UNIVERSITY
OF WARSAW

University of Warsaw
Faculty of Physics

Anna Abramuk

Properties of exotic nuclei with a high excess of neutrons in the mass region A = 110

Doctoral thesis

The thesis supervised by
dr hab. Jan Kurpeta
Nuclear Physics Division UW

Warsaw, September 2025

Abstract

The thesis presents the results of a study of the exotic, neutron-rich nuclei ^{107}Mo, ^{117}Ag, and ^{119}Ag, at the limits of contemporary experimental methods by means of trap-assisted spectroscopy. The studied nuclei were produced in proton-induced fission of a ^{238}U target. Protons were accelerated in the K-130 cyclotron at the Accelerator Laboratory of the University of Jyväskylä (Finland). The fission fragments were then stopped in a gas cell of the Ion Guide Isotope Separator Online (IGISOL) system. Next a dipole magnet separated an isobaric beam of a selected mass number A. Then the Penning-type ion trap called JYFLTRAP was used to select ions of a wanted element out of the isobaric beam, forming a so-called monoisotopic beam. β decays of the monoisotopic samples populated levels in their daughter nuclei (the nuclei of interest in this work). The γ quanta and β particles following β-decay were recorded using germanium Low-Energy Germanium detectors and a thin plastic scintillator, respectively.

The nuclei ^{107}Mo, ^{117}Ag and ^{119}Ag were studied via $\beta\gamma$ coincidence methods. As a result 28 new γ transitions for the nucleus ^{107}Mo, 17 new γ transitions for the ^{117}Ag nucleus, and 58 new γ transitions for the ^{119}Ag nucleus were discovered. The energy of the isomeric state in ^{119}Ag was determined to be 33.4 keV. The observed β half-lives range from 0.27$\pm$0.02 s for the β decay of ^{107}Nb to ^{107}Mo, to 0.87$\pm$0.02 s for the β decay of ^{119}Pd to ^{119}Ag.

A spin and parity assignment of $1/2^+$ is proposed for the ground state of ^{107}Mo, replacing the previous assignment. The first excited level at 65.4 keV has been assigned $5/2^+$. Moreover the placement of the $(1/2^-)$ level above the $(7/2^+)$ ground state in ^{117}Ag is proposed, supported by data from spontaneous fission. Two distinct nuclear-level structures were observed in ^{117}Ag, built on the $1/2^-$ and $7/2^+$ isomers. Experimental results were interpreted using a deformed shell model.

Experimental data on exotic nuclei like these are essential for calculating the correct path of the astrophysical r-process. Over the years, many astrophysical sites have been proposed for the r-process, but its actual location remains uncertain. In addition, providing new experimental data from exotic nuclei is crucial for testing existing theoretical models.

By combining γ-spectroscopy, which provides information on nuclear properties, with optical methods, which map the electron distribution and enable the determination of key nuclear parameters such as masses, isomeric energies, spins, and magnetic dipole and electric quadrupole moments, it might be possible to determine r-process site with greater accuracy. This view is supported by the fact that the energy and spin of the isomeric state in ^{119}Ag, determined independently through γ and optical spectroscopy, were found to be identical.

Contents

Chapter 1. Introduction

The physical world consists of atomic nuclei surrounded by clouds of electrons. An atomic nucleus of medium mass is approximately 10^{-4} times the size of an atom and is composed of positively charged protons and neutral neutrons. The number of protons, denoted by Z, identifies different elements. An isotope of an element is defined by a fixed proton number Z but a variable neutron number N. The mass number of the isotope, A is the sum of the protons and neutrons, given by $A = Z + N$.

At present, the periodic table of elements extends from hydrogen ($Z = 1$) to oganesson ($Z = 118$) [1], and only those elements are known to exist. However, the variation in neutron numbers for each element remains a significant subject of investigation. There are only about 283 stable or sufficiently long-lived nuclei found on Earth and in its vicinity [2]. Theoretical predictions suggest that about 6000 to 7000 distinct nuclear species can form bound systems that can be studied. Most of them contain more neutrons than protons. These nuclei are therefore called *neutron-rich nuclei*.

In Fig. 1 the nuclear chart displays known or hypothetical nuclei as a function of their neutron (N) and proton (Z) numbers. Moving horizontally across the chart corresponds to following an isotopic chain. Nuclei that share the same mass number A but have different proton and neutron numbers are known as *isobars*. The valley of stability, represented by black squares in the center of the graph, contains only stable nuclei, which do not undergo any radioactive transformation. Nuclei positioned below the stability line have an excess of neutrons compared to protons and undergo β^- decay. In contrast, nuclei above the valley of stability have a lack of neutrons and undergo β^+ decay or electron capture (EC). Magic proton and neutron numbers are indicated with black lines. A nucleus in which the number of protons Z or neutrons N equals one of the numbers 2, 8, 20, 28, 50, 82, or $N = 126$ is called a *magic-number nucleus*. If both the number of protons and neutrons in a given nucleus is a magic number then it is a double magic nucleus. Nuclei that are far from the stability line may emit clusters of protons or neutrons, such as ^{4}He or ^{12}C nuclei. Nuclei with an atomic number greater than 83 and mass numbers exceeding 209 are unstable and undergo α decay, spontaneous fission, or an emission of delayed neutrons.

The inaugural 1958 edition of the Karlsruhe Nuclide Chart included information on 1517 nuclides across 102 chemical elements known at that time [3]. In contrast, the recent edition features data for 4122 nuclides covering all 118 currently recognized chemical elements [4]. This represents only the beginning of the journey to understanding the laws and forces responsible for nuclear properties. The most interesting nuclei are poorly known or have not yet been studied. They do not exist under terrestrial conditions and are therefore called *exotic nuclei*. Theoretically predicted number of bound nuclei (for $2 < Z < 120$) is about 7000 [5].

Over the past forty years, significant progress has been made in the production and study of exotic nuclei. This progress has been enabled by modern experimental techniques, collectively known as *radioactive beams*. For instance, the number of known nuclei

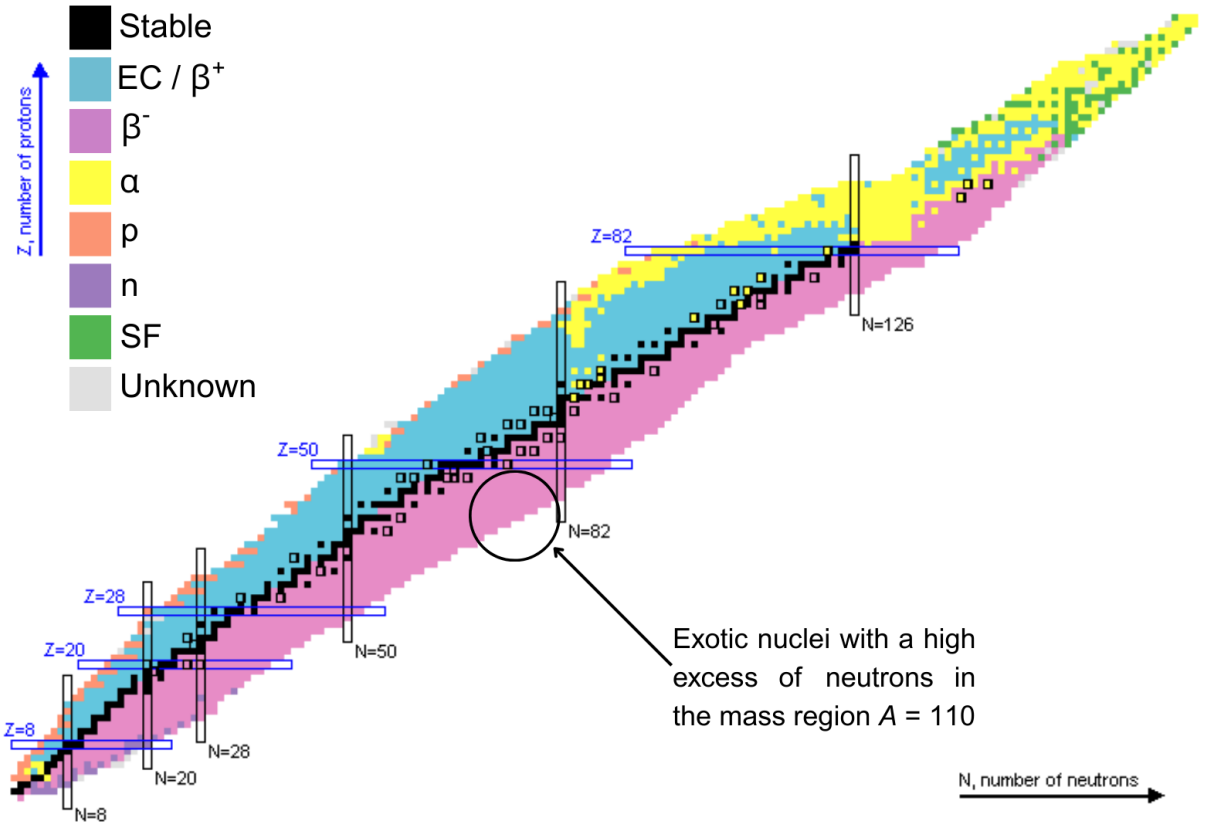

Figure 1: The nuclear chart with the area of interest in this work highlighted in a circle. The key shows the nuclear decay modes. Adapted from [1].

increased from about 2200 in 1981 to about 3000 in 2006 [6]. Although this technique was not employed in the present study, it remains an important tool for nuclear physicists.

This study investigates the nuclear structure of neutron-rich nuclei in the mass region $A = 110$, specifically focusing on ^{107}Mo, ^{117}Ag, and ^{119}Ag. These nuclei, highlighted in pink in Fig. 1, exhibit an extreme neutron-to-proton ratio (N/Z) and are located in the midshell region, far from closed neutron shells ($N = 50$ and 82) and magic proton numbers ($Z = 28$ and 50). Each nucleus is considered exotic and was produced indirectly via the β^- decay of its parent nucleus.

The studied nuclides are produced through a light-particle-induced fission reaction of ^{238}U. They undergo thermalization and charge reduction to the 1^+ charge state in a helium jet, followed by precise mass separation in a Penning trap. This technique, well-known for its high mass resolution, can separate even isomeric states [7]. The IGISOL technique, developed in Jyväskylä [8], provides a unique way to produce mass-separated, short-lived radioactive sources of elements inaccessible to other setups (see Chapter 4.3). Currently, there is a high demand for data on such nuclei, in particular on neutron-rich nuclei of refractory elements with masses $A \simeq 110$, which challenge the limits of current experimental techniques and nuclear models.

The structure of a nucleus within the nuclear shell model (see Chapter 3.3) can be understood by considering nucleons occupying discrete single-particle energy levels that form shells. A large energy gap between shells defines certain nucleon numbers as magic numbers. Magic numbers for protons and neutrons result in a more tightly bound nucleus and are firmly confirmed experimentally. As one moves away from these magic numbers,

the nucleus becomes deformed and loses its spherical shape. The basis of the technique known as *nuclear spectroscopy* is to reproduce the excited state structure in the studied, exotic nucleus. Although excited states do not directly reveal the extent of nuclear deformation, they can be used to study shape transitions and other structural effects. This is achieved by analyzing trends in the energies of excited levels, band structures, half-lives, spin-parities, and decay energies.

Moreover, the study of neutron-rich nuclei far from stability is crucial for astrophysical nucleosynthesis calculations, particularly for the rapid neutron-capture (r) process, which produces about half of the heavy elements in the universe [9]. This process occurs near the neutron dripline, where experimental data on nuclear properties are largely inaccessible with current facilities. The *neutron dripline* represents the absolute limit of the neutron-to-proton ratio allowed by nature. Studying the properties of exotic nuclei accessible with current techniques helps develop models that predict the characteristics of nuclei required for r-process simulations. An additional motivation is to provide experimental data to validate and refine nuclear models, which will be discussed in the next chapter.

This thesis is organized as follows: Chapter 2. Research Motivation describes the scientific motivations for the γ-spectroscopy conducted in this work on neutron-rich nuclei around mass $A = 110$. Chapter 3. Theoretical Background presents the theoretical background essential for understanding and describing the properties of neutron-rich nuclei. Chapter 4. Experimental Methods introduces the experimental setup used for γ-spectroscopy. Chapter 5. Spectroscopy Techniques describes the spectroscopy methods employed in this work. Chapter 6. β^- decay of $^{107}_{41}$Nb to $^{107}_{42}$Mo presents the results for the ^{107}Mo nucleus, Chapter 7. β^- decay of $^{117}_{46}$Pd to $^{117}_{47}$Ag for the ^{117}Ag nucleus, and Chapter 8. β^- decay of $^{119}_{46}$Pd to $^{119}_{47}$Ag for the ^{119}Ag nucleus. Finally, Chapter 9. Conclusions provides a summary and outlook.

The main results of this thesis are presented in the following publications:

1. First β-decay scheme of ^{107}Nb: New insight into the low-energy levels of ^{107}Mo
J. Kurpeta, A. Płochocki, W. Urban, **A. Abramuk**, L. Canete, T. Eronen, A. Fijałkowska, S. Geldhof, K. Gotowicka, A. Jokinen, A. Kankainen, I. D. Moore, D. Nesterenko, H. Penttilä, I. Pohjalainen, M. Pomorski, M. Reponen, S. Rinta-Antila, A. de Roubin, T. Rząca-Urban, M. Vilén, and J. Wiśniewski
Phys. Rev. C **100**, 034316 (2019)

2. β- and γ-spectroscopy study of ^{119}Pd and ^{119}Ag
J. Kurpeta, **A. Abramuk**, T. Rząca-Urban, W. Urban, L. Canete, T. Eronen, S. Geldhof, M. Gierlik, J.P. Greene, A. Jokinen, A. Kankainen, I.D. Moore, D.A. Nestereneko, H. Penttilä, I. Pohjalainen, M. Reponen, S. Rinta-Antila, A. de Roubin, G.S. Simpson, A.G. Smith, and M. Vilén
Phys. Rev. C **105**, 034316 (2022)

3. Excited levels in ^{117}Ag studied via β^- decay and spontaneous fission
A. Abramuk, J. Kurpeta, W. Urban, T. Eronen, A. Jokinen, A. Kankainen, I.D. Moore, H. Penttilä, M. Pomorski, S. Rinta-Antila, A.G. Smith, G. S. Simpson, and J.P. Greene
Phys. Rev. C **111**, 034301 (2025)

Chapter 2. Research Motivation

Over the past century, significant advancements have been made in nuclear physics with the development of new facilities, instruments, and experimental techniques. These advancements have not only deepened understanding of nuclear structure but have also enabled the application of nuclear physics across a wide range of fields, including nuclear medicine and imaging, study of ancient art, power industry, and cosmology [10]. Nevertheless, a broader region of potentially bound nuclei exists beyond the reach of current experimental capabilities [4, 5].

Spectroscopic investigations in the neutron-rich region of the nuclide chart are typically motivated by the diversity of nuclear structures and shapes, as well as their significant relevance to the astrophysical r-process. Further insight into this topic are provided in the following chapter.

Moreover, due to the complex nature of the nucleus, no single coherent theory of the atomic nucleus has yet been developed, that can describe all nuclear properties within a consistent formalism. Several models of atomic nuclei exist, each of which describes only a limited set of nuclear properties, and these will be described in more detail in the next chapter.

The outermost nucleons are often the most crucial for gaining insight into the observed properties of the nucleus, such as spin, parity, β feeding, and γ transition types. Collecting experimental data is therefore essential to validate and improve theoretical nuclear models.

The research questions which this work has sought to answer are as follows:

QUESTION 1: **ISOMERIC STATES**

The research question is whether isomeric states are present in the neutron-rich nuclei under study in the mass region $A = 110$ and what determines their occurrence. An isomer is an excited state of a nucleus whose decay to other states is hindered. This often leads to an extended lifetime of such a state, which makes it particularly convenient to observe, due to significant differences in the wave functions of the initial and final states.

QUESTION 2: **NUCLEAR DEFORMATIONS**

Nuclei near magic numbers N and/or Z typically exhibit a spherical shape. However, as additional nucleons are added, the situation changes significantly. The nuclear shape arises from the collective motion of many nucleons. It is well known that large nuclear deformations occur far from closed proton and/or neutron shells. What types of deformations (prolate, oblate, or triaxial) are observed in the studied nuclei, if they are located in the midshell region? How do these deformations evolve with changing neutron and/or proton numbers? Which nuclear mechanisms, such as proton-proton and proton-neutron interactions near the Fermi surface, rule the nature and magnitude of these deformations?

In the mass region $A = 110$, nuclides have been identified that can adopt different shapes depending on their excitation state. This phenomenon, known as *shape coexistence*, still requires thorough investigation. Consequently, attempts to describe their structure become even more complex.

Theoretical nuclear models provide predictions of the expected shape and deformation parameters for a given nucleus, but these models require experimental validation. Experimental data are crucial for testing theoretical frameworks, which perform well in describing the commonly observed *prolate* deformation but are less successful in describing *oblate* deformation. These models also less frequently consider *triaxial* shapes, which have been observed in the $A = 110$ region and exhibit three axes of symmetry [11].

The oblate nuclear shape is a relatively rare occurrence across the nuclear chart. Nuclear deformation is primarily prolate [12, 13]. Therefore, investigation of oblate shapes is crucial for advancing our understanding of nuclear structure.

The specific shape adopted by an exotic, neutron-rich nucleus at a given energy level also plays a significant role in determining the path of the r-process.

QUESTION 3: **NEW NUCLEAR STRUCTURE DATA**

Moreover, many past γ-spectroscopy studies of neutron-rich nuclei relied on less advanced separation methods (e.g., chemical separation) compared to those available in the 21st century. Today, the use of on-line separators allows the acquisition of larger quantities of higher-quality data. This research aims to confirm and significantly expand the results contained in the worldwide evaluated database [1], the Evaluated Nuclear Structure Data File (ENSDF), particularly through the discovery of new excited states and the determination of their spins and parities.

This is especially relevant for isotopes of refractory elements such as palladium, rhodium, ruthenium, and technetium, which cannot be produced using commonly employed ion sources where fission products are released from the target by diffusion at high temperatures, as in the ISOLDE setup (see Chapter 4.3). The IGISOL-type ion source, which operates at room temperature, does not face these limitations (also Chapter 4.3).

The findings of this work will not only extend the knowledge of neutron-rich nuclei but also contribute to a more accurate and predictive framework for describing very exotic isotopes. The research question is: What new phenomena in the structure of atomic nuclei can be observed by studying exotic nuclides with a large excess of neutrons?

QUESTION 4: **SYSTEMATICS OF NUCLEAR PROPERTIES**

What new trends, or rapid changes in these trends, can be deduced by following the systematics of nuclei in the $A = 110$ region in terms of half-lives, spins and parities of the ground state and low-lying excited states? Theoretical predictions for the excited states arising from the β^- decay of ^{119}Pd to ^{119}Ag are limited. The most recent theoretical publication on odd palladium isotopes with large neutron excess [14] concluded its predictions with the ^{117}Pd isotope. In contrast, a paper presenting calculations for the studied ^{119}Pd [15] drew a different conclusion regarding the spin of the ground state than that assigned according to the ENSDF databases. A publication on excited states resulting from the decay of β^- ^{117}Pd [16], separated using the JYFLTRAP ion trap, indicated a spin $1/2^+$ of the ground state, while a spin of $7/2^-$ was assigned to the isomeric state. This disagrees with the hypothesis of Sarriguren [15], who predicted $9/2^-$ for this state. This is

an example showing that the experimental studies are ahead of currently known nuclear models.

QUESTION 5: **OPTICAL SPECTROSCOPY**

Optical spectroscopy using lasers can provide information about the spins and parities of ground states and low-lying isomeric states in exotic nuclei. This method allows the investigation of electron orbital energy spectra, from which the shape of the atomic nucleus around which the electrons orbit can be determined. A key aspect is the comparison of results from laser spectroscopy with those from nuclear spectroscopy. These two independent methods provide information on nuclear shape, specifically on the deformation parameter. The main question is whether both methods yield consistent results regarding nuclear structure?

2.1 Nucleosynthesis

Nucleosynthesis is a stellar evolutionary process that begins with H and He atoms from the Big Bang, which combine to form more complex atoms via nuclear reactions that transform one element into another [17].

One of the major open questions in astrophysics is how elements heavier than iron are formed in the universe and how their abundances can be accurately described. Lighter nuclei are primarily created in stars through various processes, with fusion being the most common mechanism. However, fusion reactions can only produce energy up to elements around iron ($Z = 26$). For elements heavier than iron, two key processes come into play: the slow neutron-capture process (s-process) and the rapid neutron-capture process (r-process). The latter occurs in just about one second and is responsible for roughly half of the elements heavier than iron existing in the universe [9, 17]. This process is highly dependent on environmental factors such as temperature (1-5 $\cdot$ 10^9 K), neutron flux (at least 10^{20} $\frac{1}{cm^2 \cdot s}$), and the nuclear properties [18]. In the nuclide chart, theoretical predictions suggest that the r-process runs near the neutron-rich nuclei under study with mass $A = 110$, typically 10 - 20 neutrons beyond the stability path [17]. The majority of isotopes are formed as a result of contributions from both the s-process and the r-process [17].

The r-process requires a neutron-rich environment, where neutrons are rapidly captured by seed nuclei via (n, γ) reactions. These reactions occur much faster than the timescale of β decay. Neutron-rich nuclei continue to capture neutrons until the separation energy of the next neutron becomes sufficiently low for photons to induce nuclear disintegration. This stage, known as the *waiting point* lasts from from 0.1 to 30 s [19], and prevents further neutron capture, causing the nucleus to undergo β decay instead. Through a repeating cycle of neutron captures and β decays, heavier elements are synthesized until fission processes eventually dominate, bringing the r-process to an end in the thorium and uranium region.

As mentioned in Question 2, the specific shape adopted by an exotic, neutron-rich nucleus at a given energy level plays a significant role in determining the path of the r-process. Deformed nuclei can undergo β^- decay more rapidly, which accelerates the r-process toward the formation of heavier elements. Additionally, the type and degree of nuclear deformation affect the nucleus's binding energy. In particular, deformation can lead to so-called *islands of stability* in regions of otherwise highly unstable nuclei. These more stable, deformed nuclei can act as waiting points along the r-process path.

Increased nuclear deformation also tends to enhance the neutron capture rate, facilitating faster progression along the neutron-rich axis toward increasingly exotic nuclei. Therefore, further research on nuclear deformation may not only improve theoretical nuclear models but also provide deeper insight into the r-process path [20].

Neither the precise pathway of the r-process nor its astrophysical location is yet known. The estimated course is presented in Fig. 2.

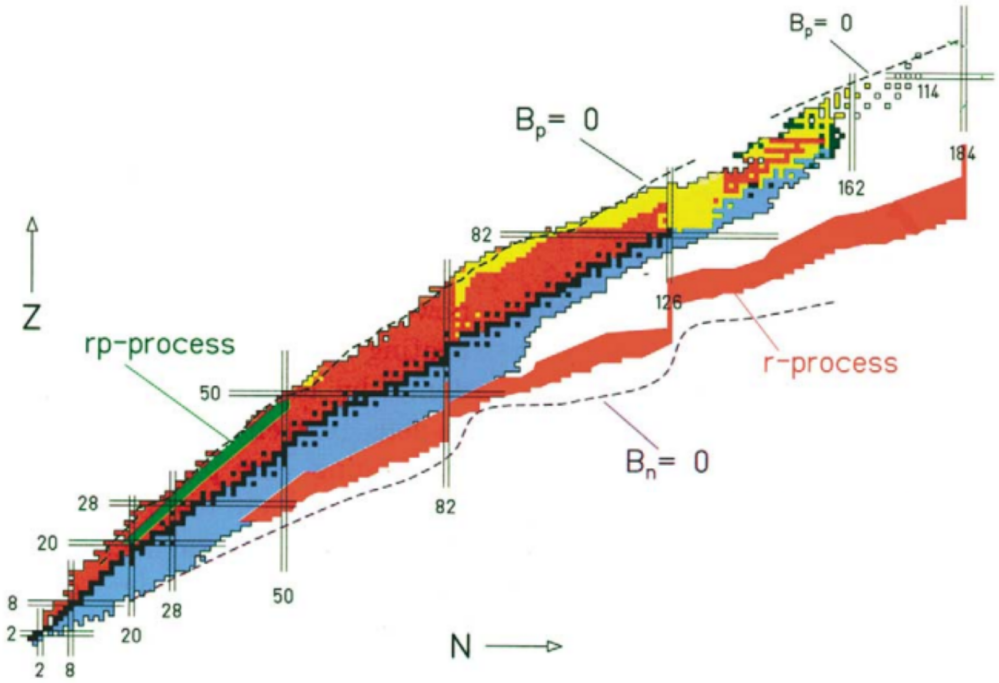

Figure 2: Map of the nuclear landscape. There are shown three paths: the r-process and the rp-process, which cross regions yet unexplored. A third path, the s-process path, runs along the stable nuclei [21].

Recent research indicates that neutron star mergers (NSMs) serve as a key environment for this process [22]. Alterations in the r-process production rate are influenced by the half-lives of both ground and excited states [23].

The r-process nuclei are not yet accessible experimentally. The study of somewhat lighter isotopes may help predict their properties, whose values are currently estimated only theoretically. Therefore, studies must rely on semi-empirical extrapolations based on observed properties, although it remains unclear whether these extrapolations are sufficiently accurate. These uncertainties limit the confidence in any conclusions drawn on this subject [17].

Theoretical extrapolations and simulations, which aim to address this challenging question, require data from approximately 5 000 tested nuclei and some 50 000 nuclear reactions [18]. This represents a substantial dataset, and the simulations face additional challenges. Yet, to improve understanding, experiments must be pushed forward toward more exotic cases.

The contributions of experimental physicists represent only one piece of the complex puzzle of understanding the r-process. Achieving a complete picture requires collaboration across multiple fields: experimental physicists collecting data, observational astronomers analyzing both ancient and young stars, gravitational-wave scientists detecting ripples in spacetime, nuclear theorists developing models of nuclear structure and neutron star

matter, and computational astrophysicists simulating phenomena such as neutron star mergers, solving intricate equations that can take months to compute even on the world's most powerful supercomputers [24].

2.2 Characteristics of the $A = 110$ mass region

The nuclei under study in this work, ^{107}Mo, ^{117}Ag, and ^{119}Ag, lie in the mass region $A = 110$, where nuclear structure exhibits a rich interplay between single-particle and collective effects. Only a limited number of theoretical predictions exist for neutron-rich nuclei in this region, making experimental studies particularly valuable.

In the vicinity of $Z = 40$, corresponding to elements such as yttrium and zirconium, ground states exhibit a sudden change in nuclear deformation [25, 26, 27]. These nuclei lie far from the nearest proton magic number, $Z = 50$, and contain more than fifty neutrons, with several occupying orbitals above the closed neutron shell . Such phenomena provide a useful framework for interpreting the structure of ^{107}Mo and the studied silver isotopes.

Laser spectroscopy studies of yttrium isotopes [25] indicate that for neutron numbers $N = 50$ - 60, nuclei exhibit oblate ground-state deformations, which can be characterized as increasingly soft. In this context, the gradual addition of neutrons to the nucleus leads to less pronounced minima on the potential energy surface. As a result, nuclear shapes become more sensitive to fluctuations (oscillations) or changes in response to small variations in energy. A sudden transition to a rigid prolate deformation is observed at $N =$ 59 - 60. In [26], the authors employed Monte Carlo Shell Model (MCSM) calculations and compare their results with experimental data for zirconium isotopes. These calculations confirmed this transition, showing prolate deformation from ^{100}Zr to ^{110}Zr and suggesting the coexistence of prolate and triaxial shapes. These results highlight general trends in deformation relevant for the interpretation of ^{107}Mo, ^{117}Ag, and ^{119}Ag.

Key observables for studying nuclear structure include the energy ratio of the first excited 4^+ to the first 2^+ states and the reduced electric quadrupole transition probability, $B(E2)$, which can be determined both experimentally and theoretically [27]. Calculations for nuclei with $Z = 38$ - 46 and $N = 52$ - 66 reveal a sudden change in these parameters at $N = 60$ and $Z = 40$, consistent with the trends observed in Y and Zr isotopes.

Silver nuclei occupy a transitional region between the classical shell model and collective behavior, resulting in the coexistence of different structural properties at low excitation energies. A key factor is the competition between the $\pi g_{9/2}^{-3}$ configuration and core excitations. As noted in [28], the $\pi g_{9/2}$ orbital, being the only positive-parity orbit below $Z = 50$, contributes to the sub-shell closure at $Z = 40$ and plays a crucial role in the wave functions of Ag nuclei. In ^{97}Ag, the lowest positive-parity state is $9/2^+$, associated with $\pi g_{9/2}$ occupation, while the next state, $7/2^+$, could stem from excitations across the $Z = 50$ shell gap. However, its experimentally observed low energy challenges this interpretation. In medium-mass silver nuclei ($A \approx 110$), the $7/2^+$ state becomes the ground state, an effect known as the $j - 1$ anomaly. The experimentally observed low energy of this state challenges its simple interpretation as a proton excitation across the $Z = 50$ shell gap, highlighting the coexistence of single-particle and collective degrees of freedom.

Overall, these studies indicate that nuclei in the mass region $A = 110$, including ^{107}Mo, ^{117}Ag, and ^{119}Ag, display complex structural behavior. The combination of theoretical predictions and experimental observations provides a coherent framework to interpret the changes in nuclear shapes.

Chapter 3. Theoretical Background

3.1 Nuclear binding and separation energies

The atomic nucleus has a mass that is slightly lower than the combined mass of its individual nucleons due to the nuclear binding energy B, which can be calculated as:

$$B(Z, A) = [ZM_H + NM_n - M]\, c^2 \tag{3.1}$$

where M is the mass of the atom, while M_H and M_n represent the masses of the hydrogen atom and the neutron, respectively. When plotting the average binding energy per nucleon (B/A) for stable nuclei as a function of their mass number A, the value of B/A remains relatively constant, except for very light nuclei [29]. The maximum of B/A occurs for ^{56}Fe and ^{62}Ni, where $B/A \approx 8.8$ MeV [30]. In Fig. 3 the vertical axis covers values around 7.0 - 9.0 MeV, which can give the impression of larger variations in B/A for individual mass numbers A. At the top of the figure the magic numbers for neutrons and protons were highlighted, as well as the mass region $A < 30$. The binding energy values calculated using the Weizsäcker formula (solid line in Fig. 3) are in good agreement with experimental data, deviating by approximately 2% [31]. This formula will be discuss in greater detail in the next chapter. The resulting elemental abundance distribution exhibits maxima at H, He, Fe, and Pb. These jumps in B/A values correspond to closed nucleon shells, analogous to the ionisation energy for closed electron shells. Light nuclei display significant deviations and require individual analysis.

The decrease in B/A for nuclei heavier than ^{56}Fe and ^{62}Ni is attributed to the saturation of nuclear forces. The nuclear core prevents nucleons from approaching closely, and for nuclei with $A > 60$, the Coulomb repulsion between protons becomes increasingly significant. In contrast, for light nuclei, the B/A value is lower due to the surface effect, where outer nucleons are not fully surrounded, unlike nucleons near the core.

The energy required to remove a nucleon from a nucleus is referred to as the *proton separation energy* (S_p) for a proton or the *neutron separation energy* (S_n) for a neutron. The energy needed to remove a single neutron from a nucleus equals the binding energy of the original nucleus with atomic number Z and mass number A, minus the binding energy of the nucleus with the same number of protons Z, but one fewer neutron, i.e., mass number $A - 1$. Discontinuities in S_p and S_n appear at closed nucleon shells.

The separation energies, S_p and S_n, define the energy thresholds above which particle emission becomes more likely than γ ray emission. If the excitation energy of the nucleus exceeds the separation energy, de-excitation process can occur through neutron or proton emission, which competes with γ transitions and modifies the structure of the observed spectrum. This is particularly important from the perspective of γ-spectroscopy, where primarily γ-ray lines are studied, and the emitted particles are not detected by the experimental setup. Knowledge of the separation energies allows the identification of allowed

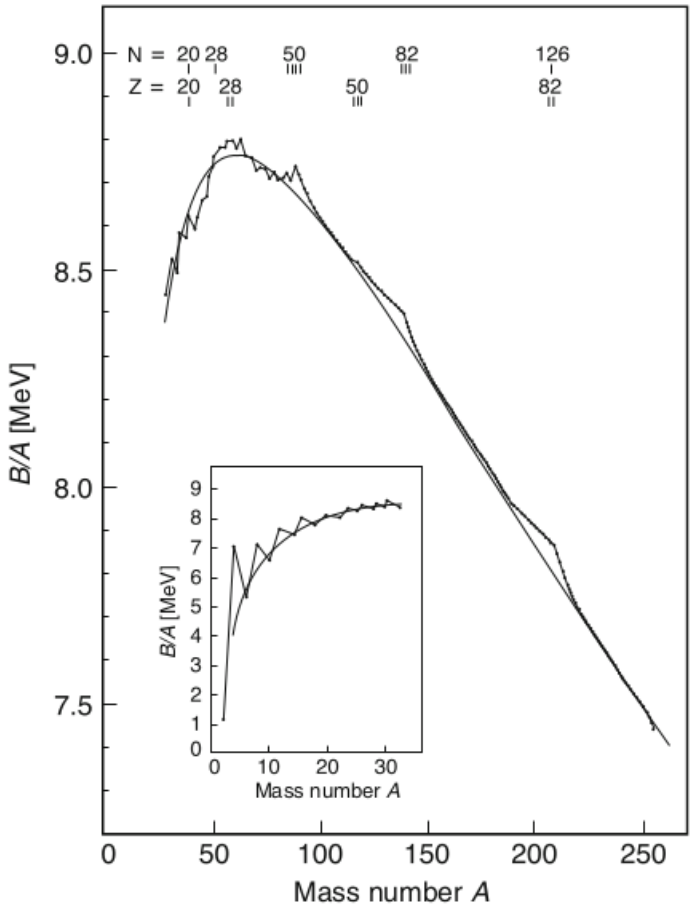

Figure 3: The average binding energy per nucleon for even-mass number A was marked with calculated dots. The solid line represents the Weizsäcker formula [32].

decay channels and facilitates the correct interpretation of the observed lines in the γ spectrum, especially for highly excited states.

3.2 The liquid drop model

The liquid drop model (LDM) assumes that the atomic nucleus behaves similarly to a liquid drop, although the *nuclear liquid* possesses an extremely high density compared to ordinary matter. The total nuclear binding energy can be expressed using the semi-empirical mass formula (Weizsäcker formula) [33] as:

$$B(Z,A) = a_{\text{vol}}A - a_{\text{surf}}A^{2/3} - a_{\text{coul}}\frac{Z^2}{A^{1/3}} - a_{\text{sym}}\frac{(A-2Z)^2}{A} + \delta, \tag{3.2}$$

where

$$\delta = \begin{cases} +12A^{-1/2}, & Z \text{ and } N \text{ even}, \\ 0, & \text{odd } A, \\ -12A^{-1/2}, & Z \text{ and } N \text{ odd}. \end{cases}$$

The first two terms describe a spherical liquid drop, contributing to the total nuclear binding energy B through the volume term (a_{vol}) and the surface term (a_{surf}). The total binding energy is further corrected for the electrostatic repulsion between protons via the

Coulomb term (a_{coul}). The last two terms primarily account for individual nucleon effects: the asymmetry term (a_{sym}) represents the difference between the number of protons and neutrons, while the pairing term (δ) reflects the tendency of nucleons to form pairs. The formula also considers that the nucleons at the nuclear surface are less tightly bound than those in the interior of the nucleus.

The liquid drop model (LDM) is useful for describing spontaneous nuclear fission. However, it does not account for the phenomenon of closed shells. This limitation arises from the classical nature of the model, which treats the nucleus as a macroscopic object and neglects quantum effects.

3.3 Nuclear shell model

In principle, every nucleus can be described using either the liquid-drop model or the Fermi gas model. However, certain phenomena, such as the γ-ray emission discussed below, cannot be adequately explained within these frameworks. When the emitted quanta originate from transitions between excited states, this indicates the presence of discrete (linear) spectra, showing that the states occupied by protons and neutrons are not continuous but discrete. To account for the existence of magic numbers, a shell-like structure is employed. They are distinguished by properties among neighbouring nuclei. Magic nuclei are distinguished from their neighbors by specific properties, including a high energy of the first excited state and elevated values of S_n and S_p.

The shell structure can be described using the potential energy $V(r)$, given in Equation 3.3, which represents the averaged potential generated by all nucleons. This potential is commonly modeled by a Woods-Saxon (W.S.) form, expressed as:

$$V(r) = \frac{-V_0}{1 + \exp\left(\frac{r-R}{a}\right)}, \tag{3.3}$$

where R is the average nuclear radius ($R = 1.25 \cdot A^{1/3}$ fm), a represents the skin thickness (typically below 1 fm), and V_0 is the depth of the potential well.

The shell model is well-suited for assigning spins and parity to excited states, as well as for studying the magnetic and electric dipole moment of nuclei. In addition, it provides information on the properties of the ground state and the lowest excited states for nuclei with both even and odd numbers of nucleons, both spherical and deformed nuclei.

In Figs. 4(a) and 4(b), the orbitals are labeled by the quantum numbers n and l, where n denotes the number of a specific orbital with an angular momentum quantum number l. Spectroscopic notation (s, p, d, f, g, h, i, ...) is used to represent different values of l ($l = 0, 1, 2, 3, 4, 5, 6, \ldots$). The maximum number of protons or neutrons that an orbital with quantum number l can accommodate (its degeneracy) is given by $2(2l + 1)$. Both the infinite well and the Woods-Saxon (W.S.) potentials fail to accurately reproduce the magic numbers for $N, Z > 20$, as shown in Fig. 4.

In 1949, [34] successfully reproduced the magic numbers (14, 28, 50, 82, 126) by incorporating a spin-orbit (SO) potential. This caused the l-orbitals to split, as illustrated in Fig. 4(c). The spin-orbit potential is expressed as $-V_{so}(r)\,\mathbf{l} \cdot \mathbf{s}$, where s is the spin angular momentum. Consequently, the energy levels in Fig. 4(c) can be labelled by the quantum numbers n, l, and j, where the total angular momentum j is defined as:

$$j = l + s \tag{3.4}$$

Here, the spin quantum number of a nucleon is $s = \pm 1/2$, and the possible values of the total angular momentum quantum number are $j = l + 1/2$ and $j = l - 1/2$ (with only $j = 1/2$ allowed if $l = 0$). The spin-orbit term can be calculated from Equation 3.5 as:

$$\langle \mathbf{l} \cdot \mathbf{s} \rangle = \frac{1}{2} \left[j(j+1) - l(l+1) - s(s+1) \right] \hbar^2 \tag{3.5}$$

The specific values for $\langle \mathbf{l} \cdot \mathbf{s} \rangle$ are given by:

$$\langle \mathbf{l} \cdot \mathbf{s} \rangle = \begin{cases} \frac{1}{2} l \hbar^2 & \text{if } j = l + \frac{1}{2}, \\ -\frac{1}{2}(l+1)\hbar^2 & \text{if } j = l - \frac{1}{2}. \end{cases} \tag{3.6}$$

The degeneracy of a given j-orbital is $2j+1$, which corresponds to the possible magnetic substates m_j, where $m_j = j, j-1, \ldots, -j$, as shown in Fig. 4(c).

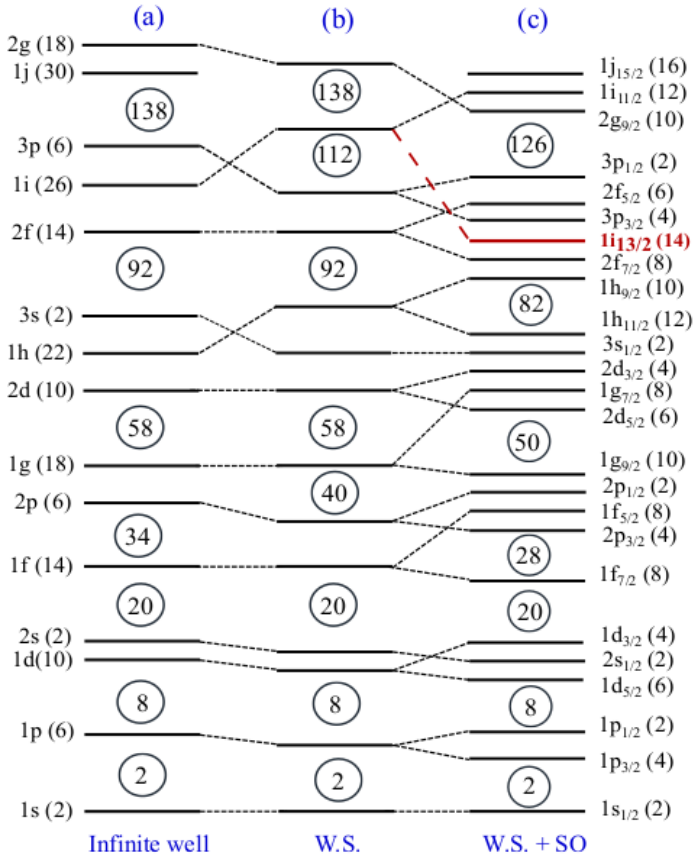

Figure 4: A schematic drawing of the energy levels of the single-particle orbitals using different nuclear potentials based on [29] (a) Infinite well, (b) Woods-Saxon potential (W.S.) and (c) Woods-Saxon potential coupled with the spin orbit (SO) interaction. The red line shows an example of the unique parity intruder orbital $1i_{13/2}$ [35].

Neutrons and protons exhibit a strong tendency to completely fill their respective shells. Consequently, the ground state spin and parity I^{Π} of nuclei with even numbers of protons (Z) and neutrons (N) is 0^+. These states are spherically symmetric, indicating that magic nuclei typically have spherical shapes. In contrast, for odd-A nuclei, the ground state spin is determined by the last unpaired nucleon.

Parity π is a quantum number that describes the symmetry properties of the wave function. Parity is given by $\pi = (-1)^l$. Therefore, orbitals with odd l will have negative parity ($\pi = -$), while those with even l will exhibit positive parity ($\pi = +$).

In Equation 3.6, the effect of the spin-orbit interaction becomes evident. The splitting of a particular l-orbital causes the higher-j state ($j = l + \frac{1}{2}$) to shift downward in energy, approaching lower orbitals with opposite parity. Conversely, the lower-j state known as an *extruder* ($j = l - \frac{1}{2}$) is pushed upward, increasing in energy. These high-j orbitals, with $j = l + \frac{1}{2}$, are referred to as *intruder states* within the shell-model framework. In Fig. 5, the single-particle shell model levels of interest for this work are presented.

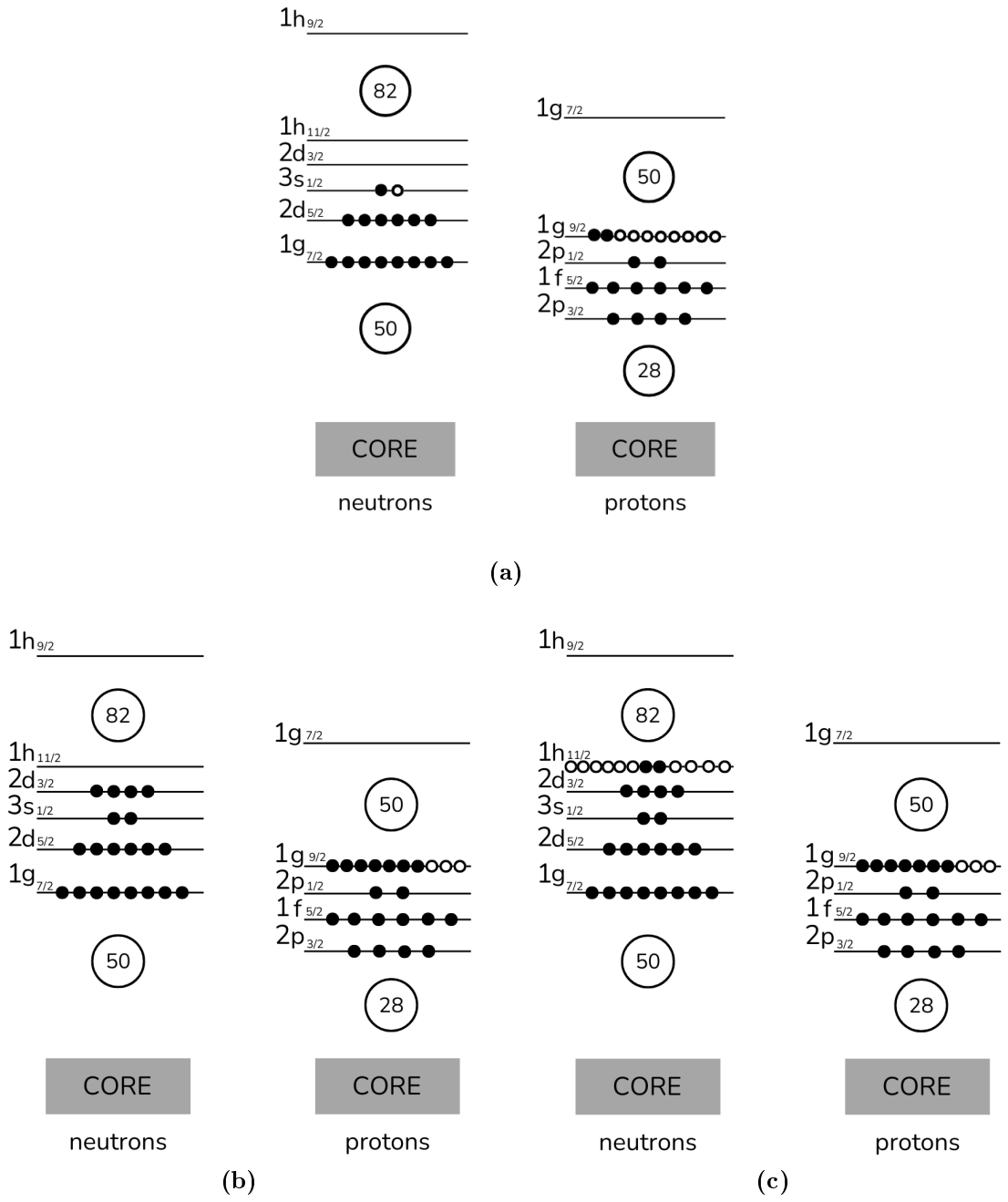

Figure 5: A schematic view of the spherical shell model energy levels relevant for this work. The occupation of levels (black circles) represents (a) ^{107}Mo, (b) ^{117}Ag, (c) ^{119}Ag.

Fig. 4(c) illustrates the combined effects of the Woods-Saxon potential and spin-orbit coupling. The highlighted line shows how the $1i_{13/2}$ orbital, which has positive parity (even l), shifts downward in energy, becoming a shell-model intruder state among neighbouring orbitals with negative parity (odd-l orbitals). The presence of such a state, surrounded by orbitals with different parities and angular momenta, often results in hindered nuclear transitions between these states.

The nuclear shell model is particularly well-suited for describing nuclei with magic numbers of protons or neutrons, where shells are closed and nuclear stability is high. It is especially effective for magic and near-magic nuclei.

3.4 Deformed shell model

In the collective model developed by Bohr and Mottelson [12], first introduced in 1952, nuclear properties are described using the collective variables β_2 and γ. The parameter β_2 quantifies the degree of deviation from a spherical shape, while γ measures the deviation from axial symmetry. Specifically, $\gamma = 0°$ and $\gamma = 60°$ correspond to axially symmetric ellipsoidal shapes, prolate and oblate, respectively. Intermediate values, $0° < \gamma < 60°$, represent triaxial shapes with three distinct semi-axes, with maximum triaxiality occurring at $\gamma = 30°$.

Some experimental observations across the nuclear chart could not be fully explained by the spherical shell model. More importantly, no theory has yet been able to simultaneously account for all nuclear properties and effects, due to the complexity of the nucleon-nucleon interaction and the many-body problem. A key breakthrough toward this goal was the realization that nuclei can adopt deformed shapes, which helped explain various experimental phenomena, such as large quadrupole moments [36]. This led to the development of the *deformed shell model*, first introduced by Nilsson in 1955 [37, 38], which modified the spherical shell model. In deformed nuclei, the total angular momentum j, used in the spherical shell model, no longer remains a good quantum number. The $2j+1$ degeneracy, present in the spherical case, is broken in the Nilsson model, and a new set of quantum numbers is introduced. The quantum number Ω replaces j, exhibiting only double degeneracy (two nucleons with $\pm\ \Omega$), where Ω represents the projection of the total angular momentum j onto the symmetry axis.

Nilsson diagrams illustrate how the energy levels of individual nucleons in a nucleus change in a function of the deformation parameter β_2. They incorporate the effects of non-spherical, typically quadrupole, deformation into the shell model. These diagrams are particularly useful for analyzing ground and excited states of nuclei that deviate from a spherical shape.

The Nilsson diagrams for protons and neutrons relevant for this work are presented in Fig. 6.

The deformation considered in the Nilsson model is described by the quadrupole deformation parameter β_2. A negative value of β_2 ($\beta_2 < 0$) corresponds to oblate deformation, while a positive value ($\beta_2 > 0$) describes prolate deformation, see Fig. 7. The deformation parameter β_2 can be expressed as follows [39]:

$$\beta_2 = \frac{4}{3}\sqrt{\frac{\pi}{5}}\frac{\Delta R}{R_{\text{ave}}} \tag{3.7}$$

The average radius R_{ave} is defined as $R_{\text{ave}} \approx \frac{1}{3}(a+2b)$ [12], where a and b represent the two axes of the ellipsoid shown in Fig. 7. The difference between these axes is given by

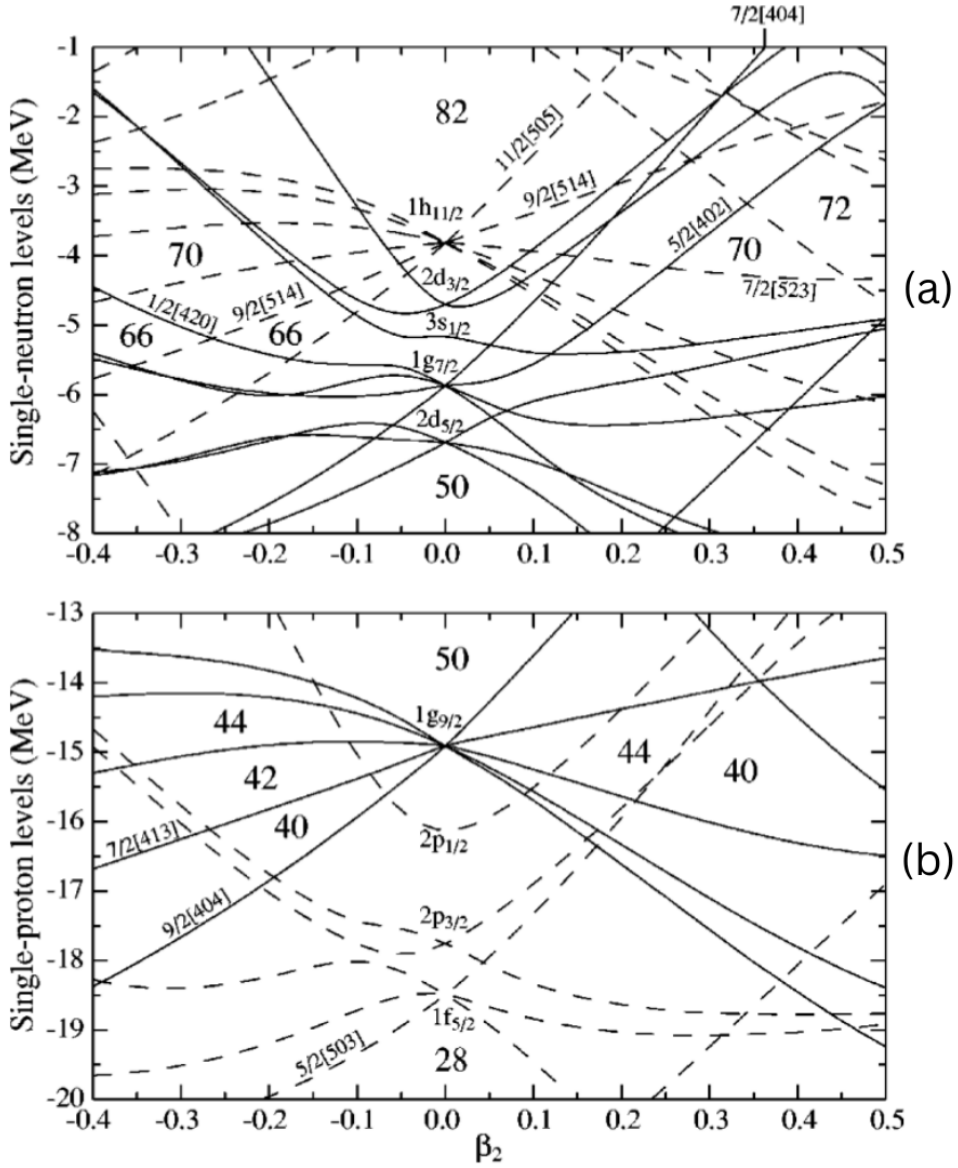

Figure 6: (a) The calculated single-neutron and (b) single-proton levels of the Woods-Saxon potential. Axial symmetry is assumed with $\beta_4 = -|\beta_2|/6$, approximating the hexadecapole value of the ground states obtained from the TRS calculations. Positive and negative parity are indicated by solid and dashed lines, respectively [40].

$\Delta R = a - b$. The ellipsoid in Fig. 7 illustrates a prolate deformation, with the deformation parameter set to approximately $\beta_2 \sim 0.2$. In turn, Fig. 8 presents several basic nuclear shapes within the deformed shell model.

The shape of a nucleus is highly sensitive to structural factors and can vary between neighbouring nuclei as the proton number Z or neutron number N changes [41]. Moreover, the nuclear shape can undergo transitions at low excitation energies within a very narrow energy range, resulting in the coexistence of two or more states with different shapes within the same nucleus. This phenomenon is known as *shape coexistence* [42].

Shape coexistence can be understood within the framework of the Nilsson model. When the sum of the orbital energies of single nucleons, plotted as a function of deformation, exhibits two distinct minima, shape coexistence may occur. This phenomenon appears across a wide range of nuclei and represents one of the major challenges for nu-

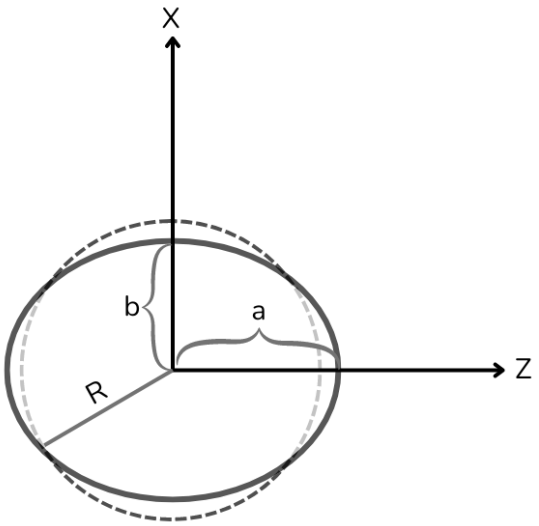

Figure 7: The solid line represents an ellipsoid associated with a prolate deformation of $\beta_2 \sim 0.2$. The ellipsoid is compared with a circle ($\beta_2 = 0$) drawn with a dashed line, having a radius R and the same volume as the ellipsoid.

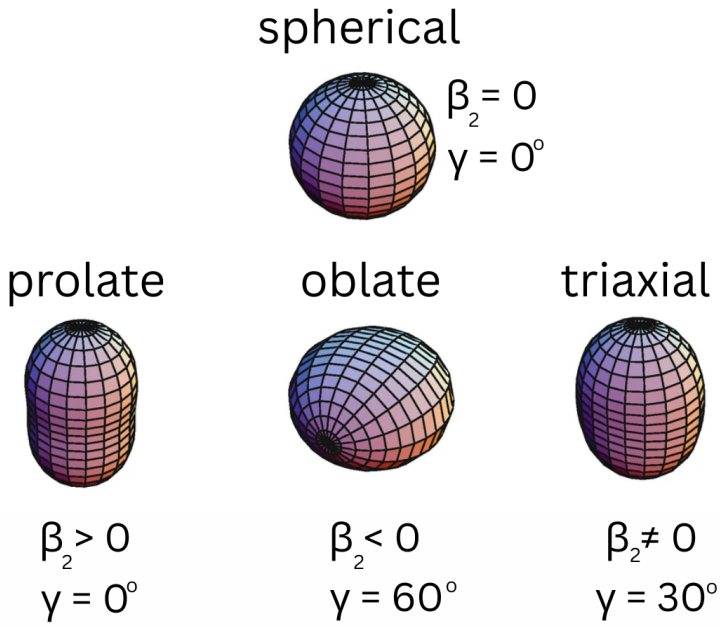

Figure 8: Examples of basic nuclear shapes in deformed shell model: spherical, prolate, oblate, and triaxial shapes. The deformation parameters β_2 and γ describe the deviation from sphericity and axial symmetry, respectively. Adapted from [43]

clear structure theories. Over the years, the perception of shape coexistence has shifted: from being seen as an exotic rarity, to a phenomenon observed in specific *islands of occurrence*, and is now considered to be a general phenomenon present in nearly all nuclei except the lightest ones. Shape coexistence can be identified through several key features: the presence of a rotational band structure built on intruder states originating from above the $Z = 50$ shell closure, enhanced $E2$ transitions within this intruder band, hindered electromagnetic transitions between intruder and spherical configurations, and the strong population of intruder states in stripping reactions contrasted with their weak or absent

population in pickup reactions [42].

According to Casten [13], triaxial deformation refers to a nuclear shape in which the nucleus lacks any axis of symmetry, meaning that all three principal axes have different lengths. This results in a more complex rotational behavior compared to axially symmetric (prolate or oblate) nuclei. Additionally, the rigid triaxial rotor model developed by Davydov and Filippov [44] provides a straightforward framework for describing nuclei with shapes that lack axial symmetry. The γ degree of freedom is essential for capturing the characteristics of triaxiality and plays a key role in describing such nuclei. For values of γ between 0° and 60°, the nucleus adopts triaxial shapes with three distinct semi-axes, with maximum triaxiality occurring at $\gamma = 30^\circ$. Additionally, triaxial nuclear shapes manifest through various phenomena, such as chirality and wobbling, and indirectly through signature splitting [45] and signature inversion. The study of triaxiality is fundamental for understanding the evolution of nuclear shapes and the associated collective excitations.

3.5 Nuclear excited states

Excited states in an atomic nucleus arise when one or more valence nucleons are promoted to higher unoccupied shells. In nuclei with closed shells, excitations are predominantly non-collective. When the number of valence nucleons is small, the excitation spectrum consists mainly of non-collective states (Fig. 9(a)). In a spherically symmetric nucleus, the only collective motion corresponds to surface oscillations, i.e., small deviations from the spherical shape.

As nucleons are added to the outer shell, the nucleus remains largely spherical but becomes increasingly likely to undergo deformation, as reflected in its excitation spectrum (Fig. 9(b)). With a further increase in a number of valence nucleons, the nucleus may become unstable in the spherically symmetric configuration, adopting a deformed equilibrium shape. Such deformed nuclei can undergo rotational motion (Fig. 9(c)).

3.6 Single-particle excitations

In nuclei with few valence nucleons, excited states can be classified into two types: single-particle excitations and multi-particle excitations. The first type involves a single nucleon being promoted to a higher orbital while the remaining nucleons form an inert core. The second type involves several nucleons being promoted simultaneously, often requiring enough energy to break nucleon pairs.

According to the shell model, even-even nuclei have a 0^+ ground state, as all nucleons are paired. Excited states arise when nucleons acquire sufficient energy to break from their paired configuration and occupy higher orbitals. The coupling of unpaired nucleons determines the spin and parity of the excited states, which can range from $|j_1 - j_2|$ to $j_1 + j_2$, where j_1 and j_2 denote the angular momenta of the orbitals involved.

Although the energy associated with residual interactions is small compared to the average nuclear potential, these interactions play a crucial role in determining the coupling scheme of valence nucleons and influence important nuclear properties such as spin, magnetic moment, and quadrupole moment. In even-even nuclei, the first excited state typically has spin and parity 2^+.

As the number of valence nucleons increases, the tendency for the nucleus to deform also grows. The spherically symmetric state becomes unstable, and the nucleus adopts a deformed equilibrium shape. In such nuclei, rotational motion can occur, representing

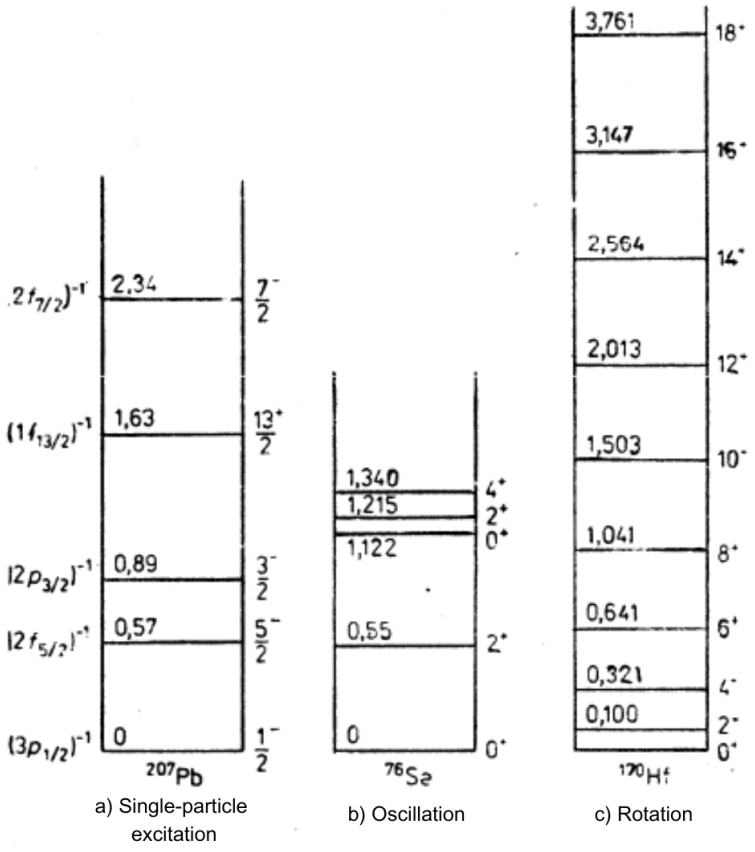

Figure 9: Single-particle versus collective excited states in nuclei: comparison of excitation spectra [46].

one type of collective excitation possible in deformed systems (Fig. 9(c)).

The behavior of valence nucleons is largely determined by residual interactions. In nuclei with only a few nucleons in the outer shell, it is possible to reproduce the couplings and energies of states that arise due to pairing forces. These pairing interactions are a short-range component of the residual nuclear forces and tend to maintain a roughly spherical shape, opposing deformation in nuclei with few valence nucleons.

The gradual addition of valence nucleons illustrates the transition from non-collective to collective excitations. As the nucleus becomes increasingly likely to undergo deformation, collective modes such as surface vibrations and rotational motion emerge, marking the onset of collective behavior. This evolution is clearly visible in the excitation spectra, where non-collective single-particle states gradually give way to vibrational and rotational bands (Fig. 9(b) - 9(c)).

3.7 Collective excitations

Collective excitations are associated with the correlated motion of many nucleons within the nucleus. These correlations are driven by the long-range component of the nuclear force, whose influence grows with the number of valence nucleons. While the shell model alone cannot fully account for the structure of medium- and heavy-mass nuclei, collective effects manifest as rotational and vibrational bands and are confirmed experimentally by enhanced electromagnetic transition probabilities, particularly large $B(E2)$ values [46].

In the macroscopic collective model, nuclear deformation emerges naturally as a manifestation of quadrupole correlations. In contrast, in the microscopic deformed shell model (Nilsson model), deformation is introduced explicitly, modifying the single-particle structure. Both approaches are complementary in describing collective excitations.

Two fundamental types of collective excitations are distinguished. Vibrational excitations correspond to oscillations of the nuclear surface and may occur in both spherical and deformed nuclei. Quadrupole vibrations are the most prominent and give rise to vibrational bands characterized by sequences of 0^+, 2^+, 4^+, and higher-spin states. Rotational excitations correspond to the collective rotation of a nucleus with a stable, deformed equilibrium shape and lead to rotational bands with characteristic energy spacings.

Vibrational excitations in deformed nuclei involve oscillations around the equilibrium shape. The simplest of these are β vibrations, associated with changes in the elongation of the nucleus, and γ vibrations, Higher-order vibrational modes, such as octupole vibrations, may occur in certain nuclei, leading to reflection-asymmetric (pear-shaped) deformations. Each vibrational mode produces a vibrational band, which is observable in γ-spectroscopy as a regular sequence of transitions.

In even-even nuclei, the addition of a single quadrupole phonon to the 0^+ ground state produces the first excited 2^+ state. Adding a second quadrupole phonon generates a triplet of states with spins 0^+, 2^+, and 4^+, approximately twice the energy of the first excited state. The addition of a third phonon yields a quintuplet with spins 0^+, 2^+, 4^+, and 6^+. The addition of an octupole phonon produces a 3^- state. An example of such vibrational structures is shown in Fig. 9(c).

Rotational excitations occur in nuclei with permanent deformation, quantified by the parameter β_2 [39]. For $\beta_2 > 0$, the nucleus is prolate, whereas for $\beta_2 < 0$, it is oblate. The presence of a stable oblate deformation is a rare phenomenon. Rotational bands in even–even nuclei have even spins and positive parity. The rigid-rotor model describes the energy of a state with spin I as

$$E_I = \frac{\hbar^2}{2\mathcal{J}} I(I+1), \quad I = 0, 2, 4, \ldots \tag{3.8}$$

$\mathcal{J}$ is the moment of inertia of the deformed nucleus.

Three types of collective bands can be distinguished. The first type is a rotational band built on a deformed ground state, with successive excited states having spins 2^+, 4^+, and higher, with increasing energy spacing. The second type corresponds to γ vibrations, in which the nuclear surface oscillates perpendicular to the symmetry axis, producing excited states with spins 2^+, 3^+, and higher. The third type is associated with β vibrations, in which the nuclear surface oscillates along the symmetry axis, giving rise to successive states with spins 2^+, 4^+, and higher. An example of this classification is shown in Fig. 10.

The ratio $E(4_1^+)/E(2_1^+)$ provides a useful measure of nuclear structure. Spherical nuclei typically exhibit $E(4_1^+)/E(2_1^+) \simeq 2$, indicating vibrational behavior. Strongly deformed nuclei show $E(4_1^+)/E(2_1^+) \simeq 3.33$, consistent with an axially symmetric rotor, while transitional nuclei fall between these limits, typically with $E(4_1^+)/E(2_1^+) \simeq 2.7$. Experimental values of E_4^+/E_2^+ for isotopes of Zr, Mo, Ru, Pd, and Cd are shown in Fig. 11, illustrating the evolution of collective behavior with neutron number $N > 60$.

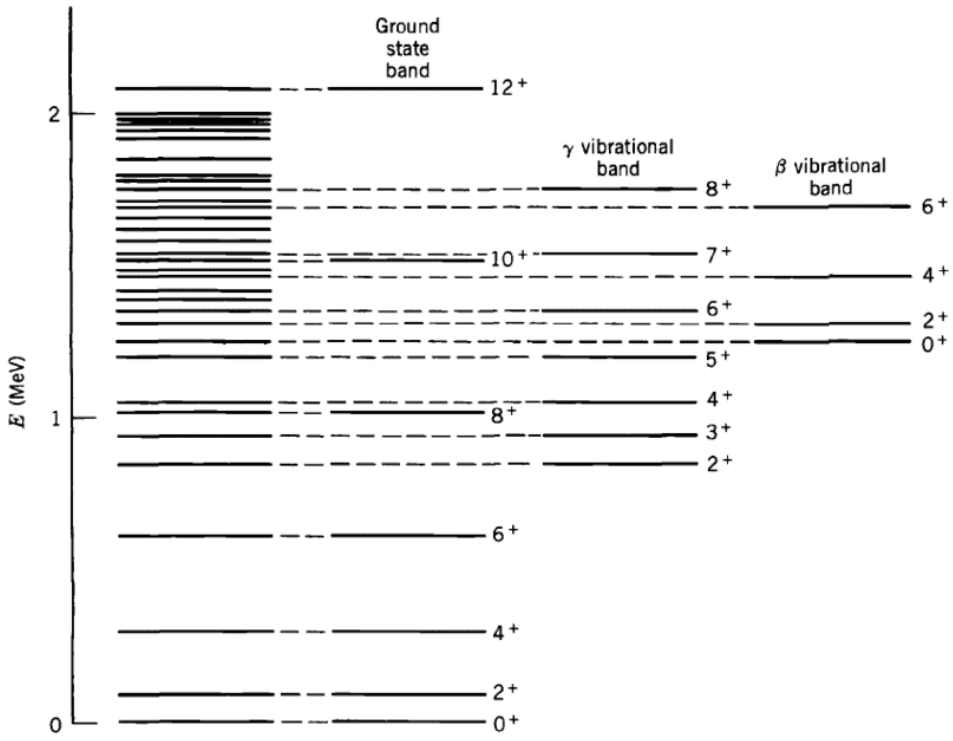

Figure 10: Classification of rotational bands in even–even nuclei [39].

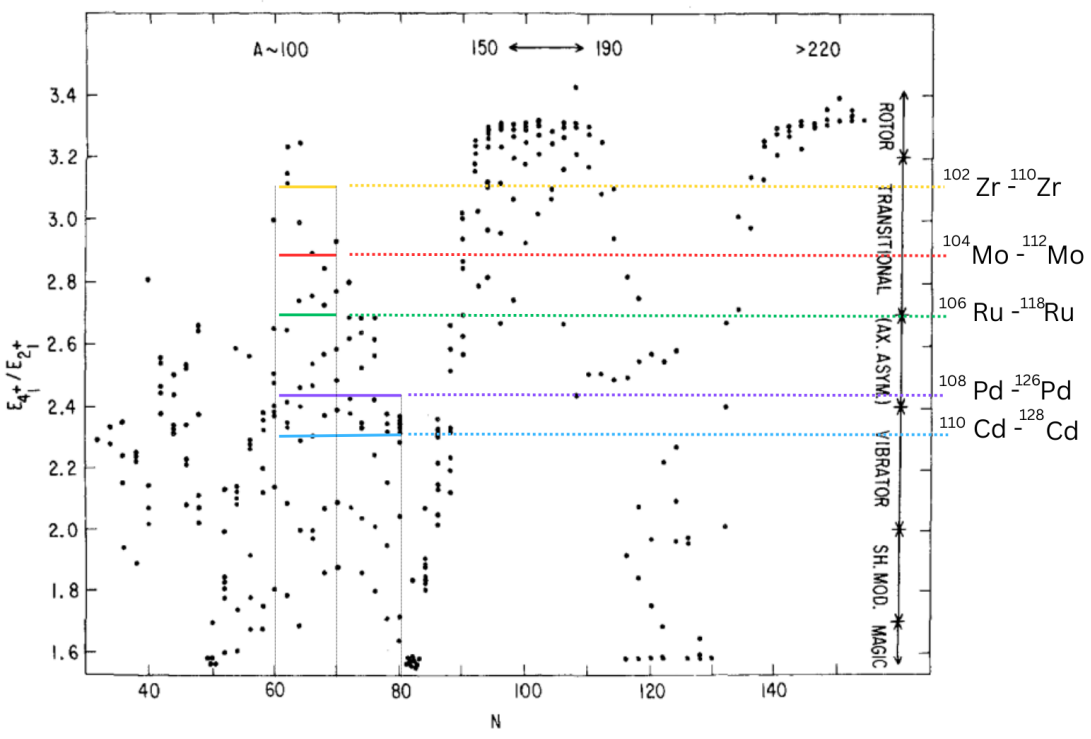

Figure 11: E_4^+/E_2^+ values plotted against N for the nuclei with $N > 30$ and even mass. Adapted from [13]. The experimental data were taken from [1] for the following isotopes: ^{102}Zr – ^{110}Zr (yellow line), ^{104}Mo – ^{112}Mo (red line), ^{106}Ru – ^{118}Ru (green line), ^{108}Pd – ^{126}Pd (purple line), and ^{110}Cd – ^{128}Cd (blue line).

3.8 Collective behavior in transitional nuclei

The nuclei ^{107}Mo, ^{117}Ag, and ^{119}Ag exhibit a rich spectrum of excited states resulting from both non-collective and collective excitations. In these nuclei, valence nucleons outside closed shells can be promoted to higher orbitals, giving rise to single-particle and multi-particle excitations. In ^{107}Mo, the relatively small number of valence nucleons allows for a significant contribution of single-particle excitations, where an unpaired nucleon is promoted to a higher orbital while the remaining nucleons form an inert core. Multi-particle excitations, involving the simultaneous promotion of several nucleons and often requiring sufficient energy to break nucleon pairs, also contribute to the excitation spectrum.

With increasing numbers of valence nucleons collective excitations become increasingly important. These excitations are associated with the correlated motion of many nucleons and are driven by the long-range component of the nuclear force. Vibrational excitations correspond to oscillatory deformations of the nuclear surface. The most prominent quadrupole vibrations generate vibrational bands characterized by sequences of 0^+, 2^+, 4^+, and higher-spin states. In addition, β vibrations, corresponding to changes in stretching, and γ vibrations, associated with triaxial oscillations, are observed. In certain cases, octupole vibrations produce reflection-asymmetric states such as 3^- levels.

Rotational excitations are observed in nuclei when a stable deformation is present. In the case of ^{107}Mo, a moderate prolate deformation leads to rotational bands with energies following the rigid-rotor formula. In the heavier silver isotopes, ^{117}Ag and ^{119}Ag, deformation is more pronounced, resulting in rotational bands with even-spin positive-parity states. Experimental studies of these isotopes reveal sequences of excited states that can be interpreted as vibrational multiplets and rotational bands, illustrating the gradual transition from single-particle-dominated excitations in ^{107}Mo to strongly collective behavior in the heavier silver isotopes.

3.9 Nuclear isomers

Nuclear isomers are excited, metastable states of nuclei, which live for longer than a nanosecond or exhibit measurable half-lives [47]. A specific term has also been introduced for astrophysical isomers, referred to as *astromers* [47]. They are nuclear isomers that play a significant role in the astrophysical environment of interest.

The discovery of nuclear isomerism is usually credited to the work of Otto Hahn [48], who, in 1921 conducted research that led to the identification of a new radioactive decay product of uranium.

Most nuclear isomers can be interpreted within the shell model as configurations involving one or two, and in some cases up to ten, specific unpaired nucleon orbitals. These orbitals often couple to produce higher-spin states compared with other states of similar excitation energy, which makes their decay dependent on the emission of high-spin and/or low-energy radiation, which in turn leads to unusually long half-lives [49].

It is now widely recognized that various nuclear structure effects can result in isomeric states. The most well-known examples include spin traps, in which the excited state has a significantly different spin compared to lower-energy states. K isomers, in which the spin orientation relative to the symmetry axis in a deformed nucleus differs greatly from lower-energy states. And shape isomers, in which the excited state has a shape that is notably different from lower-energy states [50].

The occurrence and characteristics of isomers form a fundamental basis for the construction of nuclear models, including collective models [49].

The complexity arises, in some cases, from the coexistence of states associated with different nuclear shapes [51], whereas in other cases it is due to very low-lying levels, which are best characterized as many-quasi-particle states [52].

In deformed nuclei with a symmetry axis, the angular momentum vector tends to retain an approximately conserved projection, K, onto that axis, giving rise to the existence of K isomers. Due to their direct relation to shell-model orbitals, such isomers are often regarded as simple nuclear states with a largely well-defined wave function. The blocking of pairing correlations in multiparticle configurations further simplifies these states, sometimes making them sometimes easier to describe than the ground state [49].

In many cases, isomeric radiation does not strictly follow selection rules, as its properties are highly sensitive to even small wave function combination. Another important type of isomer is the shape isomer, illustrated by fission isomers, where the long half-life of the state is linked to a shape transition rather than a change in angular momentum. The half-life of an isomer can be longer than that of the ground state.

The greatest sensitivity to nuclear structure, through measuring of subsequent decay radiations, is achieved for isomers that decay on a μs time scale, which minimizes random events. There is only one naturally occurring, effectively stable (or quasi-stable) isomer: the 77.2 keV 9^- level in ^{180}Ta, with a half life of $> 7.1 \times 10^{15}$ years [1]. This inhibited decay leads to the storage of enormous amounts of energy in these states, 10^4 or 10^5 times greater than the energy released in chemical reactions [53].

The current challenge and potential for scientific discovery lie in understanding the formation of nuclear isomers through deeper insights into nuclear structure. This includes developing the ability to control the excitation and de-excitation of isomers, which could have extensive applications from isomer-based bombs and γ-ray lasers to clean energy sources.

The study of nuclei with isomeric states is also essential in nuclear astrophysics, as it provides critical insight into their role in the formation of elements in the universe and their contribution to the overall composition of matter [47]. Although nuclear isomers have been known for nearly a century, much remains to be understood about their influence on element formation during astrophysical nucleosynthesis, and certain isomers with distinct decay properties are expected to significantly impact these processes [23].

Nuclear isomers primarily decay through electromagnetic processes, such as γ decay or internal conversion (IC). However, some undergo decay via the strong interaction (e.g., α emission) or the weak interaction (e.g., β decay or electron capture). In certain cases, decay can also proceed via proton or neutron emission, or even nuclear fission. Isomeric states play a crucial role in determining elemental abundances in the universe, as they can interact with their ground states through thermal excitations in hot astrophysical environments. Studies have shown that a range of nuclear isomers are significantly populated during the r-process, between the first peak (mass number $A \sim 80$) and the third peak ($A \sim 195$) of elements (see Fig. 3) [47].

3.10 Beta decay

β decay is a general term for weak interactions between two neighbouring nuclear isobars (excluding the very rare phenomenon of double β decay). It occurs in three forms: β^-, β^+, and electron capture (EC) decay. The specific process of β^- is presented in

Equation 3.9 and 3.10.

$$(Z, N) \rightarrow (Z + 1, N - 1) + e^{-} + \tilde{\nu}_e \tag{3.9}$$

$$n \rightarrow p + e^{-} + \tilde{\nu}_e \tag{3.10}$$

The maximum energy available for β decay is equal to the mass difference between the parent and daughter nuclei, as expressed in Equation 3.11. The energy released in this decay is given by

$$Q_{\beta^-} = M(Z, A)c^2 - M(A, Z + 1)c^2 \tag{3.11}$$

where $M(Z, A)$ and $M(Z + 1, A)$ are the masses of the parent and daughter nuclei, respectively.

For β^+ decay it looks like as follows:

$$Q_{\beta^+} = M(Z, A)c^2 - M(A, Z - 1)c^2 - 2m_e c^2 \tag{3.12}$$

Electron capture (EC) decay can always occur, whereas β^+ decay has an energy threshold [13, 46]. The three-body nature of β decay due to the involvement of the neutrino, leads to a continuous energy spectrum for the emitted β particles.

β decays are contolled by the weak interaction, which is short-ranged significantly weaker than the other fundamental forces acting within a nucleus, such as the nuclear strong force and the electromagnetic force.

The probability of β decay depends on several factors, including the energy released in the decay, the angular momentum of the emitted particles, the nuclear charge, and the nature of the initial and final nuclear states. By the nature of the initial and final states, one refers to their quantum characteristics, such as spin, parity, nucleon configuration, and excitation energy. According to Fermi's golden rule, the transition rate between an initial and a final state is given by:

$$\lambda = \frac{2\pi}{\hbar}|M|^2 \frac{dn}{dE} \tag{3.13}$$

where E is the energy available for the final state products, $\frac{dn}{dE}$ is the density of the final states, and M is the matrix element. Conservation of angular momentum and parity, along with the properties of the initial and final states, determines the type of β decay that can occur. In Fermi decay, the emitted positron and neutrino have antiparallel spins ($S = 0$), so no orbital angular momentum is carried away. In Gamow-Teller decay, the positron and neutrino spins are parallel ($S = 1$), and one unit of angular momentum is carried away. Consequently, the transitions must satisfy the following vector addition rules:

$$I_f = I_i + L \quad \text{for Fermi transitions} \tag{3.14}$$

$$I_f = I_i + L + 1 \quad \text{for Gamow-Teller transitions} \tag{3.15}$$

The $\log_{10} ft$ value is a parameter used to characterize the probability of β decay transitions. The $log_{10} ft$ value is defined as the base-10 logarithm of the product of f and t. The quantity $\log_{10} ft$ is designed to depend only on the nuclear structure, eliminating the strong dependence on energy, which allows β transitions to be comparable across different nuclei. For this reason, it is also referred to as the *comparative half-life* or *reduced*

half-life. Here, f is the statistical rate function, accounting for the phase space available to the emitted electron (or positron), and t is the partial half-life of the β transition to a specific excited state. Typical $\log_{10} ft$ values for β transitions of different types are presented in Table 1.

Table 1: β-decay selection rules and typical $\log_{10} ft$ values, with transitions forbidden for $I_i = 0$ or $I_f = 0$ shown in parentheses [54, 55].

Transition type	L	ΔI (Fermi)	ΔI (Gamow-Teller)	$\Delta\pi$	$Log_{10}ft$
Allowed	0	0	0,1	No	3.8 - 6.0
1^{st} forbidden	1	(0),1	0,1,2	Yes	6 - 10
2^{nd} forbidden	2	(1),2	2,3	No	11 - 13
3^{rd} forbidden	3	(2),3	3,4	Yes	17 - 19
4^{th} forbidden	4	(3),4	4,5	No	> 22

The experimentally determined values of $\log_{10} ft$ can be organized according to the decay order. Such systematics are especially useful in the study of exotic nuclei, for which decay schemes are either unknown or very limited. By determining $\log_{10} ft$ values, one can gain insights into the spins and parities of the excited states populated in β decay.

In β decay, the total available energy Q_β is distributed among the kinetic energy of the electron (or positron), the kinetic energy of the neutrino, and the excitation energy of the daughter nucleus state E_x. If the decay populates a level with excitation energy E_x, the energy available to the electron and the neutrino is given by

$$E_0 = Q_\beta - E_x, \tag{3.16}$$

where E_0 represents the maximum energy of the emitted particles.

Consequently, the probability of β decay is proportional to the product

$$\lambda \propto |M|^2 \cdot f(Z, E_0) \tag{3.17}$$

where $|M|^2$ is the squared transition matrix element, which depends on the nuclear structure (i.e., whether the transition is allowed, forbidden, etc.), and $f(Z, E_0)$ is the phase space factor, describing the number of possible combinations of momenta and energies of the final-state leptons.

For allowed β decays, the phase space factor f increases strongly with E_0, approximately as E_0^5 in a simplified model that neglects all corrections. When the excitation energy E_x is large, the available energy E_0 becomes small, causing f to decrease rapidly, which strongly limits the probability of such a transition. Conversely, for small E_x, E_0 is larger, leading to a significantly higher f, so that the β decay preferentially populates low-lying excited states.

When comparing the β-decay probabilities to different levels in the daughter nucleus, in addition to $log_{10}fts$, the Gamow-Teller strengths can be used. For the pure GT decay the strength is defined as:

$$B(\text{GT}) = \frac{1}{ft} \frac{C}{\left(\frac{G_A}{G_V}\right)^2} \tag{3.18}$$

The total GT strength is defined as the sum of all individual transition strengths

$$B_{\Sigma}(GT) = \sum B_i(GT) \tag{3.19}$$

In deformed nuclei, slightly different $\log_{10} ft$ values can be observed compared to those already shown in Table 1. Considering the asymptotic quantum numbers (N, μ_z, Λ, and Ω), transitions can be classified as either *hindered* or *unhindered*. For allowed transitions, the unhindered group has $\log_{10} ft < 5.5$ [56], while the hindered group lies within $6.0 < \log_{10} ft < 6.8$ [56]. For first-forbidden transitions with $\Delta I = 0$ or 1, the values are $6.0 < \log_{10} ft < 7.7$ if unhindered, and $7.2 < \log_{10} ft < 8.3$ if hindered [56].

3.11 Electromagnetic transitions

An atomic nucleus in an excited state with energy E_i, to transition to the energetically more favorable state E_f, where $E_i > E_f$, must release excess energy. It can do this in several different ways. Firstly, it can emit the excess energy as a particle, but in that case it transforms into another nucleus. It can also emit it as a γ quantum, or by transferring it to an orbital electron. In this work excited bound states are considered, as they are the most important levels at low energies and are often populated in β decay.

The probability of a γ transition between the initial and final states, with angular momenta I_i and I_f, respectively, is given by the following formula (Equation B.72 in [57]):

$$\lambda(L) = \frac{1}{\tau} = \frac{8\pi(L+1)}{\hbar L[(2L+1)!!]^2} \left(\frac{E_\gamma}{\hbar c}\right)^{2L+1} B(ML; I_i \to I_f) \tag{3.21}$$

where τ is the mean lifetime of the state, $B(ML; I_i \to I_f)$ is the reduced transition probability, E_γ is the energy difference between the states in MeV, M specifies the character of the transition (E for electric and M for magnetic), and L is the multipole order. For $L > 0$, L corresponds to the angular momentum carried away by the photon.

The sources of the electromagnetic field are either electric or magnetic. Electric radiation is produced by oscillating charges, while magnetic radiation originates from oscillating currents or magnetic moments.

Classification based on the multipolarity of the transition, which may be dipole ($L = 1$), quadrupole ($L = 2$), octupole ($L = 3$), and so on. In this scheme, an $E1$ transition corresponds to electric dipole radiation. Nuclear electromagnetic transitions do not always occur with a single multipolarity. Multipole admixtures are common, particularly the admixture of $M1 + E2$.

As in de-excitation via particle emission, γ-ray emission must also obey selection rules. Both total angular momentum (spin) and parity are conserved. The spin conservation rule is expressed as:

$$|J_i - J_f| \leq L \leq J_i + J_f \tag{3.22}$$

where J_i is the total angular momentum (spin) of the initial (excited) state, J_f is the total angular momentum (spin) of the final state, and L is the multipolarity (angular momentum carried by the γ photon).

Parity conservation must also be satisfied:

$$\pi_\gamma(ML) = (-1)^{L+1} \tag{3.23}$$

$$\pi_\gamma(EL) = (-1)^{L} \tag{3.24}$$

As demonstrated in the above equations, electric and magnetic multipole radiation differ in their parity properties. Therefore, the parity selection rules can be summarized as follows [39]:

$$\Delta\pi = \text{No} \quad \text{for} \quad L = \text{even (electric)}, \; L = \text{odd (magnetic)} \tag{3.25}$$

$$\Delta\pi = \text{Yes} \quad \text{for} \quad L = \text{odd (electric)}, \; L = \text{even (magnetic)} \tag{3.26}$$

where $\Delta\pi$ denotes the change in parity between the initial and final states.

Finally, a selection rule for $L = 0$ states that $E0$ and $M0$ transitions are forbidden. However, $E0$ transitions can still occur through internal conversion. In contrast, $M0$ transitions do not occur at all, since magnetic monopoles do not exist in nature [58].

3.12 Internal conversion

Internal conversion is a process in which the nucleus de-excites by transferring its energy to an inner orbital electron. As a result, the emitted electron has an energy given by:

$$E_e = E_\gamma - B_e, \tag{3.27}$$

where B_e is the binding energy of the atomic electron and E_γ is the transition energy [59]. According to the above formula, the internal conversion electron spectrum consists of discrete lines. The emission of a conversion electron creates a vacancy in the inner electronic shell, which is rapidly filled by an electron from a higher orbital. The energy released in this process is emitted as characteristic X-rays, enabling the identification of the produced isotopes through their experimental observation. Alternatively, the released energy can be transferred to another atomic electron, leading to the emission of an Auger electron.

This process competes with γ-ray emission, and the competition can be quantified by the total conversion coefficient α_{tot}, defined as:

$$\alpha_{\text{tot}} = \frac{\lambda_e}{\lambda_\gamma}, \tag{3.28}$$

where λ_e and λ_γ are the partial decay time constants for internal conversion and γ-ray emission, respectively. The total decay time constant is then expressed as:

$$\lambda_{\text{tot}} = \lambda_\gamma(1 + \alpha_{\text{tot}}) = \lambda_e \left(1 + \frac{1}{\alpha_{\text{tot}}}\right). \tag{3.29}$$

Furthermore, the total conversion coefficient α_{tot} is the sum of the partial conversion coefficients corresponding to electrons from different atomic orbitals (K, L, M, ...):

$$\alpha_{\text{tot}} = \alpha_K + \alpha_L + \alpha_M + \ldots \tag{3.30}$$

Comparing experimental and theoretical internal conversion coefficients provides valuable information about the transition character (E or M) and its multipolarity. Experimentally, the coefficient is obtained by measuring the intensity ratio of conversion electrons to γ-rays, whereas the theoretical value is calculated using the formulas provided in [60]. In γ spectroscopy experiments, the internal conversion coefficient (ICC) is most often determined experimentally by comparing the intensity of the γ line with that of the associated K-shell X-ray radiation produced during conversion [61].

Internal conversion coefficients (ICC) have the following properties: they decrease rapidly with increasing transition energy and increase with multipolarity of the converted transition. Additionally, ICCs fairly increase with the atomic number Z. Therefore, for low-energy, high-multipolarity transitions, internal conversion strongly suppresses the emission of γ quanta, particularly in heavy nuclei.

In Chapter 7.6, internal conversion coefficients (ICCs) were calculated for selected transitions in the $A = 117$ isobars.

3.13 The j - 1 anomaly

In odd-A nuclei near closed shells, the coupling between a single particle and collective vibrations leads to a multiplet of states with different total angular momentum I. Among these states, the one with $I = j - 1$ is typically the lowest in energy. This $I = j - 1$ state is referred to as an *anomaly*, because in $(j)^n$ configurations short-range, attractive forces favor an $I = j$ state [12].

This preference arises from the structure of the particle-phonon interaction, where angular momentum coupling and schematic contributions favor this configuration. Only certain interaction diagrams contribute significantly, and their combined effect lowers the energy of the $I = j - 1$ state more than others. As a result, this state is energetically favored and often observed as the ground state in particle-vibration coupled systems [12].

A theoretical description of this phenomenon was presented in [12]. Alaga developed a model that accounts for this anomaly [62], which was later extended by Paar [52].

The phenomenon of coupling a three-particle (or three-hole) valence-shell cluster to quadrupole vibrations provides a valuable framework for interpreting the nuclear structure of isotopes such as ^{117}Ag, and ^{119}Ag. It is applicable to the description of excited states in nuclei far from closed shells, particularly in the mass region $A \approx 90 - 140$. These nuclei lie near closed proton or neutron shells and can be treated as systems with three valence nucleons (particles or holes) outside a closed-shell core. In this model, the three-particle (or three-hole) configuration in the valence shell couples with the collective quadrupole vibration (typically the 2^+ phonon) of the even-even core nucleus, producing producing a multiplet of excited states with characteristic spin-parity values and transition probabilities. For ^{117}Ag and ^{119}Ag, the structure arises from three proton holes below the $Z = 50$ closed shell. The resulting states exhibit a hybrid nature, partly single-particle and partly collective, and their electromagnetic transition rates (especially $E2$ transitions) can be predicted using Alaga rules extended to multi-particle configurations. This approach has shown good agreement with experimental data, explaining the observed energy levels and transition intensities, and providing insight into the interaction between single-particle motion and collective dynamics in mid-shell nuclei.

Chapter 4. Experimental Methods

The three previous chapters outlined the specific research questions this work aims to address, together with the theoretical framework employed in the data analysis. It is now time to proceed to the more practical part of the study, which begins with a key question: considering that these nuclei are exotic, short-lived, and absent from the natural environment on Earth, how can scientists produce them under laboratory conditions?

4.1 Nuclear Reactions Overview

This question is not trivial. Nuclear physicists have a wide range of nuclear reactions at their disposal, but there is no universal reaction. Each reaction has certain limitations and, more importantly, allows the production of atomic nuclei only within specific regions of the chart of nuclides.

Thus, only a few nuclear reactions are suitable for producing exotic nuclei for further study. Fig. 12 illustrates four nuclear reactions and highlights which reactions are available in specific regions.

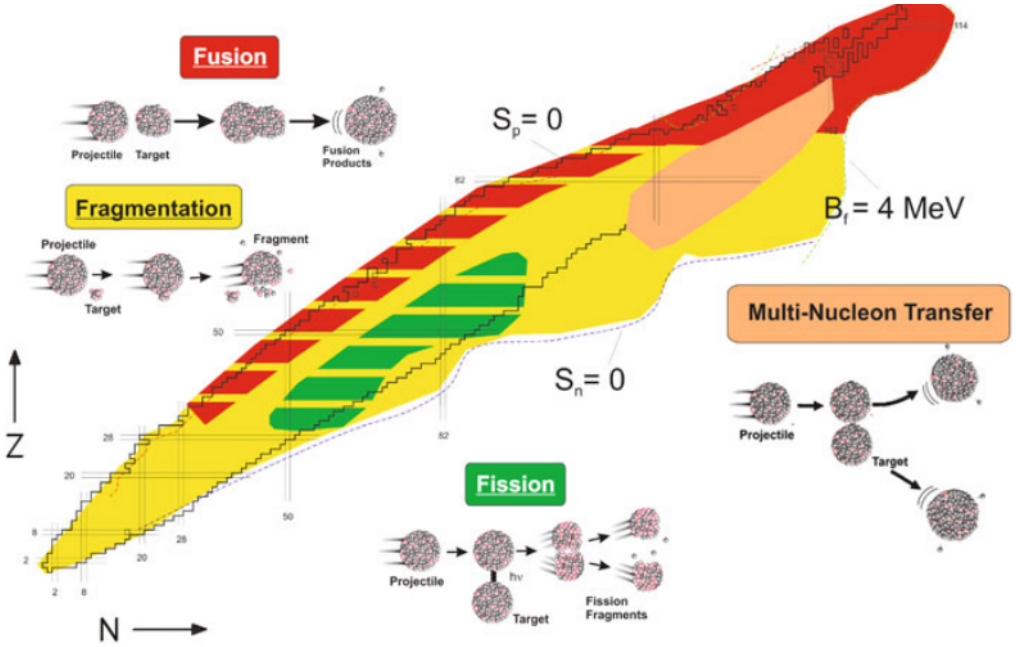

Figure 12: A schematic representation of the chart of nuclides, and a dripline where the proton sepa- ration energy and the neutron sepa- ration energy $S_{n,p} = 0$, and the regions in which exotic nuclei are primarily produced or predicted to be produced by various nuclear reactions [63].

Three of them: a fusion, a fragmentation, and a multinucleon transfer are not used for

the production of exotic neutron-rich nuclei in the mass region $A = 110$, which are the focus of this thesis. A fission reaction is the most frequently used to produce these nuclei for γ-spectroscopy studies. However, this reaction does not fully meet the requirements, because the most populated nuclei in this reaction are the less exotic ones, which have already been thoroughly studied. In contrast, the interesting, neutron-rich exotic nuclei that can be investigated using nuclear spectroscopy methods are produced with a magnitude several times lower [63]. The cross section for producing neutron-rich nuclei from technetium to palladium decreases by approximately a factor of ten for each successive isobaric shift away from the valley of stability [64].

This process involves splitting a heavier nucleus (such as ^{238}U or ^{235}U) into two fragments of comparable mass, accompanied by the emission of prompt neutrons. The nuclei resulting from fission are highly excited and de-excite primarily by emitting γ-ray quanta within a timescale of approximately 10^{-14} seconds [31]. At the same time, these nuclei have a large neutron excess relative to protons, leading to further β^- decays until stable nucleus is formed, with the gradual emission of an electron and an electron antineutrino in each decay. The daughter nucleus is usually left in an excited state and de-excites by emitting γ radiation.

Naturally, the choice of nuclear reaction determines the selection of tools employed in the experiment. Similarly, just as there is no universal nuclear reaction, there is no universal experimental setup capable of measuring all properties of exotic nuclei simultaneously. The design and effectiveness of the devices depend on the nuclear reaction mechanism, the kinematics of the reaction products, and, to some extent, the properties of the primary beam.

As mentioned earlier in this chapter, nuclear fission reactions produce a wide range of nuclei as fission fragments. The next section will therefore focus on methods for selectively separating certain nuclei from the rest.

4.2 Ion Separation Techniques

The whole production and separation process could be described as follows. The accelerator provides the primary beam (protons, deuterons, or light nuclei), generally at high energy, which is transported to the production target area. High flux neutron beams, necessary for effective induction of fission, are provided by nuclear reactors. In most cases, the actual production target is combined with an ion source, which can differ in complexity. The emergent ionized fission fragments are *purified* in a separator. By purification one means the removal of unwanted reaction products. The exotic isotope of interest is then prepared for delivery to the final experimental setup, which could be a simple set of detectors, a collector ring, or even a re-accelerator system [63].

There is two type of setup, which could be useful in this scenario, one is an in-flight method and the second one is an Isotope Separator On-Line (ISOL).

The in-flight method enables rapid separation of high-energy reaction products immediately following their production. Ions are separated based on their mass-to-charge ratio (m/q) and kinetic energy, allowing the selection of a broad range of isotopes. This technique is particularly effective for studying nuclei with very short half-lives, as the separation occurs almost immediately after the nuclear reaction, which is a primary advantage of this method. However, it is limited by lower isotopic purity and the high energy of the beam, which can complicate certain precision measurements.

In the ISOL method, ions are typically created on a high-voltage platform (around

50 kV), resulting in relatively low velocities. This allows the separator to employ room-temperature magnets and electrostatic focusing elements [63]. The method provides pure, low-energy beams of longer-lived isotopes, enabling high-precision investigations and detailed nuclear structure measurements.

In this method, reaction products are thermalized in a pure noble gas, such as helium or argon. They remain ionized in either the 1^+ or 2^+ state, depending on the element's ionization potential. A key aspect of these systems is that the stopping and thermalization of exotic ions cause significant ionization of the buffer gas. Helium is the optimal buffer gas due to its highest first ionization potential among all elements. To ensure that ionization remains confined to the buffer gas, it must be extremely pure, with impurity levels below parts per billion (ppb) [63, 65]. The ISOL offers superior isotopic purity and the ability to prepare low-energy beams suitable for detailed spectroscopic studies, but it is constrained by diffusion and ionization times, rendering it less effective for very short-lived isotopes.

In an ISOL device, exotic nuclei exit the gas cell through an orifice into a differentially pumped system, which removes the buffer gas before directing the ions to the acceleration region and as a next step into the electromagnetic separator. To enhance the acceptance of the acceleration system, a multipole ion guide captures the ions as they exit the orifice.

The separator used in the experiments, which serve as the data source for this thesis, is described in the next section.

4.3 The IGISOL

The most exotic and presently poorly known nuclei, are produced with extremely low probabilities relative to the other reaction products. For γ spectroscopy the best are purified samples, consisting of only a single nuclide, thus called *monoisotopic* samples. They are often isotopes of refractory elements (characterized by high melting points), which are difficult to produce in standard ion sources, like the one at ISOLDE (Isotope Separator On Line DEvice) located in the CERN (Switzerland). In this setup, a beam from an accelerator strikes a thick target and a number of products are formed in its interior, which remain in the target. In order to help the ions to diffuse out, the target has to be heated. This process is long enough that ions of short-lived nuclei often decay before they can be extracted.

Thus, for the study of the short-lived nuclear species the Ion Guide Isotope Separator On-Line (IGISOL) setup is a perfect choice. The IGISOL, coupled to a Penning ion trap at the Accelerator Laboratory of the University of Jyväskylä (Finland) provides a clean, monoisotopic beam perfectly suited for precise nuclear spectroscopy. Additional advantages of the IGISOL method include its non-selectivity with respect to the chemical or physical properties of the ions under study, as well as its ability to operate at room temperature. This operation at room temperature ensures high stability, allowing for continuous runs lasting several days [66].

Since fission fragments have an almost isotropic angular distribution, the projectile beam can be separated from the stopping chamber using a thin foil. The energetic fission fragments, which initially have about 1 MeV per nucleon, pass through the foil and are stopped in neutral helium. The foil has little to no impact on the number of fragments collected in the chamber, and the absence of beam-induced plasma is beneficial.

The primary ions from nuclear reactions are thermalized in flowing helium gas within a chamber (Fig. 13). In helium, the initially high charge state of the ions (about 20^+) is reduced through charge exchange reactions with helium atoms. Within microseconds,

the ions reach a 1^+ charge state and remain in this state for at least ten milliseconds [67], as helium's high ionization potential prevents neutralization through collisions with helium atoms. The main mechanisms for neutralization are diffusion to the walls and three-body collisions involving an ion, a neutral atom, and an electron produced by a projectile beam's interaction with the helium gas. Approximately 99% of the ions hit the target shield and are lost at this stage [65].

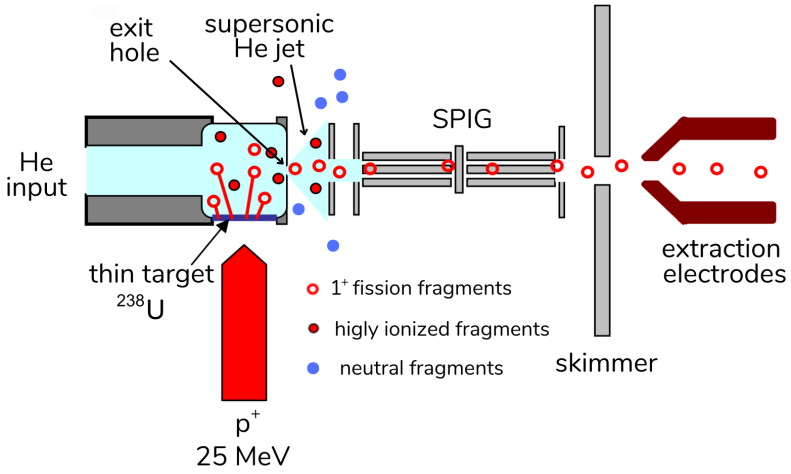

Figure 13: Diagram of the ion extraction system with a skimmer-based extraction. The reaction products leave IGISOL chamber along with the flowing helium. The ions are then focused by the electric field generated by a system of six electrodes (SPIG). Adapted from [68].

Once thermalized, the ions are carried by the helium flow from a high-pressure region of the ion guide through an exit hole (0.8 - 1.5″ in diameter) into a low-pressure region [69]. In this region, the ions are directed by an electric field into the extraction stage of the mass separator via a sextuplole ion-guide (SPIG). The sextupole structure was adopted over the quadrupole because of its ability to transport higher-current beams [69].

The neutral helium gas is removed using a Roots blower. At this stage, the beam contains nuclei of different masses, all with a 1^+ charge. The ion beam is then introduced into a magnetic dipole, where single charged fission fragments with different mass numbers A are deflected at different angles from their original paths due to the Lorentz force. A movable slit positioned precisely to allow only ions of the selected mass A to pass through.

After leaving the dipole magnet, the beam of $A \sim 110$ isobars, is directed to the RFQ system (Radio Frequency Quadrupole cooler-buncher (RFQ) [67]. The ions are slowed down to an energy of about 100 eV and bunched.

Fig. 14 presents an overview of the IGISOL experimental area at the University of Jyväskylä.

4.4 The JYFLTRAP Penning trap

The JYFLTRAP double Penning trap system is used to perform atomic mass measurements or to prepare monoisotopic ion samples for nuclear spectroscopy studies. It has been possible to achieve mass resolving power ($M/\Delta M$) of the order of 10^5 [67]. For comparison, $M/\Delta M \approx 500$ for a dipole magnet was used to select isobars.

Inside the trap, an electromagnetic field is employed to confine charged particles within a small volume, allowing ions to be cooled and stored for extended periods. Addition-

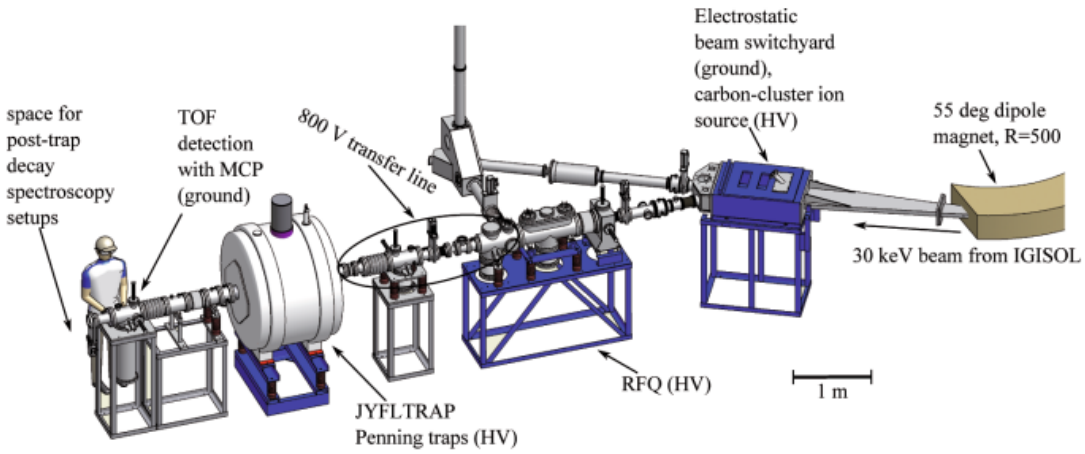

Figure 14: The IGISOL facility's experimental area included the radiofrequency quadrupole (RFQ) cooler-buncher and the JYFLTRAP Penning-trap setup. High-voltage devices are marked with (HV). A 30 keV ion beam from IGISOL enters from the right, is mass-separated by a 55° dipole magnet (with a mass resolving power of about 500), and is deflected 30° to the left by an electrostatic deflector toward the RFQ and JYFLTRAP systems [67]. The $\beta\gamma$ spectroscopy system is set up for every experiment at the left.

ally, the eigenmotions of the trapped ions can be controlled through various excitations, enabling precise isotope selection based on mass, which results in excellent mass selectivity. Another advantage of using traps is that the ions are nearly freely suspended, a feature that can be beneficial for certain spectroscopic techniques, such as measurements of conversion electrons. A typical working cycle of the ion trap lasts several hundred milliseconds (around 100 ms in an exotic nucleus β-decay experiment [70, 71]). One working cycle is sufficient to prepare a monoisotopic sample of exotic nuclei which is then sent to the $\beta\gamma$ decay spectroscopy setup.

The JYFLTRAP double Penning trap is 45 cm long and 32 mm in diameter (see Fig. 15). It consists of two parts: a purification trap and a precision trap. For isobaric purification, the single trap (purification) was used, and the other was operated in a shoot-through. The large size of the JYFLTRAP (Fig. 14), is due to the high volume of the containers for liquid nitrogen and liquid helium. The cryogenic system is required for the 7 T superconducting solenoid, inside which the Penning traps are located.

The ion trap is a device that allows charged particles to be trapped within a limited volume. A diagram of a classic Penning trap is shown in Fig. 16(a), whereas Fig. 16(b) illustrates a newer type of cylindrical Penning trap, which is part of the JYFLTRAP system. This trap contains cylindrical electrodes instead of hyperbolic ones, making it easier to quickly (several times per second) produce and release a monoisotopic sample. The increased number of electrodes, compared to a classical trap, helps shape the electric fields in a cylindrical trap, to replicate the fields in the classical trap. Consequently, the motion of the ions can be directed more efficiently, allowing the measurement of short-lived exotic nuclei, which would not be possible with the trap shown in Fig. 16(a).

The JYFLTRAP Penning trap consists of three cylindrical-shaped electrodes placed in a homogeneous magnetic field with an induction $B = 7$ T [67]. In such a field, the ions move in circles under the influence of the Lorentz force. This motion is called cyclotron motion and occurs with a cyclotron frequency ν_c:

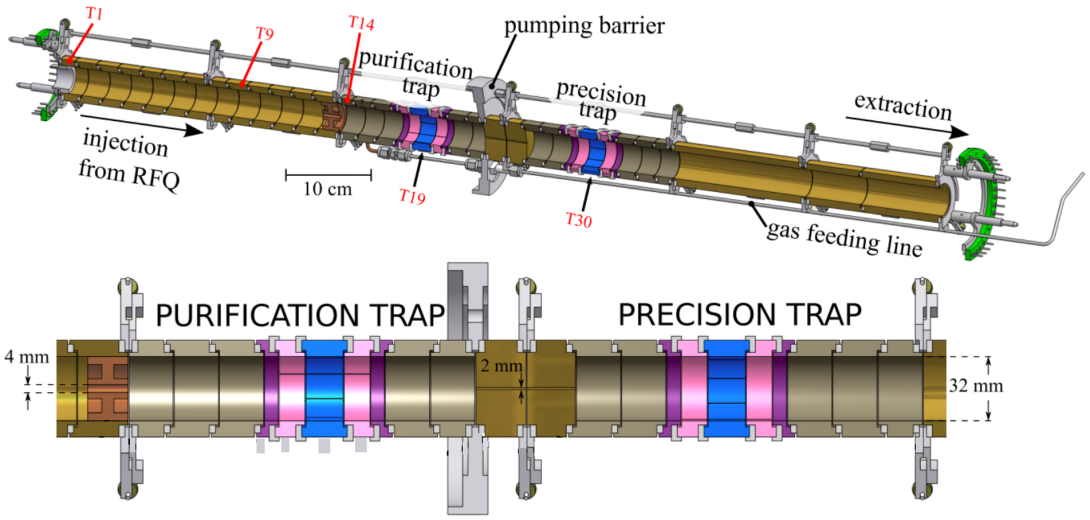

Figure 15: Schematic diagram of the JYFLTRAP double Penning trap system (adapted from [67]), consisting of several coaxial cylindrical electrodes. In this work, only the purification trap (left part of the diagram) was used.

$$\nu_c = \frac{1}{2\pi}\frac{qB}{m} \tag{4.1}$$

The cyclotron frequency ν_c depends on the magnetic field strength B and the q/m ratio [72]. The magnetic field alone is insufficient to trap the ions. An additional quadrupole electric field, generated by applying a voltage U_{dc} to the electrodes (Fig. 16), is also required. The electric potential in cylindrical coordinates is then given by:

$$V(z,\rho) = \frac{U_{\mathrm{dc}}}{4d^2}\left(2z^2 - \rho^2\right) \tag{4.2}$$

where $d = \sqrt{2z_0^2 + r_0^2}$ is defined by the trap geometry, $2z_0$ is the distance between the endcap electrodes, and r_0 is the inner radius of the ring electrode (Fig. 16).

Ions trapped in a homogeneous magnetic field B and a quadrupole electric field perform three different motions of their own (Fig. 17). The first of these, called axial motion, are oscillations along the magnetic field lines at a frequency of ν_z. The other two motions take place in a plane orthogonal to the direction of the magnetic field lines. The magnetron motion takes place with frequency ν_-, while the second corresponds to so-called *reduced cyclotron frequency* ν_+. The dependency between their values is as follows:

$$\nu_+ \gg \nu_z \gg \nu_- \tag{4.3}$$

While magnetron motion is virtually independent of the mass of the ion, reduced cyclotron frequency motion shows a strong dependence on it. The sum of the magnetron frequency and the reduced cyclotron frequency gives the cyclotron frequency ν_c

$$\nu_+ + \nu_- = \nu_c = \frac{1}{2\pi}\frac{qB}{m} \tag{4.4}$$

where q and m are the charge and mass of the trapped ion, respectively and B is magnetic induction.

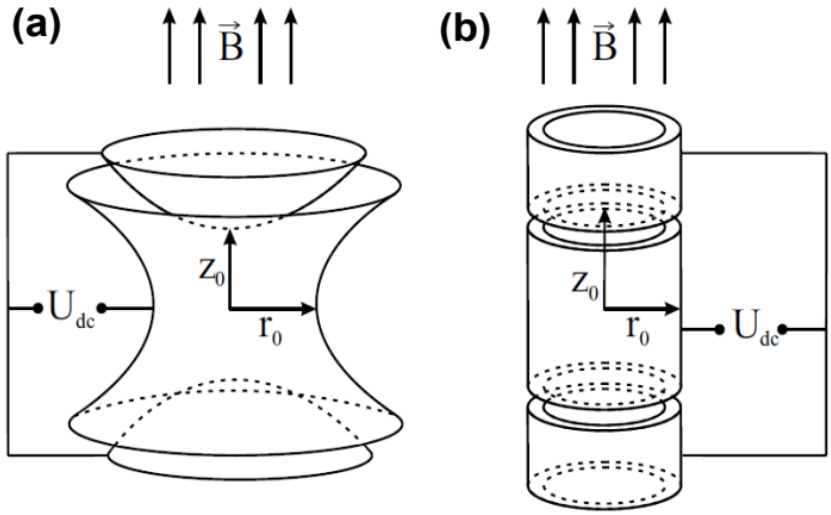

Figure 16: (a) A hyperbolical, classical Penning trap and (b) a cylindrical one [73]. The JYFLTRAP double Penning trap system uses the geometry shown in the panel (b).

In the JYFLTRAP system, the magnetic field is generated by superconducting magnets. Inside, there is an array of two Penning traps. The quadrupole electric field required to trap the ions is produced by applying appropriate voltages to the electrodes (see Fig. 15). The specific values of these voltages for ion injection, extraction, and trapping in each trap are described in [67]. A cross-section of the electrodes is shown in Fig. 18.

The separation of ions of interest is achieved by manipulating their motion within the trap. This is done by adjusting the voltages applied to different segments of the trap electrodes, as shown in Fig. 18. Each electrode is composed of eight segmented quadrants, grouped into four pairs. The effect of these excitations on ion motion depends on the type of excitation and its parameters: frequency, amplitude, and duration. In the JYFLTRAP setup, two opposing quadrants are coupled to a common RF signal, while the remaining two quadrants are maintained at a constant DC voltage [68].

As mentioned earlier, the JYFLTRAP system consists of two Penning traps, of which only the first, the purification trap, was used in this work. Using a single trap provides a mass resolving power of $M/\Delta M \approx 10^5$, which is sufficient to separate the nuclei of interest from an isobaric beam. The purification trap is filled with helium at a pressure of 10^{-4} mbar.

Ions trapped in the JYFLTRAP purification trap interact with helium atoms, gradually losing energy and thereby reducing the amplitudes of their axial and reduced cyclotron motions, while the amplitude of the magnetron motion remains essentially unchanged (see Fig. 17) [67]. Once sufficiently cooled, the motion of the ions can be manipulated by applying appropriate excitations.

To separate the isotope of interest from other isobars, a dipole excitation is applied first. A signal at the magnetron frequency ν_- is applied to one quadrant (Fig. 18) for approximately 10 ms, while a constant voltage is applied to the remaining quadrants. This increases the radius of the magnetron motion of all ions, moving them away from the trap axis and preventing them from passing through the 2 mm diameter orifice (Fig. 15) [67].

After the ions reach the desired radius, a quadrupole excitation at the cyclotron frequency ν_c is applied to two opposite quadrants, while a constant voltage is maintained on

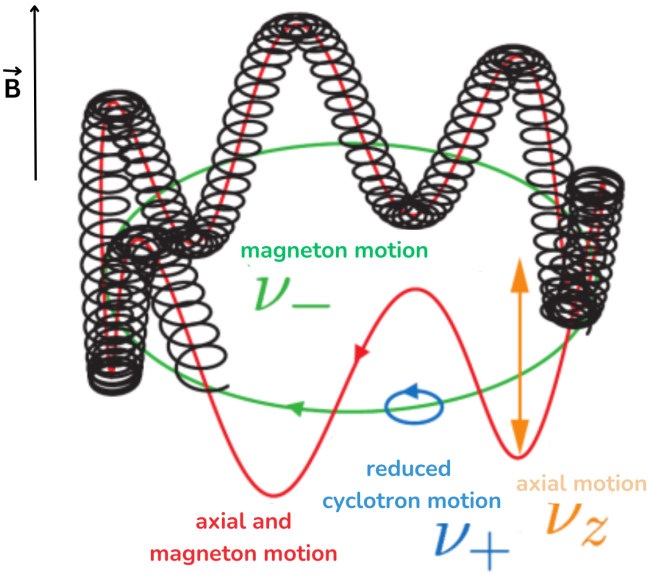

Figure 17: The motion of a charged particle in a Penning trap. The magnetic field $\vec{B}$ is directed upwards. The particle's motion, which is the combination of three different intrinsic motions, is marked in black. Adapted from [74].

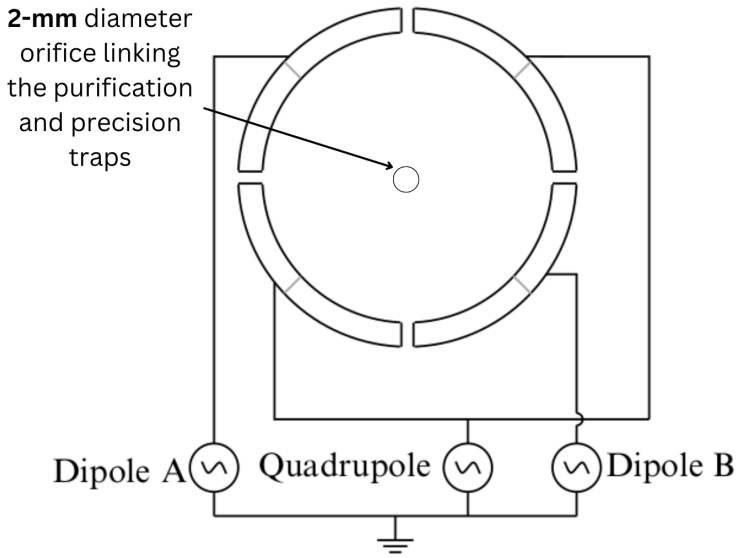

Figure 18: Cylindrical electrode (in a cross-section) generating excitation motions of the charged particle in the trap. Each quadrant consists of two segments. In the JYFLTRAP system, two quadrants are used for quadrupole excitations. For dipole excitations, one of the quadrants is used. Adapted from [67].

the other two. At this frequency, the magnetron motion and reduced cyclotron motion are coupled, allowing the slow magnetron motion to convert into fast reduced cyclotron motion. The fast-moving ions then interact with the helium gas, losing energy and reducing the amplitude of the cyclotron motion. Consequently, ions with a mass corresponding to the frequency ν_c are focused toward the trap axis, while other ions remain largely unaffected. The focused ions are extracted through the 2 mm orifice and proceed to the final γ-spectroscopy setup, whereas the remaining ions collide with the trap walls [67].

An example of the change in ion trajectories is shown in Fig. 19.

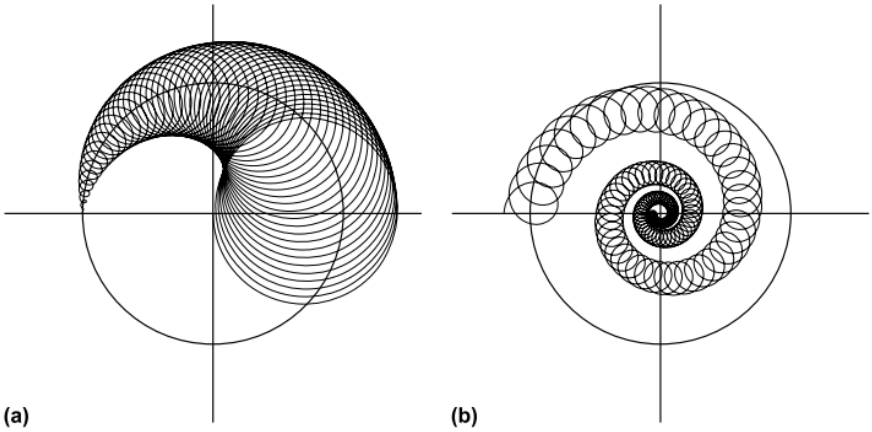

Figure 19: Ion motion in a radial plane in a buffer gas filled Penning trap (purification trap). (a) Without excitation, radius of the reduced cyclotron motion decreases and radius of the magnetron motion increases. (b) Quadrupole excitation at the resonance frequency ω_c. Due to the conversion of the magnetron motion into the reduced cyclotron motion, radii of the both motions are decreasing, because the fast reduced cyclotron motion is decreased by the buffer gas [75].

Before measuring a specific nucleus, an additional step known as a *mass scan* is performed. This procedure is used to determine the intensity of the ion beam for a selected isotope at the exit of the JYFLTRAP Penning trap. It involves varying the quadrupole excitation frequency of the ions in the trap, which focuses them along the trap axis, and recording the number of ions leaving the trap after each adjustment. Examples for isobars with mass numbers $A = 107$ and $A = 119$ are shown in Fig. 20.

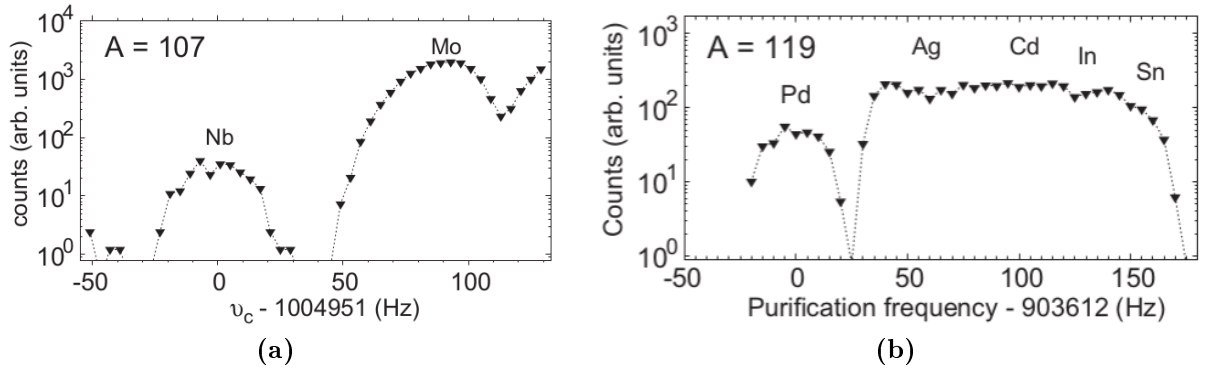

Figure 20: Ion counts registered with a MicroChannel Plate (MCP) detector placed after the Penning trap as a function of the purification frequency. The resolved atomic ions from IGISOL isobaric beam are marked with their element symbols. (a) Ion counts for ^{107}Nb β^- decay to ^{107}Mo [76], (b) and ion counts for ^{119}Pd β^- decay to ^{119}Ag [70].

Figs. 20a and 20b show the 1^+ ions of the $A = 107$ and $A = 119$ mass chains detected using the MCP detector, which is positioned outside the strong magnetic field surrounding the Penning traps. The quadrupole radio-frequency field was scanned over

a wide frequency range to determine the resonance frequency for selecting niobium and palladium ions.

4.5 Detection setup

After production and separation, the ions of the studied nucleus are transported to their final destination: the β-γ spectroscopy detection setup.

The monoisotopic samples of radioactive ions, after being released from the JYFLTRAP system, were implanted onto a movable plastic collection tape located inside a vacuum chamber. The tape was moved every few seconds (3.5 s for β decay of ^{119}Pd [70], 5 s for β decay of ^{117}Pd [71]). This interval was short enough to efficiently remove longer-lived isobars of mass $A = 107$, 117, or 119 (the β decay products of ^{107}Nb, ^{117}Pd, and ^{119}Pd, respectively), while allowing the collection of decay events for more than 14 half-lives of ^{107}Nb, more than 1 half-life of ^{117}Pd, and more than 3 half-lives of ^{119}Pd [1]. The tape has a finite length and must be rewound several times per experiment. Consequently, after some time, the Low-Energy Germanium (LEGe) detectors register a slightly elevated background radiation level, as long-lived nuclei deposited on the tape re-enter the detection area.

The detector setup included a 2-mm thick plastic scintillator and three high-resolution LEGe detectors. These detectors, featuring thin composite carbon entrance windows to enhance the transmission of low-energy γ rays, were positioned at 90° to each other, registering γ rays from the investigated samples implanted into the collection tape. The LEGe spectrometers, with an FWHM of around 0.5 keV at 20 keV, were excellent for recording low-energy γ quanta.

The scintillation detector, surrounding the implantation point, was used to detect electrons emitted in the β^- decay. By identifying these electrons, it was possible to correlate the detected γ rays with the β^- decay process. Such a time correlation (coincidence) was highly effective in reducing both natural and anthropogenic γ background radiation from the surrounding environment.

To minimize the loss of low-energy γ radiation, three thin Kapton windows were mounted into the vacuum chamber. Each of the three LEGe γ detectors was aligned with a corresponding Kapton window in the chamber.

Every interaction in a detector that produced a measurable electric signal from a preamplifier was recorded as an event by the data acquisition system. Experimental data were collected from four LEGe detectors and one scintillator detector. Each event was assigned a time stamp, allowing later analysis of time-coincidence relations between events. Logical signals from the JYFLTRAP and the collection tape driver unit were recorded as well.

The experimental data acquisition system, based on Digital Gamma Finder (DGF) modules, recorded all signals in a triggerless mode. Later, offline, the data were time-ordered and sorted into one- and two-dimensional coincidence histograms for further analysis.

A setup consisting of LEGe detectors arranged in a close geometry was used to maximize the detection efficiency of exotic decays. By analyzing the coincidence relations between the emitted γ quanta, it was possible to construct level schemes of excited states in the studied nuclei. Examples of such schemes are presented in the following chapters as Figs. 28, 32, and 40.

This setup has certain limitations. It can record γ-ray energies down to slightly below

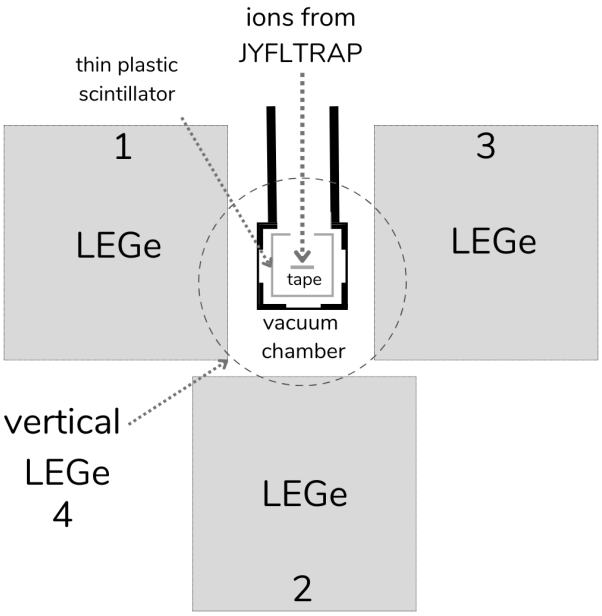

(a) Horizontal section of the detection setup, adapted from [70].

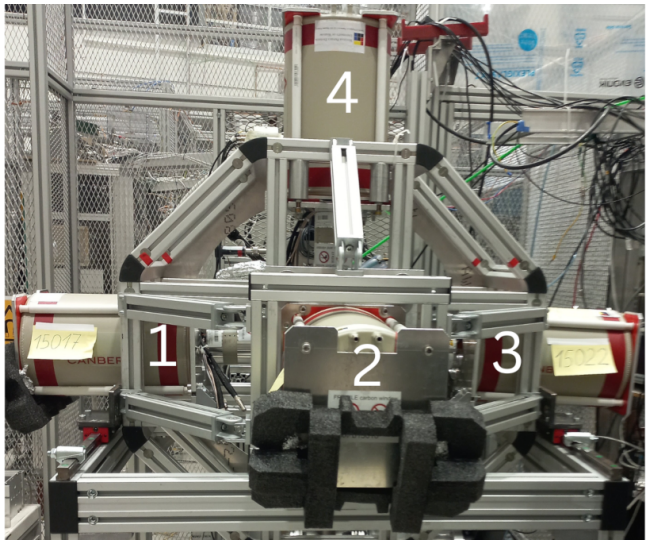

(b) Photo of the detector setup taken in September 2023.

Figure 21: (a) Ions are implanted into a movable tape. A thin plastic scintillator inside the vacuum chamber detects electrons. LEGe detectors are positioned tightly around the chamber, and the vertical detector indicated by a dotted line. (b) Photo of the detection setup taken in September 2023.

20 keV. The detection efficiency is not equal across the four detectors; it decreases with increasing distance. The detectors labeled 1 and 3 in Fig. 21 register the majority of events.

Detector 2 (Fig. 21) records slightly fewer counts than detectors 1 and 3, while the vertical detector 4 registers the lowest number of counts. This reduced efficiency is caused by the presence of the light guide of the β scintillation counter, which attenuates low-energy γ radiation. The overall layout of the experimental setup and its components is shown in Fig. 21.

Chapter 5. Spectroscopy Techniques

5.1 Singles spectra

The analysis of experimental data should begin with the basic type of spectrum, whose examination forms the starting point of the process. *Singles spectrum* is a spectrum showing all the recorded events with no additional conditions set. All γ rays, which were registered by any of the LEGe detectors can be found there.

For the experiments, the results of which are reported in the next three chapters, the spectrum displays all events from γ-rays ranging from over a dozen keV to around 2700 keV. The upper limit is caused by the fact that β decay populates the low-lying excited levels (see Chapter 3.10). Therefore, there is no need to record a wider energy range to achieve the main goal of γ-spectroscopy: producing a producing a coincidence table and a scheme of excited states in a given nucleus.

The spectrum range was set to around 2700 keV to use the 2614.5 keV peak from ^{208}Tl as an energy calibration point. The original, unmodified spectrum showed the number of counts versus channels. The singles spectra contain peaks originating from natural background radiation, which are present in any experiment, as well as various peaks from isobars corresponding to the selected mass number A. Peaks originating from the investigated nucleus may also be visible in these spectra. However, if only the ion beam passes through the IGISOL setup and the JYFLTRAP Penning trap is not used, detection of the investigated nucleus is almost impossible, as peaks from less exotic nuclei dominate the spectra. An example of such a spectrum is shown in Figure 2 of [77].

The singles spectra are characterized by excellent statistics, several orders of magnitude higher than those obtained with any gating condition (see Chapter 5.4). However, the number of peaks appearing in the spectra remains substantial.

One of the steps in the data preparation stage for analysis involves performing an energy calibration. In order to do so, commonly used calibration sources were applied: ^{152}Eu, ^{241}Am, ^{60}Co, and ^{137}Cs, as well as the strong γ lines from natural radiation, such as the 2614.5 keV line from ^{208}Tl [78, 79].

According to Appendix D in the cited source [78], natural background radiation features peaks from primordial radionuclides such as ^{40}K, ^{235}U, ^{238}U, and ^{232}Th, along with their decay products. It also includes contributions from certain common reactor activation products, nuclides formed through neutron interactions with detector and shielding materials, and characteristic fluorescence X-rays emitted by typical shielding elements.

In the book by Gilmore [78], there is also a table of NORM (Naturally Occurring Radioactive Material). It does not include γ lines classified as anthropogenic radionuclides, such as those from common calibration sources or from neutron activation produced in a nuclear reactor. In this work, only Appendix D of [78] was used.

Following the energy calibration, during the data sorting phase, a *gain matching* procedure is applied. Gain matching is the process of adjusting the amplification factors of

individual LEGe detector channels so that they produce identical responses to the same input signal, ensuring that all spectra are perfectly aligned. This step is necessary to allow the spectra to be summed in the next stage, enabling the analysis of a single combined spectrum. Each LEGe detector records the same γ quanta, and summing their signals improves the statistics and enhances the γ lines originating from exotic nuclei. The effectiveness of this procedure is demonstrated by the resolution of 2 keV for the 1332 keV γ line (from ^{60}Co), representing the optimal resolution setting for the analyzed spectrum. An example of the resulting spectrum is shown in Fig. 22.

Then, one has to identify lines originating from natural background radiation [78] as well as peaks from other isobars with the same mass, which were created in the β^- decay of the monoisotopic samples separated with JYFLTRAP.

Moreover, attention should be focused on peaks of particular interest, in particular those whose origin cannot be identified and are not listed in [1], as they may represent new transitions from the studied nuclei. The outcome of this stage of data analysis is presented in Fig. 22(a).

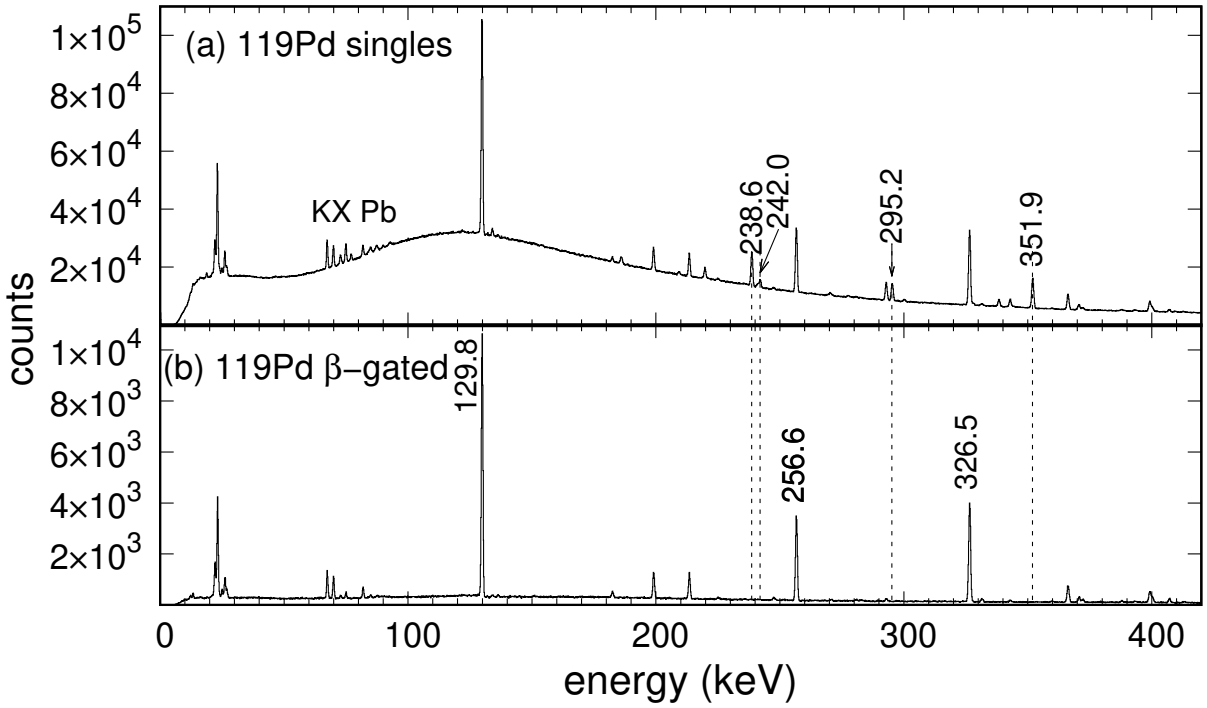

Figure 22: Example of single and β-gated spectrum for monoisotopic samples ^{119}Pd. Panel (a) shows the assigned peaks from background radiation and panel (b) presents all the γ peaks, which were not suppressed by the β coincidence condition. Marked peaks are characteristic for ^{119}Ag. Both spectra were created by summing the spectra from the four individual detectors

During the experiments, as already mentioned, four LEGe detectors recorded singles spectra, which were subsequently processed under various conditions during the data preparation phase to obtain spectra gated by β particles or γ rays (see Chapter 5.4).

5.2 Background γ radiation

Natural background radiation refers to ionizing radiation that is constantly present in the environment and originates from natural rather than anthropogenic sources [80].

Among these, cosmic radiation is a major contributor and consists primarily of protons (87%), helium nuclei (11%), as well as smaller fractions of heavier nuclei (1%) and electrons (1%) [81].

An example is ^{40}K, which is one of the 18 naturally occurring radioactive elements in the Earth's crust [81]. Its half-life is only slightly shorter than the age of the Earth [81]. Moreover, terrestrial radiation, such as that from ^{235}U, ^{238}U, and ^{232}Th, initiates a series of successive nuclear decays, resulting in the presence of 43 additional radioactive isotopes in the Earth's crust [81].

Nucleosynthesis continues to occur in the upper layers of the atmosphere through interactions with cosmic radiation. For instance, this process produces another nuclide of scientific and geological importance, ^{14}C. Specifically, ^{14}C is produced in reactions involving thermal neutrons and nitrogen nuclei [81].

Natural background radiation is a constant and unavoidable part of the environment, contributing to any kind of conducted γ-spectroscopy experiment, so this phenomenon must be kept in mind when analysing experimental data.

Using the tables provided in [78, 79], the γ lines from natural background radiation discussed in the following three chapters were identified. Each singles spectrum also contains lines resulting from the interaction of γ radiation with matter, including escape peaks associated with ^{40}K.

5.3 Characteristic X-rays and coincidence

In the case of X-rays, the situation differs from that of γ radiation, since all isotopes of a given element exhibit the same characteristic X-ray energies. This results from the fact that X-rays originate from electron transitions between atomic shells, which are identically populated in all isotopes of the same element. In [78], a table of characteristic X-ray energies that may appear in the experimental spectrum was provided, and this table served as the basis for the data analysis performed in the present work

For atomic numbers Z = 40 - 50, the energy differences between the characteristic X-rays peaks are so small that they merge in the spectra, appearing as a single broadened peak. For $Z = 41$ the difference between K_{α_2} and K_{α_1} is 0.1 keV, whereas for $Z = 49$ it is 0.2 keV.

This type of radiation occurs in the studied nuclei at around 20 keV, so it interferes with spectrum analysis, as it may mask other lines originating from the β^- decay of the monoisotopic sample. An exceptional case is a low-energy transition from an isomeric state to the ground state. However, such transitions, even if they occur, are practically invisible in γ-ray spectroscopy, because their internal conversion coefficients are high. Therefore, the level is usually de-excited through electron emission rather than through γ emission (see Chapter 3.12).

So it is a useful phenomenon. However, placing a gate on the K_{α_1}, K_{α_2}, etc., X-ray lines allows one to ensure that a given γ ray can be assigned to a specific element. Spectra gated by K_α and K_β lines are often summed to improve the statistics. It is also important to note that γ quanta escaping the vacuum chamber may interact with any material, not necessarily depositing all their energy in the detectors. X-ray lines in the spectrum could, for instance, originate from the lead shielding commonly used in experimental setups. However, this was not the case in the measurements described in this work, as no such shielding was used

However, Pb lines may be visible in any experiment anyway (as K X-rays and γ line

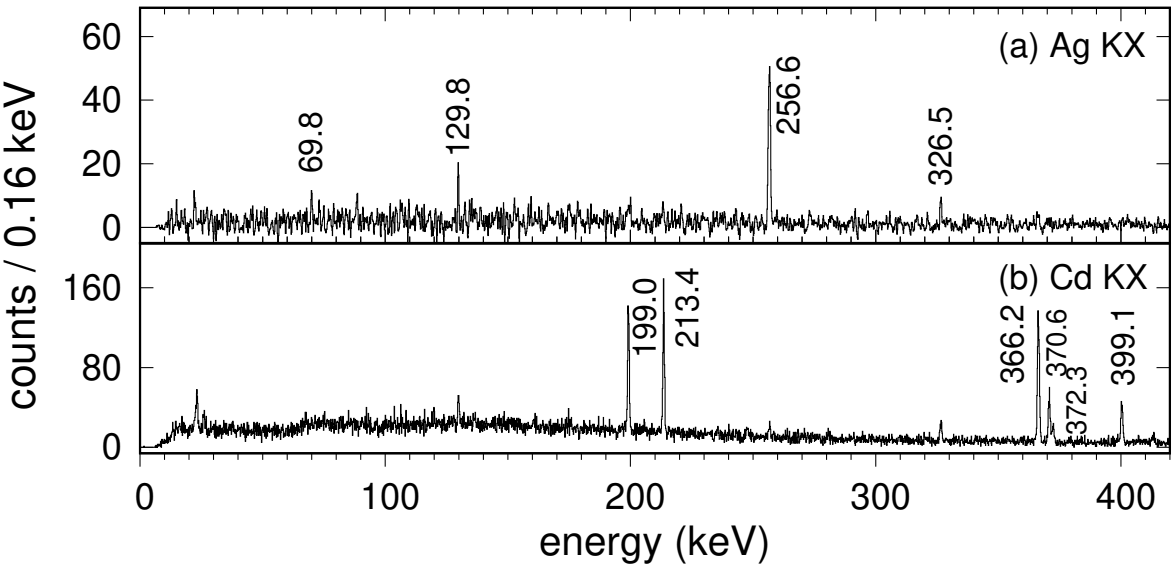

Figure 23: X-ray-gated spectra recorded using LEGe detectors for the monoisotopic samples of ^{119}Pd. The spectra shown in panels (a) and (b) are gated by the combined K_α and K_β X-rays of silver and cadmium, respectively. Each peak is annotated with its energy in keV.

of specific isotopes), even if such shielding is not used, because Pb is part of the natural radioactive decay series. Similarly, lines originating from bismuth may also appear. It is also possible to observe lines, resulting from incomplete absorption of γ-ray energy via the photoelectric effect. If a photoelectric event takes place close to the surface of the detector, some characteristic X-rays (here characteristic for germanium, so most often 9.9 keV) may escape from the detector volume. Thus the total energy absorbed in the detector would be $E_\gamma - E_{K\alpha}$ and the process is called an X-ray escape [78]. For example, if there is a strong K X-ray of palladium (21.1 keV) in a spectrum, one observes its X-ray escape peak at $21.1 - 9.9 = 11.2$ keV. Such a line appearing in the spectrum may be mistakenly interpreted as a candidate for an isomer in the studied nucleus.

Fig. 23 presents an example of an experimental spectrum in which gates were placed on the combination of K_α and K_β X-rays for silver and cadmium. The analysis of this spectrum was part of the study of the ^{119}Ag nucleus, which will be discussed further in Chapter 8.1. In Fig. 23(a), a clear coincidence of the X-ray peak with the 69.8, 129.8, 256.6, and 326.5 keV lines can be observed. This further confirms that these lines can be assigned to the scheme of excited states in the ^{119}Ag nucleus, as detailed in Tables 7, 8, and Fig. 40 in Chapter 8.3. Meanwhile, Fig. 23(b) shows lines that coincide with cadmium K X-rays. These include 199.0, 213.4, 366.2, 370.6, 372.3, and 399.1 keV. According to [1], all of these are assigned to the β decay of ^{119}Ag to ^{119}Cd.

The nuclei discussed in this thesis are very short-lived, and the analyzed spectra may contain γ lines assigned to nuclei closer to the valley of stability, as several β decays may have already occurred. For instance, in the study of the ^{119}Ag nucleus, these include γ lines belonging to ^{119}Cd (e.g., the lines visible in Fig. 23(b)), into which silver undergoes direct decay

5.4 Coincidence method

The coincidence method is based on measuring the simultaneous emission of at least two types of radiation, such as a β-ray and a γ ray, two γ rays, or a heavy particle and a γ ray. The basic case of a double coincidence is considered here. This is achieved using two counters or detectors along with a coincidence circuit to determine the simultaneity of these emissions within a resolving time τ, in the present work, the lower limit for the resolving time is limited by the hardware to 25 ns. Thus any time window length used in offline analysis is a multiple of 25 ns. As previously discussed in Chapter 4.5, the setup consists of LEGe detectors or scintillator detectors, restricting the study to β-rays and γ rays. When conducting measurements of this kind, the focus is not only on the temporal correlation between the emissions of two types of radiation but also on the energy distribution of the radiations that are time-correlated [82].

The γ-γ coincidence method is described in this section. By employing this method, one can establish the relative positioning of γ-ray transitions between nuclear excited states by gating specific transitions and analyzing the resulting one-dimensional histogram. The peaks in this histogram represent transitions that are coincident with the γ ray under study. This implies that γ rays from the same cascade of transitions between excited states appear in the coincidence spectrum for the gated γ ray.

Applying this procedure to all observed γ rays allows for the identification of nearly all transition cascades and excited nuclear states. Peaks that do not match the energy of known γ rays may indicate previously undiscovered transitions between energy levels that were not seen in the singles spectrum or the β-gated spectrum (see Fig. 22(b)). The concept of the excited levels and transitions is illustrated in Fig. 24.

Coincidence data are stored in two-dimensional matrices, which are projected onto a one-dimensional spectrum for analysis. The γ-γ coincidence gating method encompasses a set of techniques aimed at determining the relative positions of γ ray transitions by setting energy gates on specific γ rays. The γ rays that correspond to the gated transitions appear as peaks in the projected spectrum. When two γ rays are in coincidence, they are either directly connected or linked through intermediate transitions, while not in coincidence parallel transitions do not appear in the spectrum. The coincidence spectrum for a γ ray displays thus all associated transitions and excludes unrelated ones.

In the previous section, in Fig. 22(b) only visible γ quantum is this one, which was recorded by any of germanium detector, and simultaneously a β particle was recorded by the scintillation detector. Fig. 22(b) is significantly simplified, compare to Fig. 22(a) (the singles spectrum), because peaks in no coincidence with β particles disappear, the spectrum itself contains fewer peaks requiring identification. The consequence of gating on β particles is also a significant reduction in the background radiation level. However, the total number of counts across the entire spectrum also decreases. Nonetheless, the peak-to-background ratio improves, making the peaks more distinct. All lines assigned as the natural background radiation [78, 79] (238.6, 242.0, 295.2 and 351.9 keV) are not present in Fig 22(b), compare to the singles spectrum (Fig. 22(a)). Whereas if the β-gate is set these lines disappear and one can get a better look at the lines, which derive from ^{119}Ag excited scheme (129.8, 256.6 and 326.5 keV).

Analysis, which is based on this type of the spectrum, enables the creation of the excited levels schemes, which are presented in the further chapters as Figs. 28, 32 and 40.

In the coincidence spectrum obtained by setting a gate on a strong γ line, false peaks originating from so-called *backscattering* can appear. These peaks frequently appear during the analysis of coincidence spectra. They arise from strong γ lines and are associated

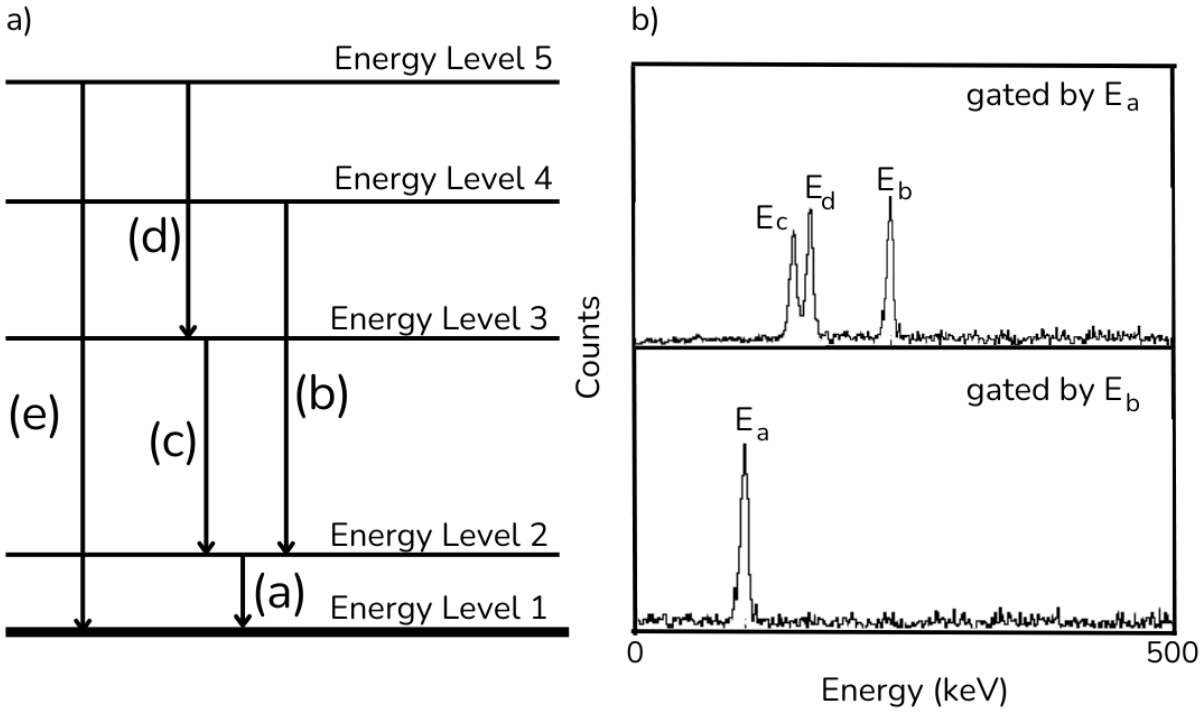

Figure 24: Panel (a) - a mock-up set of excited levels and transitions. γ rays (a) and (b) are in a coincidence, as well as (c) and (d) are. Line (a) is also in coincident with (c) and (d) lines, however not with (e). Panel (b) - coincidence spectra gated at an energy of the (a) line E_a contains (b), (c) and (d) lines, while the spectrum gated at the E_b energy only shows (a) line. Line (e) is parallel to all other transitions, hence does not appear in the spectra gated on (a), (b), (c) or (d) lines, and the spectrum gated on the (e) line shows no transitions.

with Compton scattering phenomena. An incoming γ quantum undergoes scattering, depositing part of its energy in the detector and then escaping from it. In some cases, the scattered γ quantum may enter another detector. Since this occurs within the time window typical for coincidences, a false coincidence is observed [83].

Data analysis using coincidence techniques combined with the movement of the collection tape enables effective removal of long-lived isobaric activities originating from the β-decay of isobaric chain. The method described in this chapter is crucial for γ spectroscopy of the exotic, neutron-rich nuclei. Currently, the coincidence method is one of the approaches used to determine the energy levels of radioactive nuclei [82].

5.5 Estimation of β feeding to excited levels

β feeding calculations are subject to systematic uncertainty due to the so-called *pandemonium effect* [84]. The term describes the challenges encountered when constructing a complex level scheme using high-resolution data from β decay experiments. A primary problem lies in LEGe detectors' relatively low efficiency. The level scheme is built by detecting individual γ rays and coincidences between them, so some de-excited γ rays can be missed due to a low detector efficiency. Because of this, the feeding pattern is incorrectly determined as a result of an incomplete level scheme.

The effect can be illustrated using the diagram in Fig. 25. The left panel represents the *real* scenario in this simplified case. It shows a schematic β decay that always populates

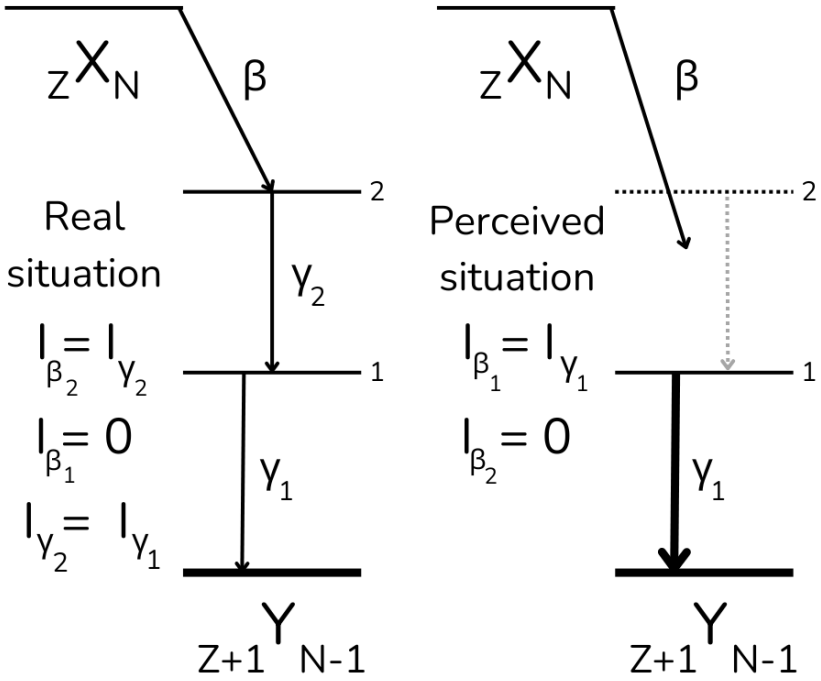

Figure 25: Schematic decay to illustrate the pandemonium effect. I_β represents the feeding (normalized to 100 %), which is determined from the intensity balance of γ rays feeding and de-exciting the level and I_γ the γ intensity [85]. See text for details.

level 2 (100% of the time). After the β decay, level 2 in the daughter nucleus de-excites via a cascade of two γ rays (γ_1 and γ_2). In a β decay experiment with LEGe detectors, the goal is to detect the γ rays de-exciting the populated levels. By analyzing the intensity balance of the γ rays populating and de-exciting the levels in the daughter nucleus, the β feeding is inferred ($I_\beta = I_{out}$ - I_{in}). Ideally, one would deduce that the feeding to level 2 ($I_{\beta_2} = I_{\gamma_2}$ - 0) is 100%, and to level 1 ($I_{\beta_1} = I_{\gamma_1}$ - I_{γ_2}) is 0%. In such an experiment, the detection setup has an efficiency for detecting each γ ray, represented by η_1 and η_2, and the probability of detecting coincidences is proportional to the product η_1 η_2. However, if the efficiency for detecting γ_2 is very low, and this transition is missed in the spectrum or the coincidence is not observed, only γ_1 will be detected, leading to the feeding being incorrectly assigned to level 1 ($I_{\beta_1} = \mathrm{I}\gamma_1$). As a result, instead of assigning the feeding to level 2 (as in the real situation), there will be an apparent 100% feeding to level 1, leading to incorrect nuclear structure information. When this occurs, one describes the decay as being affected by the pandemonium effect. The main issue, however, is that one typically cannot determine whether the decay data are actually impacted by this effect or not.

If the feeding probabilities (f = $I_\beta/100$) and the levels populated during the decay of nucleus are known, the average γ and β energies released in the decay can be calculated using the following approach:

$$\overline{E}_{\gamma,i} = \sum_j f_\beta(E_j) E_j \tag{5.1}$$

$$\overline{E}_{\beta,i} = \sum_j f_\beta(E_j) \langle E_{\beta j} \rangle \tag{5.2}$$

Here, j represents all levels populated in the daughter nucleus. The term f$\beta(Ej)$ refers to the β-feeding probability to level j, and E_j is the excitation energy of level j in the

daughter nucleus. The value $\langle E\beta_j \rangle$ represents the average energy of β particles emitted during the feeding of level j. This value only considers the energy of the β particles that populate level j and excludes the energy carried away by neutrinos. Since β particles follow a continuous energy spectrum, $\langle E\beta_j \rangle$ must be calculated separately for each populated level j.

States with high β feeding values usually have lower (more allowed) $log_{10}ft$ values, indicating that β decay to these levels is more probable and faster. Conversely, states with low β feeding often exhibit higher $log_{10}ft$ values, corresponding to more forbidden transitions.

5.6 Calculation of γ transition intensity

The intensities of the strongest γ lines present in the decay scheme of the studied nuclei (Figs. 28, 32, 40) were determined based on the singles spectrum, using the efficiency calibration curve that was previously obtained. For a small group of cases, this method could not be applied, as the lines were not sufficiently visible in the singles spectrum, being obscured by other stronger γ lines belonging to the isobar $A = 107, 117, 119$, or by lines originating from natural background radiation. To determine the intensities of such γ lines, coincidence spectra were used.

Chapter 6. β^- decay of $^{107}_{41}$Nb to $^{107}_{42}$Mo

6.1 Analysis of singles and coincidence spectra

In the γ spectra for mass $A = 107$, one can observe peaks resulting from the chain of consecutive β^- decays of monoisotopic samples of ^{107}Nb.

Three out of the four available spectra from LEGe detectors were chosen for summation. It was caused by the fact, that one of the detectors, which was placed above the vacuum chamber (detector marked as 4 in Fig. 21), was bescreened by the lightguide of the scintillator detector, so its efficiency in low-energy range was lower than others.

During data analysis, three types of spectra were taken into consideration. All of them have been described already in Chapter 5.1 and in Chapter 5.4. The first one, the singles spectrum containing all events registered by the LEGe detectors, is shown as Fig. 26(a). In contrast, Fig. 26(b) shows the γ events that coincide with β events detected in the plastic scintillator. This coincidence with β particles enhances the γ lines emitted from excited states populated by β decay, while suppressing other γ lines such as background radiation or isomeric transitions.

In the spectrum shown in Fig. 26(a), the γ lines 185.7, 238.6, 295.2, 338.3, and 351.9 keV originate from the natural background radiation [78, 79] are visible. These peaks are absent in Fig. 26(b), as the gating condition was applied to β particles, so only γ quanta detected in coincidence with β events are visible in the spectrum.

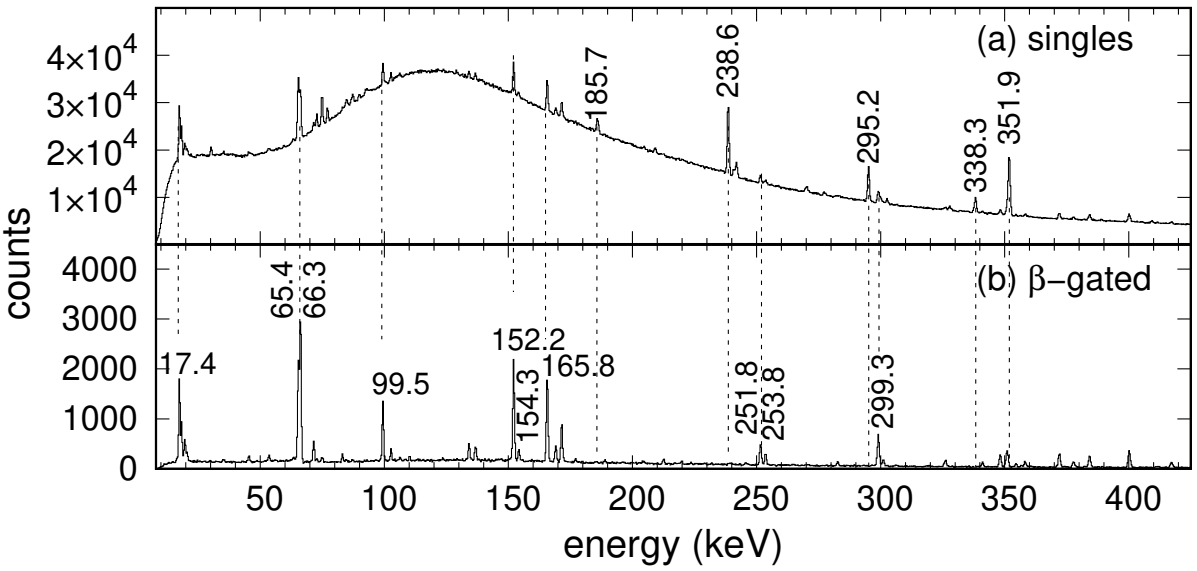

Figure 26: Singles, panel (a), and β-gated, panel (b), γ spectra registered in the LEGe detectors for the β decaying monoisotopic samples of ^{107}Nb. The peaks are marked with their energies in keV.

In the spectrum Fig. 26(b) the background level was considerably reduced by applying the β gating condition, at the same time the counting statistics was reduced approximately tenfold. Assignments can be made for peaks with energies of 17.4, 65.4, 66.3, 99.5, 152.2, 154.3, 165.8, 251.8, 253.8, and 299.3 keV. It has been determined that all these peaks came from the β decay of ^{107}Nb to ^{107}Mo and they can be found in both the singles, Fig. 26(a), and the β-gated, Fig. 26(b), spectra.

The assignment to the specific place in the level scheme was done in the data analysis process, based on the γ-γ and β-γ coincidence. Some of the above-mentioned γ lines also appear in Fig. 27, which illustrates the application of the coincidence method.

In singles and β-gated spectra, one can observe γ lines following consecutive β decays of the ^{107}Nb nuclei (selected with IGISOL and JYFLTRAP). The decay chain finally terminates at the β stability path. In this case, the γ lines come from β decays of ^{107}Nb, ^{107}Mo, ^{107}Tc, ^{107}Ru and ^{107}Rh. Additionally there are X-ray lines (emmitted from electron shells), characteristic for an element. As an example, the 17.4-keV and 19.6 keV lines are the K_α and K_β X-rays of molybdenum. K_α is visible in Fig. 26(b), but it was not included in the coincidence Table 2.

Fig. 27 highlights the coincidence data obtained from the decay of monoisotopic ^{107}Nb samples. Figs. 27(a) and 27(b) show spectra gated on the fourth- and third-most intense 99.5 keV and 152.2 keV γ-ray lines, corresponding to two distinct level structures in ^{107}Mo bands A and B, respectively.

In Fig. 27(a) there are lines 17.4, 66.3, 154.3, 251.8, 326.2, and 378.0 keV visible in the spectrum. In Fig. 27(b), a gate was set to the 152.2 keV line, and the coincident lines are: 17.4, 65.4, 147.0, 189.0, 219.9 and 326.2 keV. All γ lines, on which gates were placed to obtain an analogous spectrum to Fig. 27, are presented in Chapter 6.3 in the coincidence Table 2.

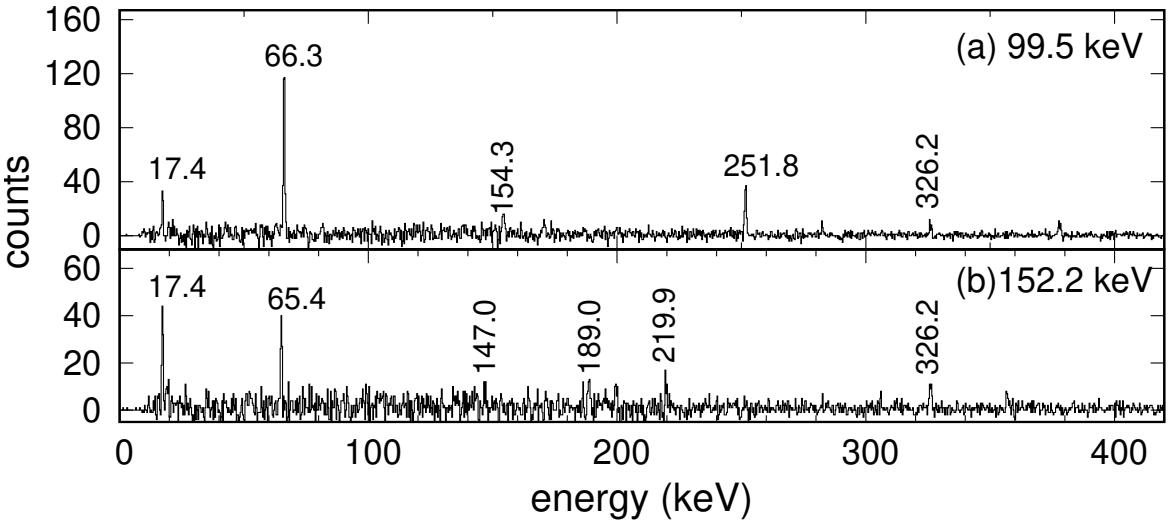

Figure 27: The coincidence γ spectra gated on the 99.5 and 152.2 keV γ lines populated in the β^- decay of ^{107}Nb. The peaks are labeled with their energies in keV.

6.2 Calculation of γ line intensity

An energy spectrum recorded with a LEGe detector consists of two main components: the background and multiple peaks superimposed on it. The background level can gener-

ally be estimated locally by fitting a straight line. This line is typically fitted to at least two background regions, located on either side of a peak (or a group of peaks). Each background region usually spans a few channels, including more channels helps reduce the uncertainty in the mean counts per channel beneath the peak.

Single spectra are most commonly used to determine the intensities of individual peaks. However, in exceptional cases, β-gated and β-γ-gated spectra are also employed to fulfill this task.

The area of a peak is determined by fitting it with a Gaussian function. Since γ peaks usually lie on a background, the peak area is calculated as the difference between the total area of the peak and the underlying background.

Peak area (number of counts in a peak) must be corrected with detector's efficiency to obtain a total number of emitted γ quanta, called γ intensity.

Sometimes emission of γ quanta is not the only way an excited state can decay (depopulate). The most common process competing with emission of γ quanta is internal conversion (IC), in which nuclear excitation energy is transferred to the electrons orbiting the atom. Information about IC has been discussed in Chapter 3.12.

To estimate total transition intensities between nuclear levels, the γ intensities (recorded with a LEGe detector) for low-energy lines were corrected for IC by using the total theoretical internal conversion coefficients [60].

The calculated γ line intensities are presented as Table 2 in the next section. Whenever one talks about the intensity of the γ transitions, the internal conversion (IC) has to be taken into account during the calculation for low-energy γ rays. Table 2 includes only the intensity of the γ lines, without correction for IC. These are relative values, where the reference point is the strongest γ line with an energy of 66.4 keV.

The intensity errors, also shown in Table 2, were determined as the square root of the area under the γ peak in the recorded singles spectrum. Additional measurement uncertainty arises from detector calibration and detection efficiency, the latter of which was addressed using standard error propagation methods. The uncertainty of the efficiency calibration curve affects the final uncertainty of the result calculated from the peak area. When converting the peak area into a physical quantity, the efficiency uncertainty from the calibration propagates together with the statistical uncertainty of the peak area, increasing the total uncertainty of the result.

Background subtraction, in practice, involves subtracting two spectra from each other (each affected by statistical uncertainty). In such a case, the uncertainties add up.

6.3 Coincidence relations and construction of the excited-level scheme

Prior to building the scheme of Fig 28, the scheme available in the databases [1] was verified. Using the current experimental data, the previous scheme was updated, adding new levels and γ lines. The new level scheme of ^{107}Mo (see Fig. 28) was prepared using coincidence relations between γ lines, their relative intensities and level systematics of neighboring nuclei.

In the ENDSF database [1], no data originating from β^- decay of ^{107}Nb to ^{107}Mo are available. However, data from other three different nuclear reactions are accessible. Notably, these include data from the spontaneous fission of ^{252}Cf [86] and ^{248}Cm [87, 88], as well as from the ^{238}U(α, Fγ) reaction [89].

The comparison between the γ lines observed in the singles and β–γ-gated spectra and those appearing in the ENDSF database [1] is presented below.

The γ lines with energies of 65.4, 66.3, and 99.5-keV are consistent with those reported in the ENDSF database within a 3σ uncertainty range. The 110.2 keV transition also matches in energy. However, in the ENDSF database, it is placed between the 458.50-keV and 348.30-keV levels, which were not observed in the present study. Therefore, this line is considered to be previously reported in the literature but assigned a new placement in the level scheme of the studied nucleus.

In contrast, 13 γ lines: 147.0, 178.5, 219.9, 251.8, 282.8, 299.3, 372.2, 351.0, 326.2, 378.0, 417.4, 448.7, 578.5-keV appear to be the newly observed transitions, not mentioned in the database. The 299.3-keV and 326.2-keV lines will be discussed later in this section.

The 152.2-keV line corresponds to a transition listed in the ENDSF database as 152.1(1)-keV. However, in that database it is placed between the 152.1-keV level and the ground state. In the present study, no such excited level was observed. The line is in mutual coincidence with the 65.4-keV γ transition and has therefore been placed higher in the level scheme, de-exciting the 217.6-keV level to 65.4 keV level. This level is populated by five other transitions, providing strong support for its existence and placement. Furthermore, the 152.2-keV transition is the only one de-exciting this level and exhibits high intensity. Based on these arguments, the 152.2-keV line is considered in this work as a transition already reported in the literature, but assigned to a different location in the level scheme. The 154.3-keV and 165.8-keV lines are included in the first of the previously described groups, alongside the 65.4, 66.3, and 99.5 keV transitions.

The 189.0-keV line had already been reported in previous experimental data, although at a different position in the level scheme between the 341.01-keV and 152.10-keV levels. Similar to the case of the 152.2-keV transition described above, in the present study this line was shifted upward by 65.4-keV. Due to the observation of coincidence only with the 152.2-keV line, which itself was reassigned to a higher energy level, all other transitions found in coincidence with 152.2-keV were likewise shifted upward in the level scheme relative to the placements given in the ENDSF database [1]. Therefore, the 189.0-keV line is classified as belonging to the second group along with 110.2 keV γ line.

The 223.7(3) keV γ line is energetically similar to the 225.6(5) keV transition, which is included in the evaluated ENDSF dataset as a transition between the 566.59 keV and 341.01 keV levels. Within a 3σ uncertainty, these transitions are energetically consistent. However, the associated energy levels differ by approximately 20 keV. In this work, the levels were determined to be 543.8 and 320.1 keV. In the dataset, the assignment of the 341.01 keV level likely stems from the presence of a 341.0(1) keV line, which de-excites this level to the ground state. The 341.2-keV line was also observed in this work, but, like the 152.2-keV line, it was incorporated into the excited level scheme at energies 65.4 keV above those listed in [1]. No 320.1-keV γ transition to the ground state was observed.

In the present study, a weak coincidence has been observed between the 223.7 keV line and the 66.3 keV and 253.8 keV transitions. The latter also appears in the ENDSF dataset, where it is placed higher in the level scheme, de-exciting the 819.81 keV level and forming a cascade with the 414.5(1) keV line, whose presence has not been confirmed in this work. This coincidence may have influenced the placement of the 225.6(6) keV and 253.7(7) keV lines in that part of the evaluated scheme. In the present study, however, the 223.7 keV transition has been placed elsewhere.

During the analysis of the 299.3 keV line, it was noted that the ENDSF dataset does not report any transitions feeding the 65.4 keV level. In contrast, Fig. 28 of this work

presents five such γ transitions. The 299.3 keV line is considered a new transition, as previously mentioned, similarly to the 147.0 keV transition.

Regarding the next transition, 306.3(1) keV, a corresponding line at 306.4 keV is listed in the ENDSF dataset. However, similarly to the 152.2 keV line, it is placed lower in the level scheme. In the present work, due to its coincidence with the 152.2 keV line which, in turn, is in coincidence with the 65.4 keV transition both lines have been shifted upward in the level scheme.

The 326.2(3) keV transition within the 66.3 keV coincidence branch corresponds to the 326.3 keV line in the ENDSF dataset and is found at the same position in the level scheme as confirmed in this study. In contrast, the 326.2 keV line within the 65.4 keV coincidence branch is a newly observed transition not previously reported.

Regarding the 341.2(1) keV line, its placement in the ENDSF dataset has already been discussed above. In this study, it has been found to be in coincidence with the 65.4 keV transition, and therefore has been assigned to de-excite to the 65.4 keV level rather than to the ground state, as was the case in the fission data of ^{248}Cm [87, 88]. The 348.5 keV transition is close in energy to the 348.3(1) keV line reported in fission data, where it de-excites directly to the ground state. However, similarly to the cascade involving the 152.2 keV transition, following the observed coincidence with the 65.4 keV line, the cascade including the 348.5 keV and 110.2 keV transitions has been shifted upward by 65.4 keV relative to its position in the ENDSF dataset [1].

Toward the conclusion, the energy of the 477.6(2) keV transition is consistent with the 478.8(1) keV line in the ENDSF dataset within a 3σ uncertainty. In the ENDSF level scheme, this line forms part of a cascade with the 189.0 keV and 341.0 keV transitions. In the present work, no coincidence with either of those lines has been observed. Instead, a coincidence was found with the 66.3 keV transition. The 341.0-keV excited level, to which this line was assigned in the ENDSF dataset, was not confirmed in this thesis. Therefore, the line was placed between the 66.3-keV and 543.8-keV levels. The existence of both of these levels is supported by numerous transitions, and the 477.6-keV γ line fits perfectly into this scheme.

As far as the excited levels are concerned, which have already been partially described above, levels 65.4, 66.3, 165.8, 320.1, 492.0 keV were present in the earlier publications [87, 88]. The other two sources of [86, 89] also featured all the levels mentioned in this paragraph, except the 65.4 keV level. In contrast, the excited levels 217.6, 364.7, 406.6, 413.9, 417.4, 437.6, 448.7, 524.0, 543.8, 644.8 keV can be considered as new levels.

Table 2 shows that the most intense γ line is the 66.3-keV transition, while the weakest observed line is the 178.5-keV transition. The 65.4-keV line exhibits the highest number of coincidences. It depopulates the level of the same energy, which forms the basis of band B in this nucleus. Four γ lines did not show any coincidences. Among them, the 417.4- and 448.7-keV transitions were assigned to the ground state, so the absence of coincidences for them is understandable. The weakest line, already mentioned above (178.5 keV), together with the 147.0-keV transition, which is the third weakest in intensity, are listed in Table 2 and shown in Fig. 28, although no coincident lines were observed in the gates set on these energies. However, the peaks representing these lines were present in the complementary gates: a gate on the strong 152.2-keV transition revealed a coincidence with the 147.0-keV line, while the 299.3-keV transition showed a coincidence with the 178.5-keV line. In five cases, the γ rays are given in parentheses, indicating that they were observed in the coincidence spectrum. However, the corresponding peaks were very weak, and thus the coincidence can be regarded as probable but not unambiguous. The 18.3 keV line arises

Table 2: The observed energies, relative intensities I_γ, suggested multipolarities, placements within the decay scheme, and coincidence relationships in the β^- decay of ^{107}Nb to ^{107}Mo are presented. The 17.4 keV and 19.6 keV energies correspond to the K_α and K_β characteristic X-rays of molybdenum, respectively, while the 18.3 keV energy corresponds to the K_α X-ray of technetium. Energies of weaker transitions are indicated in parentheses.

E$_\gamma$(keV)	I_γ	From	To	Coincident γ lines
65.4(2)[a]	77(11)	65.4	0.0	18.3, 53.6[a], 71.6[a], 83.2[a], 152.2, 299.3, 301.2[a], (341.2), 354.7[a], 358.7[a], 372.2, 384.4[a], 400.2[a], 430.3[a], 483.7[a], 784.8[a]
66.3(1)	100(5)	66.3	0.0	17.4, 99.5, 154.3, 251.8, 253.8, 326.2, 351.0, 378.0
99.5(1)	49(3)	165.8	66.3	17.4, 66.3, 154.3, 251.8, 326.2, 378.0
110.2(1)	2.8(5)	524.0	413.9	348.5
147.0(3)	2.2(5)	364.5	217.6	
152.2(1)	94(5)	217.6	65.4	17.4, 65.4, 147.0, 189.0, 219.9, 326.2
154.3(2)	15(2)	320.1	165.8	66.3, 99.5, 165.8
165.8(4)	99(5)	165.8	0.0	154.3, 251.8, 282.8, 326.2, 378.0
178.5(4)	0.6(5)	543.8	364.7	
189.0(1)	2.8(7)	406.6	217.6	152.2
219.9(2)	4.3(7)	437.6	217.6	152.2
223.7(3)	1.6(4)	543.8	320.1	(66.3), (253.8)
251.8(2)	40(3)	417.4	165.8	17.4, 66.3, 99.5, 152.2, 165.8
253.8(6)	20(2)	320.1	66.3	(17.4), 66.3, (223.7)
282.8(1)	8.0(9)	448.7	165.8	
299.3(2)	76(5)	364.5	65.4	17.4, 19.6, 65.4, 178.5
306.3(1)	3.5(7)	413.9	217.6	152.2
326.2(3)	12(3)	492.0	165.8	17.4, 66.3, 99.5, 152.2, 165.8 (**)
326.2(3)	8(2)	543.8	217.6	17.4, 66.3, 99.5, 152.2, 165.8 (*)
341.2(1)	10(1)	406.6	65.4	(17.4), 65.4
348.5(1)	35(3)	413.9	65.4	65.4, 110.2
351.0(3)	44(4)	417.4	66.3	17.4, 66.3
372.2(2)	42(3)	437.6	65.4	17.4, 65.4
378.0(2)	21(2)	543.8	165.8	66.3, 99.5, 165.8
417.4(3)	18(3)	417.4	0.0	
448.7(1)	31(3)	448.7	0.0	
477.6(2)	17(3)	543.8	66.3	(17.4), 66.3
578.5(5)	15(1.4)	644.8	66.3	17.4, 66.3

[a] Also in β decay of ^{107}Mo
(*) branch of 65.4 keV,
(**) branch of 66.3 keV

from the K_α X-ray transition in technetium.

It was examined whether the γ-ray energies listed above in Table 2 in the *Coincident*

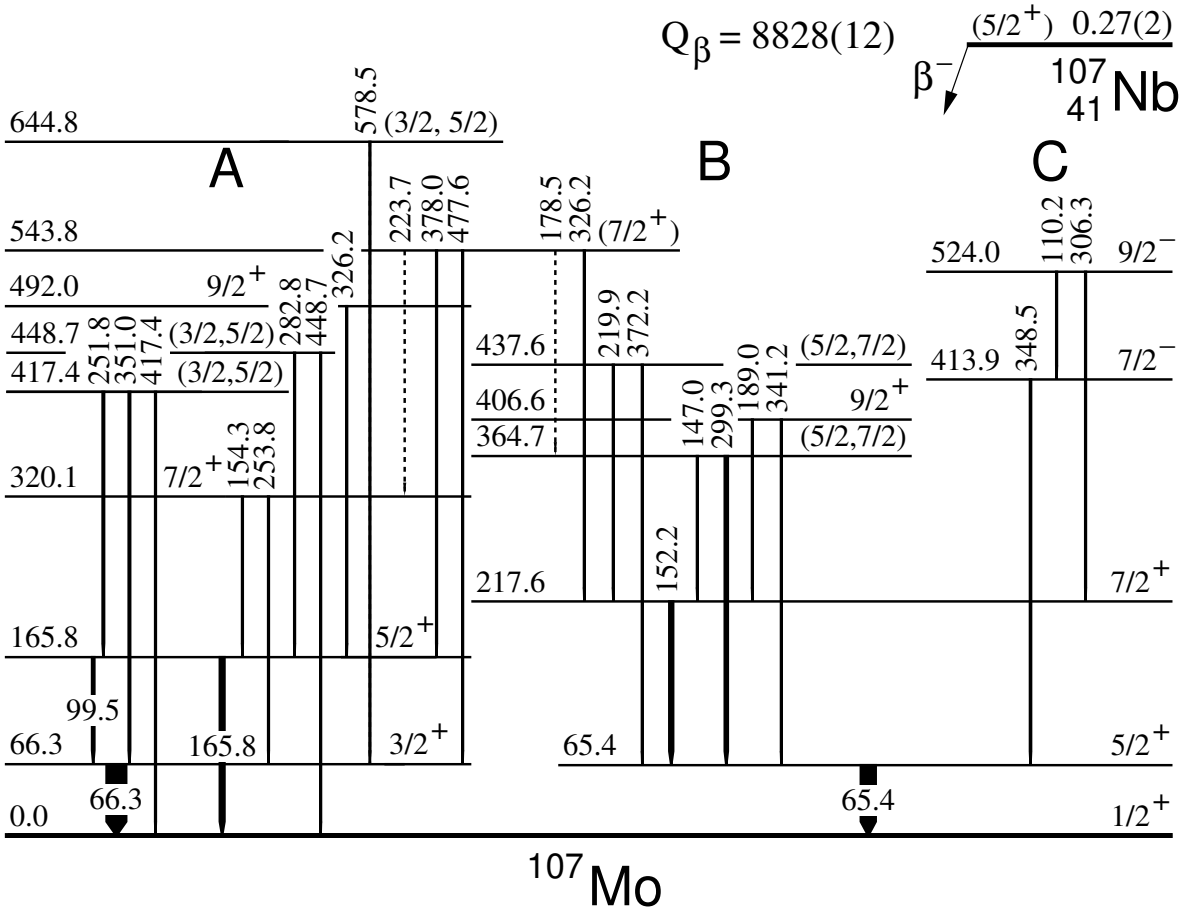

Figure 28: The β-decay scheme of ^{107}Nb to ^{107}Mo is presented, with line widths roughly corresponding to the intensities of the γ transitions. Band structures are labeled A, B, and C to aid in the discussion. The half-life value is determined in this study, while the Q_β value (in keV) is taken from [90].

γ *lines* column correspond to the energy differences between levels, and for several lines a positive match was found. However, it should be emphasized that due to the very low intensity of these γ lines, it was not possible to set an analogous coincidence gate on any of them that would unambiguously confirm the correlation between the observed transitions and the 65.4 keV line.

For these γ rays no experimental uncertainties were measured, and likewise the associated levels have no quoted uncertainties. Therefore, it was assumed that the applicable uncertainty is the same as for other γ rays in the given energy region. A 3σ test was then applied to check the consistency of the observed peak energies with the energy differences between specific levels.

One γ ray, observed in coincidence with the second most intense transition in this nucleus, has an energy consistent with the difference between the 417.4 keV and 364.7 keV levels. These levels belong to two different bands, A and B, respectively. It cannot be excluded that such a transition may occur, even though it would link two separate bands. An analogous situation is known in ^{107}Mo, represented by the weak 178.5 keV transition connecting the 543.8 keV and 364.7 keV levels.

A similar case arises for the 83.2 keV γ ray, which appeared in the coincidence spectrum when gating on the 65.4 keV transition. This line would connect the 448.7 keV level in Band A with the 364.7 keV level in band B. However, a transition of this type has already

been discussed above.

The 358.7 keV γ ray fits the energy difference between the 524 keV level of band C and the 165.8 keV level of Band A. Such a scenario is considered unlikely, since no transition linking these two bands has been observed in this nucleus.

Finally, the 384.4 keV γ ray is also consistent with this scheme. It would depopulate the 448.7 keV level in Band A to the low-lying 65.4 keV level in band B. This possibility cannot be excluded, following the same reasoning as for the 178.5 keV transition.

The fact that the largest number of coincidences is observed for the 65.4 keV γ ray, rather than for the 66.3 keV transition, arises from the different positions of these two transitions in the level scheme. This includes both coincidences with γ rays that are not placed in the level scheme (such as the four examples discussed above) and coincidences with transitions that are included in Table 2 and in the scheme, such as the 299.3 keV line. The 65.4 keV gamma line is the only line that de-excites the levels within band B. Practically, this means that almost every γ in band B occurs in coincidence with the 65.4 keV line.

On the other hand, the 66.3 keV line in Band A is only one of several lines that feed the ground state in this band. As a result, even though this line shows a higher count in the single spectrum, it does not exhibit as many coincidences as the 65.4 keV line from band B.

As a result of this study, the excited level scheme of the ^{107}Mo nucleus was extended to 28 γ ray transitions and 15 levels.

In Fig. 28 three bands are highlighted and that division was not published in [1]. The scheme also includes the proposed spins and parities of the excited levels, which will be described in more detail in the next section of this chapter.

The excitation scheme of the ^{107}Mo nucleus can be divided into three bands. Band A consists of 15 transitions and 7 excited states. The foundation of Band A is formed by three transitions: 66.3, 99.5, and 165.8 keV, which deexcite the 165.8-keV and 66.3-keV excited states. Most of the remaining lines comprising this band are in some configuration coincident with these three lines, thus enabling the energy deexcitation process to the ground state. Apart from the 66.3- and 165.8-keV lines, two other lines deexcite the excited state directly to the ground state, namely 417.4- and 448.7-keV in this band.

The 543.8-keV excited state deexcites via transitions that belong to Band A: 223.7, 378.0, or 477.6 keV. Additionally, some of these transitions are coincident with lines from Band B, specifically 178.5- and 326.2-keV. Therefore, there is a single excited state that was not assigned to any band.

Band B is not as extensive as Band A and consists of 10 transitions and 5 excited levels. In this band, all excited states are deexcited in the same manner, via γ quantum emission to the 65.4-keV state. This 65.4-keV state is then deexcited solely by the 65.4-keV line, which is more than ten times weaker than the 66.3-keV line that forms the foundation of Band A.

Finally, Band C is the least developed of all and consists of two excited states: 413.9- and 524.0-keV, as well as three γ lines: 110.2-, 306.3- keV, and 348.5- keV.

6.4 Spin and parity assignments

The spins and parities of excited levels in a daughter nucleus populated via β decay tend to be similar to that of a parent nucleus, which is typically low. In β decay, higher-energy levels in the daughter nucleus may be populated, but they tend to decay either

through multiple weak, low-energy γ rays emission or a few strong, high-energy ones. Both of which are difficult to detect with LEGe detectors due to their limited efficiency. Generally, β decay favors the population of low-spin, low-energy levels in the daughter nucleus, as it was described in Chapter 3.10.

In contrast, spontaneous fission typically produces fragments in high-spin, high-energy states that release energy via long γ ray cascades. β decay data is particularly valuable for identifying band heads and determining their position relative to the ground state, something that is often challenging to achieve using prompt γ ray measurements alone.

Publications [87, 88] reported that the ground state in ^{107}Mo has spin and parity $5/2^+$, while the first excited state has spin and parity $1/2^+$. In the present work, this assignment has been reversed. Spin and parity $1/2^+$ for the ground state of ^{107}Mo is proposed. Level of 65.4 keV gains an assignment of $5/2^+$.

[88] reported a single 65.4-keV transition in ^{107}Mo, attributed to the deexcitation of an isomeric state with a half-life of 420 ns, tentatively assigned an energy of 65.4 keV and spin-parity $1/2^+$. In this thesis the half-life of this state was not calculated, although the spin was determined to be $5/2^+$. This new assignment aligns with the systematics in Figure 6 in [76].

For the other excited levels that previously appeared in the [86, 87, 88, 89] literature, the spin and parity assignments remained the same as in the literature. The followings levels belong to this group: 66.3, 165.8, 320.1 keV.

In contrast, the subsequent excited levels, which were not present in the previously recorded data, so for the first time an assignment of individual spins and parity was made for them. Going energetically from the lowest to the highest level. The new level with an energy of 217.6 keV, as part of the band B, gained a $7/2^+$ assignment based on the fact that the γ lines that deexcite from this level feed the 65.4 keV level, which gained a $5/2^+$ assignment. A similar situation occurred for the 406.6 keV excited level, which gained a $9/2^+$ assignment based on the same rationale.

The excited levels 364.7, 417.4, 437.6, 448.7, 644.8 keV were ascribed their tentative range of spins, based on an assumption, that the most common electromagnetic transitions are $E1$, $M1$ and $E2$. All proposed spins and parities are shown in Table 3 in the next section.

6.5 Estimation of β feeding to excitation levels

To estimate experimental β feedings (I_β), one has to use absolute values of intensities and one has to take into account the fact that low-energy levels are discharged by γ radiation as well as, by electron emission in the internal conversion (IC) process. The theoretical values of internal conversion coefficients were taken from [91].

Consideration of the IC is only relevant for transition energies up to approximately 200 keV. Table 3 summarizes the outcomes of this process.

The strength of β^- feeding to a specific level is determined by balancing the γ-intensities that populate and depopulate the level. Many low-intensity γ lines are often missed by a spectroscopy setup, because of the pandemonium effect [84], so the experimental β-feeding intensities should be regarded as upper limits. The $\log_{10} f_t$ values represent lower limits. An online program [92] was used to calculate $\log_{10} ft$ values.

The highest I_β are observed for a low-lying excitation state at 65.4 keV, corresponding to $\log_{10} ft \geq 5.27$, which indicates an allowed transition, the fastest one among transitions in Table 3. Relatively large I_β values, 12, also occur at 417.4 keV, with $\log_{10} ft \geq 5.56$,

Table 3: The experimental estimates of β feedings (I_β), and the $log_{10}ft$ values for the excited levels in ^{107}Mo populated by the β^- decay of ^{107}Nb are provided. The energy levels are reported with uncertainties. The I_β values represent upper limits, while the $log_{10}ft$ values serve as the lower ones. The last column shows the proposed spins and parities.

$E_{lev}[keV]$	I_β	$log_{10}ft$	Tentative I^Π	$E_{lev}[keV]$	I_β	$log_{10}ft$	Tentative I^Π
0.0	0.0	-	$1/2^+$	413.9(1)	3.7(5)	6.07	$7/2^-$
65.4(1)	28(6)	5.27	$5/2^+$	417.4(1)	12(1)	5.56	$(3/2, 5/2)$
66.3(1)	2.6(14)	6.30	$3/2^+$	437.6(1)	5.4(6)	5.90	$(5/2, 7/2)$
165.8(1)	9.6(13)	5.71	$5/2^+$	448.7(1)	4.6(5)	5.97	$(3/2, 5/2)$
217.6(1)	9.4(11)	5.71	$7/2^+$	492.0(2)	1.4(3)	6.47	$9/2^+$
320.1(1)	4.2(5)	6.04	$7/2^+$	524.0(1)	0.8(1)	6.71	$9/2^-$
364.7(1)	9(1)	5.68	$(5/2, 7/2)$	543.8(1)	5.6(7)	5.86	$(7/2^+)$
406.6(1)	1.5(2)	6.46	$9/2^+$	644.8(1)	1.8(3)	6.33	$(3/2, 5/2)$

still indicating allowed or slightly hindered transitions. The lowest intensities, 0.8 - 1.4, are observed for higher energy states, 492.0 - 524.0 keV, with $\log_{10} ft \geq 6.4$, corresponding to first forbidden transitions. Thus, low-energy states exhibit fast and dominant β decay, whereas high-energy states are characterized by hindered, slow β decay.

When assigning the spin and parity of an excited level, the β-decay feeding to the level is considered, including the $\log_{10} ft$ value, which indicates whether the decay is allowed or forbidden and thus constrains possible changes in spin and parity. Additionally, the γ transitions depopulating the level are analyzed, focusing on the changes in spin and parity to infer the likely multipolarity. The combined consideration of β feeding and γ decay allows narrowing down the possible spin and parity assignments for the level.

6.6 Historical overview of ^{107}Mo studies

The prompt γ ray transitions in ^{107}Mo were initially observed in the spontaneous fission of ^{248}Cm [93].

A considerable number of γ lines and excited levels were already known from the evaluated database (see Chapter 6.3). However, the data from the β^- decay of ^{107}Nb to ^{107}Mo were reported for the first time in [76], which served as the basis for this thesis.

The β decay of the lighter nuclei ^{103}Nb and ^{105}Nb was reported almost 40 years earlier [94]. However, these data are not very useful for the purposes of this work, as no spin nor parity assignments were made for the excited states.

^{107}Nb and ^{107}Mo are located at neutron midshell and away from closed proton shell $Z = 50$. The following properties related to this midshell region can be found in the literature. Theoretical studies [40, 95] indicate that molybdenum isotopes near $N = 66$ exhibit γ-soft triaxial minima around $\beta_2 \approx 0.3$, potentially leading to the formation of ground-state levels. In these isotopes, a potential competition between low-lying prolate and oblate minima has been mentioned in [95]. Moreover some Hartree-Fock-Bogoliubov calculations predict an oblate ground state for ^{107}Mo [41].

As mentioned above, spin and parity assignments were not available through the β decay data, however, fortunately, better results were obtained from spontaneous fission data. In this way, molybdenum isotopes in the mass range $A = 103$ to $A = 109$ acquired these

important values [87, 88, 89].

Looking more broadly at this region of the nuclide chart, around $N = 70$, in case of molybdenum and zircon nuclei an oblate shape is present, which becomes the ground-state configuration as more neutrons are added, i.e., for $N > 70$ [40]. A theoretical work [96] on very neutron-rich zirconium and molybdenum isotopes predicts almost equal potential minima for prolate and oblate shapes.

6.7 Comparison of ^{107}Mo with neighbouring nuclei

In [76], Figure 6 presents the systematics of the first $1/2^+_1$ and second $1/2^+_2$ excited states in odd-mass isotopes of even-Z elements ranging from $Z = 40$ to $Z = 46$.

Only ruthenium and palladium isotopes had complete data within the region covered by this systematics, specifically for neutron numbers $N = 55$ to $N = 71$ for the $1/2^+_1$ state. A clear trend is observed: as neutrons are added to the nucleus, the energy of the $1/2^+_1$ state decreases, eventually becoming the ground state for ^{115}Pd, ^{117}Pd, ^{113}Ru, and ^{115}Ru. The second state shown in these systematics, $1/2^+_2$, is much less complete for ruthenium, containing only two data points, which is insufficient to confirm or disprove the trend observed for the $1/2^+_1$ state. In palladium, however, despite the lack of data for ^{115}Pd and ^{117}Pd, the $1/2^+_2$ state follows the same gradual decrease in energy across isotopes as seen for the $1/2^+_1$ state.

For molybdenum, the nucleus of primary interest in this work, only the isotopes $^{97-101}$Mo have reported data for the $1/2^+_2$ state. These three points also exhibit a downward trend similar to that observed for palladium and ruthenium, but the limited data do not allow one to determine whether this trend continues for higher neutron numbers, and therefore no definitive conclusions can be drawn. In Table 3, no other levels besides the ground state have even tentative $1/2^+$ assignments, which further restricts the possibility of making general statements. The trend line seen in palladium and ruthenium isotopes for the $1/2^+_1$ state does not appear in molybdenum or zirconium. For the three molybdenum isotopes ^{99}Mo, ^{101}Mo, and ^{107}Mo, the $1/2^+_1$ state corresponds to the ground state, consistent with the findings of this work for the latter nucleus. The only exception is ^{105}Mo, where the ground state is assigned as $5/2^-$ and the $1/2^+$ levels deviate significantly from the expected pattern. In ^{109}Mo, the $1/2^+$ level is no longer the ground state but a low-lying excited state.

Zirconium is even more scarcely documented, but, like molybdenum, exhibits a $1/2^+$ ground state in ^{97}Zr and ^{99}Zr. In summary, while certain similarities between molybdenum and neighboring elements can be observed, the comprehensive and consistent trend across a wide range of neutron numbers, clearly seen for palladium and ruthenium, cannot be established for molybdenum or zirconium. Thus, the data suggest general patterns, but they remain inconclusive for definitive systematics in this region of the nuclear chart.

Chapter 7. β^- decay of $^{117}_{46}$Pd to $^{117}_{47}$Ag

7.1 In-direct production of ^{117}Ag

In this experiment the whole separation system got set up to produce ^{117}Rh monoisotopic samples. The results on a β decay of ^{117}Rh to ^{117}Pd were presented in [16]. The results on β decay of ^{117}Pd to ^{117}Ag were presented in [71] and are highlighted in this chapter. The chain of consecutive β-decays of the monoisotopic samples of ^{117}Rh is shown in Fig. 29. In the main part of the experiment, the JYFLTRAP Penning trap was set to deliver ^{117}Rh (*trap main* in Fig. 29). There was a short measurement (*trap short* in Fig. 29) with the ion trap set to deliver ^{117}Pd samples, which decay to ^{117}Ag. Data collected in the *trap short* measurement cover almost whole $A = 117$ β^- decay chain, except for β decay of ^{117}Rh to ^{117}Pd. Thus by comparing the γ spectra for the *trap main* and *trap short* data sets, one can identify the γ lines belonging to this decay. Fig. 29 presents also spin-parities and half-lives of the ground and isomeric states in nuclei formed as a result of consecutive β^- decays, starting with ^{117}Rh, and ending with a stable nuclide ^{117}Sn. The transitions marked with an asterisk in Fig. 29 were the lines on which gates were set for the calculation of internal conversion coefficients (ICC). Output of the calculation is presented in Table 5.

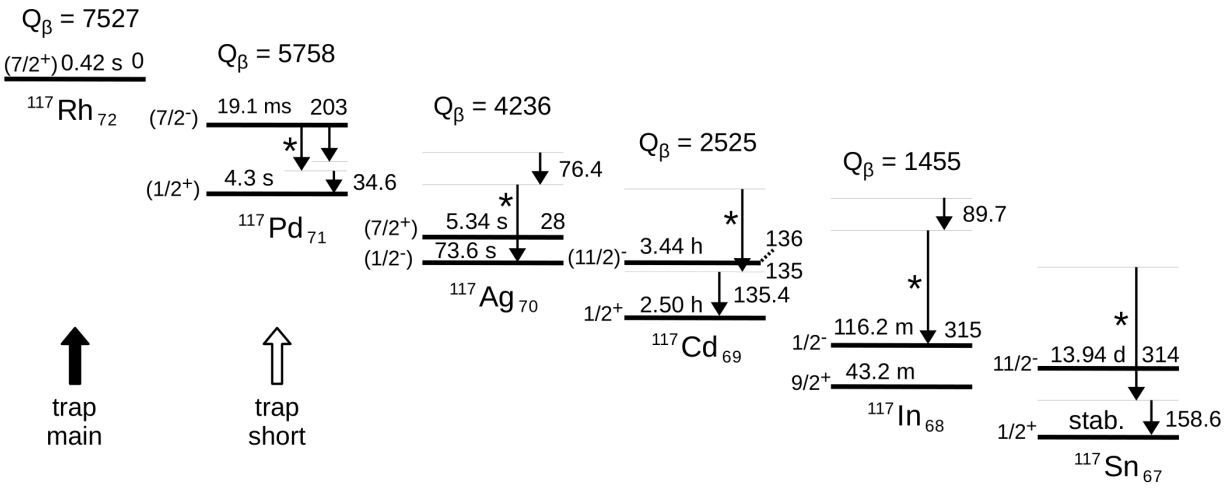

Figure 29: The selected isobars with mass number $A = 117$, along with the spins and half-lives of their ground and isomeric states, are displayed. The ^{117}Rh (*trap main*) and ^{117}Pd (*trap short*) monoisotopic samples were separated with the JYFLTRAP Penning trap. This figure is based on data from [1].

7.2 Analysis of singles and coincidence spectra

In Fig. 30(a), an example singles spectrum of the β^- decay of ^{117}Pd to ^{117}Ag in the energy range from about 10 keV to approximately 370 keV, is shown. Numerous γ ray peaks are visible, corresponding to the total absorption of these radiation quanta by the LEGe detectors. These peaks originate from $A = 117$ isobars, produced in β decay chain of monoisotopic samples delivered by the JYFLTRAP Penning trap. There are γ lines emitted by isotopes present in natural background radiation and X-ray peaks resulting from irradiation of metal parts near the measurement setup, such as the X-ray lines from lead. Additionally, the Compton continuum, resulting from partial absorption of γ-ray energy, is clearly visible in Fig. 30(a).

Both singles and γ γ, β γ coincidence spectra presented here, was recorded by 4 separate LEGe detectors (see Fig. 21), later the spectra were gain matched and summed for higher statistics. A spectrum covers an energy range from a few keV to around 2700 keV. Identification procedure of the γ lines was outlined in detail in Chapters 5.1- 5.4.

A group of the lead K X-rays (indicated as Pb X) can be seen in Fig. 30(a) as well as the 238.6 keV and 351.9 keV lines originating from natural background radiation [78, 79]. These lines do not occur in the spectrum in Fig. 30(b), where they are suppressed by the β coincidence condition.

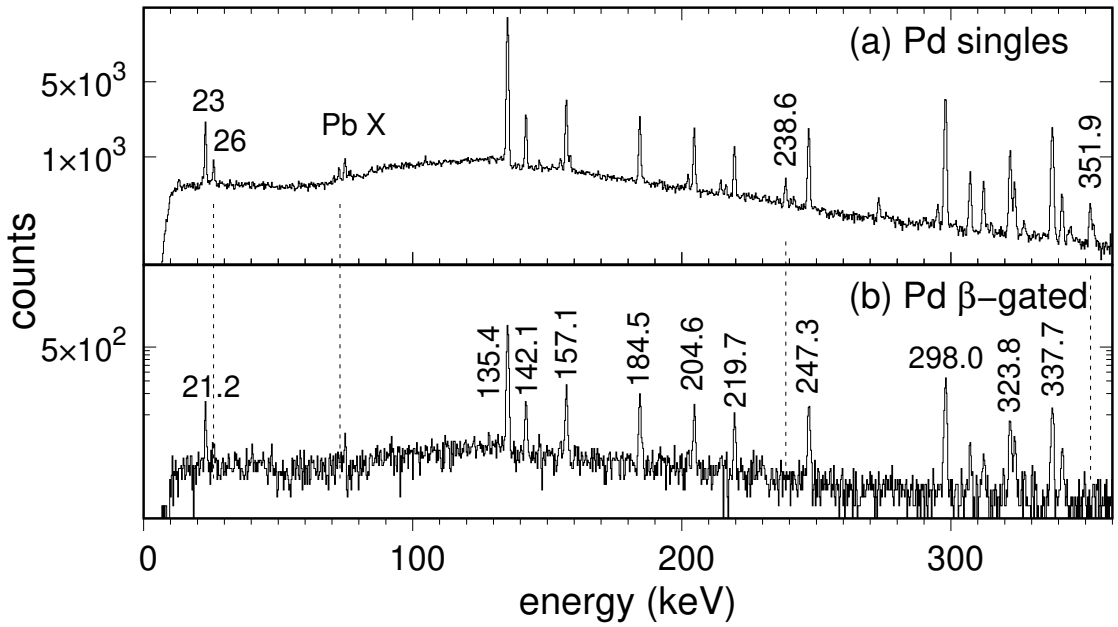

Figure 30: The spectra resulting from the β decay of ^{117}Pd to ^{117}Ag illustrate the detected γ rays in both the singles spectrum - panel (a) and the β-gated spectrum - panel (b). The peaks at 23.1 keV and 26.2 keV have been identified as the K X-ray peaks of cadmium. The vertical axes are displayed on a logarithmic scale, with peak energies labeled in keV.

Fig. 30(b) presents an example of a β-gated spectrum, in the same energy range as in the panel (a). It shows different peaks, most of which originate from one of the $A = 117$ nuclei. The number of counts displayed on the vertical axis decreases tenfold as a result of applying the gate on the registered β particles. The Compton continuum is less visible, making the analysis easier. Just like in the case of the singles spectrum, the entire β-gated spectrum is analyzed in terms of the origin of the individual peaks.

It was noticed in Fig. 30(b) that peaks 21.2, 135.4, 142.1, 157.1, 184.5, 204.6, 219.7, 247.3, 298.0, 323.8, 337.7 keV. Peaks 247.3, 323.8 keV have been classified as γ rays from the excited scheme of ^{117}Ag. Peak 21.2 keV is K X-ray from silver. Peak 135.4-keV is the strongest γ line from ^{117}Cd, also 142.1, 157.1, 184.5, 337.7 keV belong to this nucleus.

The 204.6- and 219.7-keV lines could be identified as originating from ^{117}Cd, which result from the β decay of the 5.34-s isomeric state in ^{117}Ag.

The next step of the analysis was to create coincidence spectra gated by γ rays, which were suspected to be emitted after the β^- decay of ^{117}Pd to ^{117}Ag. Dozens of spectra were created by setting additional gates on some unassigned γ line in β gated spectrum (see Fig. 30(b)). Analysis of these spectra let one verify if there are any γ lines showing coincidence relations with gated γ ray.

The coincidence method only enables to check if some γ lines could be placed in the same cascade, but one cannot check the γ transitions order this way. So a rule of thumb has an application here. A higher transition intensity means that the transition in question has to be placed at the bottom of the excited state scheme, because one presumes that the transition could be fed by weak (so not detected) γ lines.

In Fig. 31, three exemplary γ gated spectra are presented. The spectrum shown in Fig. 31(a) was obtained by gating on 247.3-keV peak. This is the strongest γ line fed by decay of ^{117}Pd nucleus, so the coincidences visible in the spectrum are clear and easy to interpret. One can call it the reference spectrum for this nucleus. After completing the full coincidence analysis, the 247.3-keV line was assigned to the very bottom of the excited-state scheme (Fig. 32), indicating that many other transitions feed the level depopulated by the 247.3-keV transition, which results in the large number of peaks visible in Fig. 31(a). The peak with energy 22.1 keV is the silver Kα X-ray line.

The γ lines in coincidence with 247.3 keV line are: 76.4, 378.0, 401.7, 522.3, 588.7, 691.7, 1701.7 and 2103.6 keV. These γ peaks are marked in the spectrum, but several other lines were also found in coincidence with the 247.3 keV line. The full list of γ lines coincidences is visible as Table 4.

Fig. 31(b) presents another example of a γ-gated spectrum, this time gated by 323.8 keV. This is also a γ line inserted at the bottom of the ^{117}Ag excited levels scheme but its intensity is approximately three times lower than the 247.3 keV γ line.

The spectrum is less clear, and background noise is more noticeable, especially in the low-energy region. The visible peaks are: 301.7, 326.1, 511.4, 671.2, 1934.3, 2070.7 keV. The 247.3 keV line is not visible in the spectrum, which indicates that these two γ lines are not in coincidence, which is confirmed by Fig. 31(a), as there is no trace of the 323.8 keV line there either.

Fig. 31(c) presents a spectrum gated by a higher-energy, lower-intensity line 1701.7 keV. Four peaks are visible in coincidence: 247.3, 323.8, 401.7 and 649.5 keV. On the other hand, γ line 1701.7 keV is present in the spectrum gated by 247.3 keV (see Fig. 31(a)) thus one can be sure that these two lines are in coincidence. Since 247.3 keV line is much more intensive as compared to 1701.7 keV, the latter was placed above the former.

A weak line of 323.8 keV in Fig. 31(c) is observed. Albeit further analysis, do not ascribed it as a member of the same cascade as 247.3 and 1701.7 keV lines. The absence of the 323.8 keV line in the spectrum gated by 247.3 keV and the absence of the 1701.7 keV peak in the spectrum gated by 323.8 keV (see Figs. 31(a) and 31(b)) indicate that these two γ transitions are not in coincidence. The origin of the 323.8 keV peak observed in Fig. 31 remains unclear. It is not attributable to the backscattering effect, as its energy exceeds the backscatter limit for a 1701.7 keV γ ray.

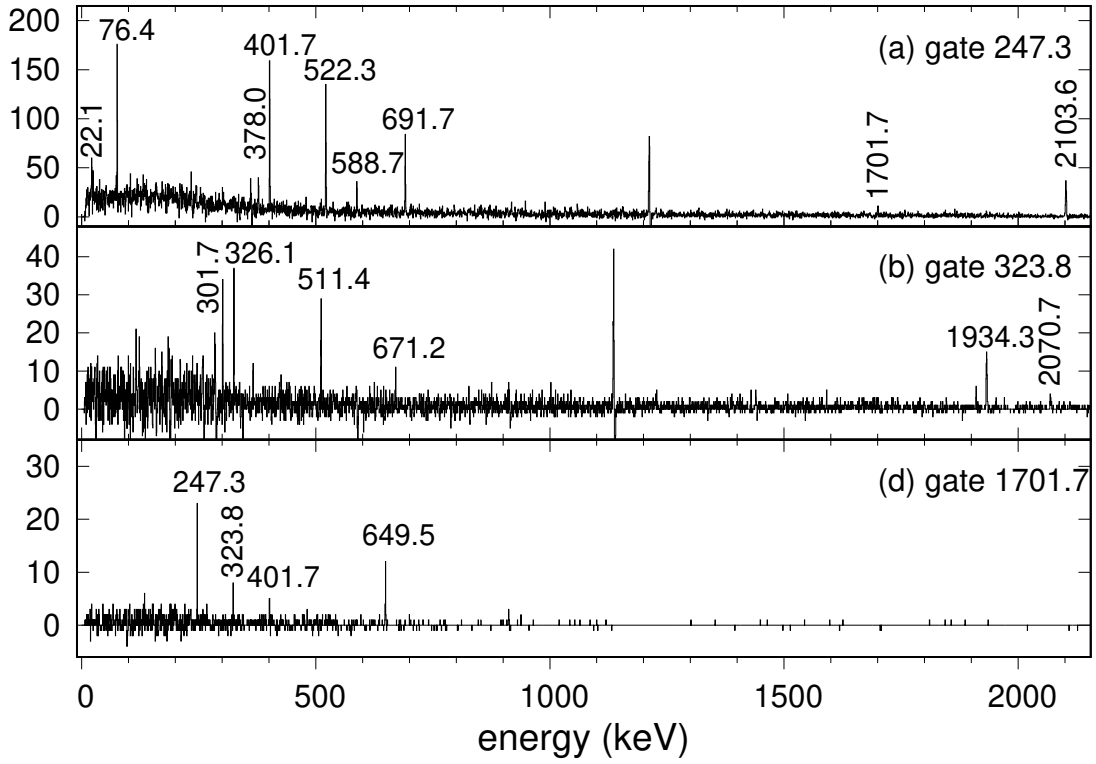

Figure 31: The γ-ray spectra are gated on specific γ lines populated by the β^- decay of ^{117}Pd. The peaks are marked with their corresponding energies in keV. In panel (a), a backscattering peak appears around 1215 keV, and at about 1140 keV in panel (b).

By reviewing many γ-gated spectra, like the ones in Fig. 31, one may deduce information on mutual coincidence relations (or lack of such relations) between investigated γ lines. This information is collected in a form of a coincidence table, Table 4 for the transitions in ^{117}Ag. Based on the coincidence relations from Table 4 a scheme of excited states in ^{117}Ag was constructed (see Fig. 32).

7.3 Calculation of γ line intensity

Experimental intensities of γ lines are given in Table 4 and were estimated with the same method as in Chapter 6.2.

Internal conversion was considered for the low-lying γ transitions in the range 76.4-326.1 keV. For the 301.7 and 326.1 keV transitions, applying the internal conversion coefficient had no impact on the calculated intensities. For the 74.6 keV transition, the intensity increased from 3.4(7) to 6.4(1.4); for 147.2 keV, from 7.0(1.0) to 8.0(1.2). The strongest γ line exhibited the largest change, rising from 100(8.1) to 103.6(8.4). Finally, for the 323.8 keV transition, the intensity varied from 34.2(3.0) to 35.1(3.0).

The inclusion of the internal conversion (IC) factor resulted in only a negligible change and was energetically relevant for just six γ lines. Therefore, it was not included in Table 4.

7.4 Coincidence relations and construction of the excited-level scheme

In the ENDSF database [1], data originating from β^- decay of ^{117}Pd to ^{117}Ag and ^{117}Ag IT decay are available [97, 98, 99].

The 28.6 keV transition that discharges the lowest lying excited state, which is suspected to be the isomeric state, appears in [99]. And it was the only transition, which was there included. In this thesis, the presence of the 28.6 keV excited level is confirmed, but the transition that discharges this level has not been measured, because the used setup did not include a device suitable to do this, like an electron conversion spectrometer known as ELLI, used in [100]. Such low-energy levels are primarily de-excited via electron emission rather than electromagnetic transitions. This phenomenon has already been addressed in Chapter 3.12.

The 76.4(1) keV line appears in the data available in [97, 98], in the same place of the excited state scheme with compatible energy. The 147.2(2) keV line appears in the same source, there is a match regarding energy value, but the line in [97, 98] was not placed in the excited levels scheme, so in this work it has gained a place of assignment between the 175.8 keV and 28.6 keV levels, perfectly aligned in energy with the gap between these levels.

The strongest γ line assigned to this nucleus 247.3(1) keV was confirmed with the literature sources, and was located in the same place in the excited state scheme. However, in this work, the measurement uncertainty has been improved by a factor of five over what was available in previous publications. The same situation, about energy value and placement was found regarding next γ line 323.8(1) keV. Line 401.7(9) keV caused problems at the analysis stage, because a γ line of similar energy appears in the neighboring ^{117}Pd nucleus with exactly the same energy. In this work, it can be identified with line 402.5(2), which appears in [97, 98], under the 3σ test concordance. In those data it was not located in the scheme, whereas in this work it gained an assignment as the line connecting the 649.5 and 247.3 keV levels. This line exhibited coincidences with two other lines, located in the scheme above and below it, thus its placement can be considered well supported by experimental evidence.

Performing the analysis for line 482.5(2) keV presented the same challenge as for the previous line. And it occurred in the same way in the β decay data [97, 98], but without entering the line into the schema structures, which was done in this work. The analogous situation and the comparisons drawn are for lines 522.3(3), 625.6(2) 629.7(3), 649.5(2) and 769.3(8)-keV. One line that appeared in [97, 98] but was not observed in this work is the 349(1)-keV line.

The 1133 keV γ line, listed in Table 4, was not included in the level scheme of Fig. 32. This line exhibits coincidences with the 498.6 keV and 625.6 keV lines, consistent with a transition connecting the 2257.7 keV and 1124.2 keV levels. However, this assignment cannot be confirmed definitively, as a gate on this line could not be established.

The 861 keV gamma line, observed in coincidence with the 522.3 keV line, cannot be unambiguously placed in the excited-state scheme. Its placement would require a level above 769.6 keV, which depopulates the 522.3 keV line, implying an additional level at 1630.6 keV. No supporting gamma transitions were observed, preventing a reliable assignment.

Similarly, the 606 keV γ line cannot be incorporated into the ^{117}Ag level scheme. It cannot correspond to a transition depopulating the 625.6 keV level via a low-lying 19 keV

Table 4: Energies, relative intensities I_γ, placement in the excited levels scheme and coincidence relations of the γ lines observed in the β^- decay of ^{117}Pd. Superscripts: ^{n} not placed in the scheme; energies of weak transitions are indicated in parentheses; $^{\mathrm{Pd}}$ visible also in ^{117}Pd; $^{\mathrm{Cd}}$ also in ^{117}Cd; ^{b} intensity in coincidence with β; ^{c} intensity estimated from γ coincidence; ^{1} seen in Ref. [100] and in this work; ^{2} seen in this work and [1]; ^{3} seen only in Ref. [100]; ^{n} not placed in the scheme

E_γ(keV)	I_γ	From	To	Coincident γ lines (keV)
$76.4(1)^{1,2}$	6.4(1.4)	323.8	247.3	247.3
$147.2(2)^{1,2}$	8.0(1.2)	175.8	28.6	482.5
$247.3(1)^{1,2}$	103.6(8.4)	247.3	0.0	22.1, 24.9, 76.4, 378.0, 401.7, 522.3, 588.7, 691.7, 919.2, 1701.7, 2103.6
$301.7(4)^{1}$	4.3(1.1)	625.6	323.8	323.1
$323.8(1)^{1,2}$	35.1(3.0)	323.8	0.0	301.7, 326.1, 511.4, 671.2, 1934.3, (2070.7)
$326.1(19)^{1,Cd}$	$2.5(0.6)^{c}$	649.5	323.8	323.8
$378.0(7)^{1}$	5.6(1.3)	625.6	247.3	247.3
$401.7(9)^{1,2,Pd}$	18.7(2.2)	649.5	247.3	247.3, (1787.7)
$482.5(2)^{1,2,Pd}$	16.9(9.4)	658.2	175.8	147.2
$498.6(6)^{2}$	6.1(1.3)	1124.2	625.6	247.3, 625.6, 1133^{n}
$511.4(6)^{1}$	$6.0(1.4)^{c}$	834.5	323.8	323.8
$522.3(3)^{1,2}$	14.4(1.7)	769.6	247.3	247.3, 861^{n}
$588.7(12)^{1,Pd}$	4.2(2.3)	834.5	247.3	247.3
$625.6(2)^{1,2}$	21.3(2.2)	625.6	0.0	498.6, 606^{n}, 1133^{n}
$629.7(3)^{1,2}$	20.3(2.1)	658.2	28.6	1599.1
$649.5(2)^{1,2}$	37.3(3.3)	649.5	0.0	1672.8, 1701.7, 1787.7
$657.8(4)^{3}$	$3.9(0.5)^{3}$	658.2	0.0	
$671.2(10)^{2}$	$2.0(0.6)^{c}$	995.0	323.8	247.3, 323.8
$691.7(4)^{1}$	9.1(2.1)	939.0	247.3	247.3
$769.3(8)^{1,2}$	6.1(0.9)	769.6	0.0	
$834.5(2)^{1}$	16.8(2.1)	834.5	0.0	
$919.2(7)^{2}$	$3.2(0.7)^{c}$	1166.5	247.3	247.3
$1599.1(10)^{2}$	14.6(1.9)	2257.7	658.2	(482.5), 629.7
$1672.8(10)^{2}$	6.9(1.6)	2322.3	649.5	247.3, 649.5
$1701.7(7)^{1}$	17.2(2.1)	2351.0	649.5	247.3, (401.7), 649.5
$1787.7(20)^{2}$	7.0(1.6)	2437.2	649.5	247.3, (401.7), 649.5
$1934.3(11)^{1}$	15.0(2.1)	2257.7	323.8	247.3, 323.8
$2070.7(10)^{2}$	3.7(1.6)	2394.5	323.8	247.3, 323.8
$2103.6(4)^{1}$	$10.6(1.6)^{b}$	2351.0	247.3	247.3

state, which has not been observed, nor does placement directly above 625.6 keV match the established energy levels. As with the previous cases, insufficient statistics prevented gating on this line to confirm a coincidence with the 625.6 keV transition.

As a result of this study, the excited level scheme of the ^{117}Ag nucleus was extended to 15 new levels and 18 new γ ray transitions.

Ultimately, Fig. 32 presents 29 γ lines, 11 of which coincide with those identified in previous analyses [97, 98] and 18 excited levels. Thus, 15 of the 18 excited levels described

in this work can be considered as new levels that were not present in the earlier literature.

The summary of all observed coincidences between individual γ lines is provided in Table 4 and illustrated in Fig. 32.

The most intense γ ray was the 247.3 keV transition, which overwhelmingly dominated the β–γ–gated spectrum. It also exhibited the largest number of coincidences with other lines assigned to ^{117}Ag. The weakest measured transition was the 326.1 keV line. However, its apparent intensity in the analyzed spectrum was elevated due to contamination from a nearby ^{117}Cd transition at 327.2(1) keV, which inflated the counts of the broadened peak. Consequently, the measured counts had to be partitioned between the two lines. Most γ rays showed coincidences with one or two other lines. Only three γ rays listed in Table 4 displayed no coincidences; each depopulates an excited state directly to the ground state, thereby reducing the coincidence probability.

Several γ rays appeared as weak, minor peaks in each gated spectrum where coincidences were observed. This was the case for the 401.7, 1787.7, and 2070.7 keV transitions.

7.5 Spin and parity assignments

For ^{117}Ag the spin-parities of the ground state and the isomeric 28.6 keV level were assigned as $(7/2^+)$ and $(1/2^-)$, respectively, by Fogelberg [99, 101]. The other spin-parities presented in Fig. 32 were adapted from Penttilä's works [98, 100]. All these low-energy levels (28.6, 175.8, 247.3, 323.8-keV) are present in odd-A silver isotopes systematics and follow a smooth trend, see the systematics drawn as Figure 16 in [70].

The placement of the $(1/2^-)$ level over the $(7/2^+)$ ground state in ^{117}Ag is supported by data from ^{252}Cf spontaneous fission (see Chapter IIIB in [71]). Observation of two cascades of γ rays, fed from two common high-spin states, enabled to determine relative positions of the $(7/2^+)$ and the $(1/2^-)$ levels as 29.6-keV. One assumes the 29.6-keV energy of the isomer, from the spontaneous fission data, is assumed to correspond to the 28.6-keV energy determined from β-decay measurements.

Further studies of this isomer (28.6 keV) are necessary, as its lifetime has not yet been measured despite multiple attempts. Care must also be taken in future investigations, since a line of nearly identical energy (28.4 keV) occurs in tin as K β X-rays, which may complicate isomeric transition studies within the $A = 117$ isobaric chain.

The strongest γ transition to the ground state, at 247.3 keV from a level with a $(3/2^-)$ assignment, corresponds to an $M1$ transition [100], consistent with the $1/2^-$ spin hypothesis. No transition from the 175.8-keV level is observed, suggesting a large spin difference and supporting the low-spin assignment for the ground state. Data from neighboring nuclei $^{107-115}$Ag, as well as ^{119}Ag, confirm the preservation of the $1/2^-$ spin hypothesis across these isotopes (see Figure 16 in [70]).

Moreover, fission is known to populate *yrast* levels (levels with the highest angular momentum at a given energy) in fission fragments [102]. The cascade populating the 29.6 keV level (see the γ intensities in Figure 6 of [71]), is much more intensive than the cascade populating the ground state in ^{117}Ag. Therefore, the spin of the 29.6 keV isomer is higher than the spin of the ground state, placing the $7/2^+$ low-lying state above the $1/2^-$ ground state.

The above conclusion on the order of the isomeric levels in ^{117}Ag, resulting from γ-spectroscopy studies, is consistent with results from a very different experimental approach reported by de Groote [103]. Using the Phase-Imaging Ion-Cyclotron-Resonance (PI-ICR) method [104] at the JYFLTRAP Penning double trap, combined with collinear

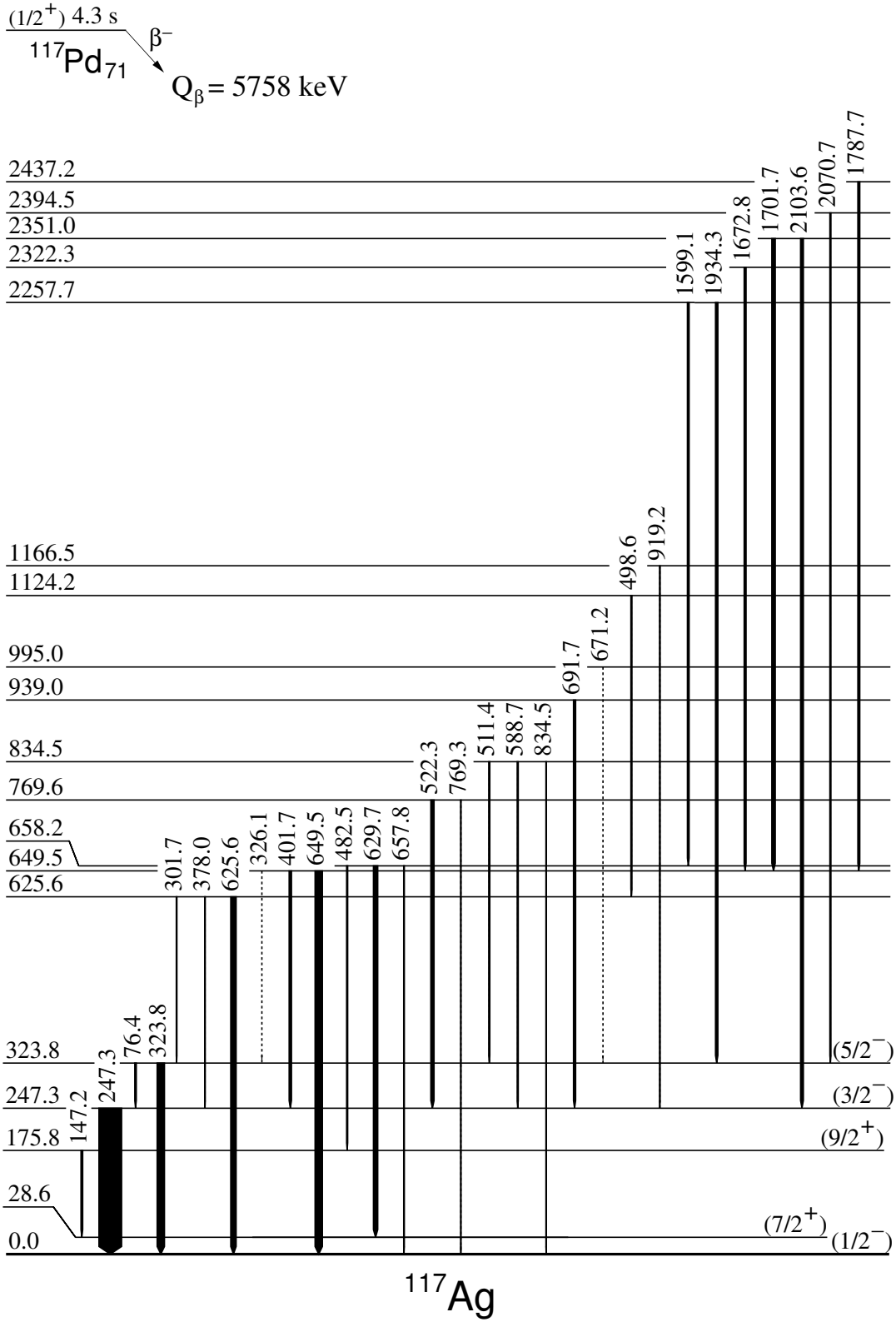

Figure 32: Scheme of excited states in ^{117}Ag populated through the β^- decay of ^{117}Pd. The ^{117}Pd nuclei were generated via the β^- decay of monoisotopic ^{117}Rh samples provided by JYFLTRAP Penning trap. The lines and excited levels energies were labeled as keV. The γ transitions with intensities below 3 have been marked with the dashed lines.

laser spectroscopy, it was determined that the $7/2^+$ level lies 29.8(31) keV above the $1/2^-$ level [103].

The ^{117}Ag ground state, assigned as $(1/2^-)$, has a low probability of being populated via β decay from the $1/2^+$ ground state of ^{117}Pd, as this decay would proceed through a first-forbidden transition (see Table 1 for theoretical considerations and Table 6 for experimental data).

The observed γ-ray transitions support the spin-parity assignment of $7/2^+$ for the 28.6-keV level in ^{117}Ag. A transition from the 175.8-keV level to the 28.6-keV level is observed, indicating that the spins of these two levels are "compatible". In contrast, no transitions are seen from the 247.3-keV and 323.8-keV levels to the 28.6-keV level, suggesting a large spin difference between them and the 28.6-keV state. Furthermore, systematics of odd-A silver isotopes in the range from ^{107}Ag to ^{115}Ag (Figure 16 in [70]) show low-energy levels with similar energies and spin assignments, consistent with the $7/2^+$ assignment for the 28.6-keV level.

The $7/2^+$ state in ^{117}Ag has a low likelihood of being populated through the β^- decay of the $1/2^+$ ground state of ^{117}Pd, because this transition would be second-forbidden (see Table 1 for theoretical considerations and Table 6 for experimental data).

Consequently, the population of the 28.6-keV level is mainly attributed to feeding by the 147.2-keV and 629.7-keV γ transitions.

The structure of excited states in the ^{117}Ag nucleus, which has been analyzed and described in this chapter, suggests a shape coexistence that materializes as two structures. One based on the prolate, $(1/2^-)$ β-decaying level, which forms the ground states in ^{117}Ag.

Such a structure, built on a weakly deformed ground state, is not unique to ^{117}Ag. It can be observed throughout the mass range $A = 107 - 121$ (see Figure 11 in [71]). It is likely that this band originates from a single proton in the $2p_{1/2}$ shell coupled to the ground state of the even-even ^{116}Pd core. This can be identified as a $1/2^-$ [301] proton configuration.

The other one forms the structure built on top of the $7/2^+$ β-decaying level at 28.6 keV. Such a structure is not unique to ^{117}Ag. It also appears in odd-A silver isotopes in the mass range $A = 107$ - 119 (see Figure 16 in [70]). This state originates from the coupling of three $\pi g_{9/2}$ proton holes to the collective Pd core. This isomer exemplifies the $j - 1$ anomalous coupling phenomenon, which will be discussed further in this chapter.

The assignment of spin and parity $(9/2^+)$ to the excited level of 175.8 keV, made already in [100, 105] and here it is maintained. It follows the trend observed in the lighter odd-A Ag nuclei (see Fig. 35). In addition, the 147.2 keV transition, which is the only one that discharges this level, feeds into the 28.6 keV level, which has gained an assignment $(7/2^+)$. The occurrence of only one transition, which depopulates this level to the $(7/2^+)$ state, confirms the $(9/2^+)$ hypothesis. On the other hand, the absence of a transition to the ground state indicates a large spin difference between these states.

Level 247.3 keV was assigned as $(3/2^-)$ and it belongs to $1/2^-$, $3/2^-$, $5/2^-$ triplets expected in odd-A Ag nuclei and presented in this work in Fig. 36d. But unfortunately the band signed as $5/2^-[303]$ is missing from the drawn systematics. The 247.3 keV level received such an assignment in [100].

The 76.4 keV transition, which de-excites the 323.8 keV excited level, is a γ transition characterized by a $M1$ multipole [100], showing that the 247.3 keV and 323.8 keV levels must differ in spin by ΔI = 1 and be assigned the same parity. So the 323.8 keV state was assigned $(5/2^-)$.

The levels at 28.6, 175.8, 247.3, 323.8, and 658.2 keV were assigned tentative spins and

parities based on spontaneous fission data reported in [71]. The remaining levels received tentative assignments based on the fact that the de-exciting transitions from a given level are most likely $E1$, $M1$, or $E2$, which effectively limits the possible spins and parities that can be assigned to that level.

7.6 Internal conversion coefficients in A = 117 nuclei

The α_K internal conversion coefficients for a few γ transitions in the $A = 117$ isobars (see Fig. 29) were determined based on the experimental data. The α_K were estimated by comparing intensities of K_α X-rays and γ rays in spectra gated by a selected γ line, shown in Fig. 33. In some cases the ICC coefficient was found for the most prominent peak in a given spectrum, (Fig. 33(c), Fig. 33(e). The obtained experimental values α_K^{exp} are compared with experimental values reported in [100] and the theoretical values from [60] in Table 5. The procedure used to determine the ICC coefficient has been outlined in Chapter 3.12.

In this work the α_K for the 34.6 keV transition in ^{117}Pd [16] was determined, by setting a gate on 168.6 keV peak (Fig. 33(a)).

The same approach was used to find an ICC for the 76.4 keV transition (not the strongest one) in ^{117}Ag (Fig. 33(b)). The gate was set to the strongest line in ^{117}Ag excited scheme: 247.3 keV line. The obtained α_K value of 0.82 is compared with a value of 0.57(10) for this transition, measured with IGISOL isotope separator only [100].

It was logical to examine the multipolarity of the 247.3 keV line. In this work, it was not possible, because the 1701.7 keV γ line, which has the highest intensity among the lines in coincidence with 247.3 keV, was too weak to allow this. The multipolarity of this transition was, however, determined in [100] and was established as $M1/E2$.

For ^{117}Cd an ICC for the 135.4 keV line was estimated using a γ spectrum gated by the line 386.8 keV. An ICC for the 89.7 keV line in ^{117}In was found using a spectrum gated by the 344.4 keV line. Finally, the α_K ICC for the 158.6 keV line in ^{117}Sn nuclide was determined using a spectrum gated by the 552.9 keV peak.

In 3 out of 5 cases, the calculated coefficients agree with the previously measured experimental α_K^{exp} coefficients.

In the case of ^{117}Pd, the counted result agrees with the previous findings that were made in [100]. Under the 3 σ test, the calculated ICC coefficient for ^{117}Ag also agrees with the experimental values included in [100]. A consistency of results was also obtained for ^{117}In. In contrast, a different multipolarity of the γ transition was counted for the 135.4 keV line in ^{117}Cd. The calculated coefficient was twice as low as in [101]. And the 158.6 keV line in ^{117}Sn has been assigned as $E1$.

7.7 Estimation of β feeding to excited levels

It must now be considered which states in ^{117}Pd β feed the excited states in the nucleus studied in this Chapter. In total two such states have been identified in ^{117}Pd. One is the ground state of ^{117}Pd with $T_{1/2} = 4.3(3)$ s [98], currently assigned a spin of $1/2^+$ [16], whereas earlier it was assigned $3/2^+$ [106] or $(5/2^+)$ [107]. Therefore, one must account for the fact that the spin of this level has changed, which directly affects the spins of the levels it could populate in the ^{117}Ag structure.

The second level feeding the structures of the nucleus studied in this chapter is an isomer with $T_{1/2} = 19.1$ ms, assigned spin-parity $7/2^-$ [16]. Unfortunately, due to such

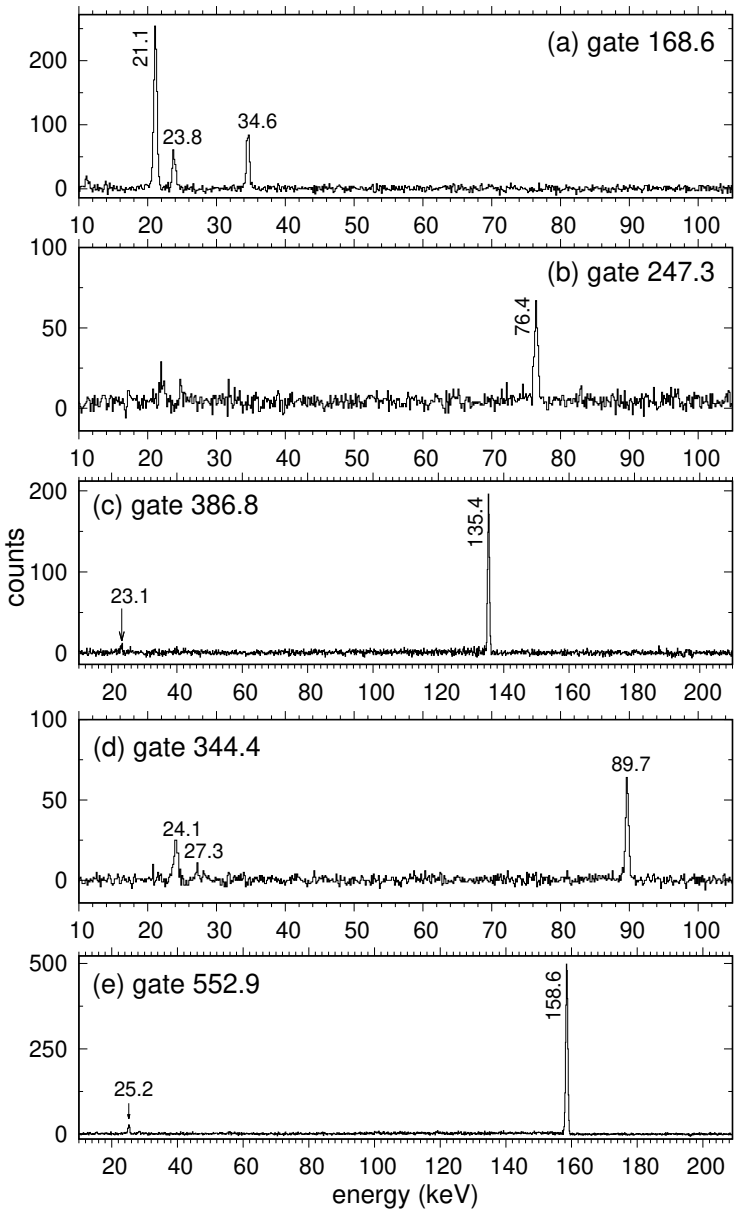

Figure 33: γ-gated coincidence spectra used for experimental estimation of the internal conversion coefficients. Next to each panel label, the energy (in keV) of the gating γ transition is provided.

short $T_{1/2}$ value versus cycle of work for Penning trap (131 ms) it was not possible to register the β feeding from the decay of this second structure to any excited level in ^{117}Ag. So the ^{117}Ag structure is only feed by decay of ground state of ^{117}Pd.

The calculated $\log_{10} ft$ values presented in column 3 of Table 6 were obtained using [92], with the input data consisting of experimental β feedings I_β.

The absence of I_β and $\log_{10} ft$ for the 175.8 keV excited level is due to the fact that the intensities of the γ transitions de-exciting this level are higher than the intensities of the transitions feeding it.

The tentative assignments for the 625.6, 658.2, and 995.0 keV levels are based on the assumption that the most common electromagnetic transitions are $E1$, $M1$, and $E2$, as well as on the systematics shown in Fig. 36d.

The experimental $log_{10} ft$ values indicate allowed or first forbidden β transitions (see

Table 5: For the neutron-rich $A = 117$ isotopes, the experimental internal conversion coefficients (ICC) and the corresponding deduced multipolarities of the γ transitions were determined. Theoretical values of ICC were taken from [60].

E_γ (keV)	α_K^{exp}	α_K^{theo}			Multipolarity	Reference
		$E1$	$M1$	$E2$		
		Transition in ^{117}Pd				
34.6	7.0(9)	2.567	7.061	23.2	$M1$	here
34.5	7.1(9)				$M1$	[100]
		Transition in ^{117}Ag				
76.4	0.82(18)	0.299	0.782	2.66	$M1$	here
76.5	0.57(10)				$M1$	[100]
		Transition in ^{117}Cd				
135.4	0.082(18)	0.0612	0.1723	0.4041	$E1$	here
135.4	0.199				$M1$	[101]
		Transition in ^{117}In				
89.7	1.1(2)	0.2051	0.6011	1.625	$E2+M1$	here
89.7	1.3(3)				$E2+M1$	[108]
		Transition in ^{117}Sn				
158.6	0.056(9)	0.0427	0.135	0.249	$E1$	here
158.6	0.1373(30)				$M1(E2)$	[109]

Table 6: The experimental estimates of β feedings are presented as I_β, and $log_{10}ft$ values of the excited levels in ^{117}Ag populated in the β^- decay of ^{117}Pd. The I_β values are upper limits and the $log_{10}ft$ values are lower limits. The energy levels are reported with uncertainties. Tentative I^Π are the forth and the last column.
^{f} - a spin proposed based on fission data in [71].

$E_{lev}[keV]$	I_β	$log_{10}ft$	I^Π	$E_{lev}[keV]$	I_β	$log_{10}ft$	I^Π
0	-	-	$(1/2^-)$				
28.6(3)	-	-	$(7/2^+)^f$	939.0(4)	3.6(0.9)	6.26	$(1/2,...,5/2)$
175.8(4)	0.0(<0.2)	-	$(9/2^+)^f$	995.0(10)	0.8(0.2)	6.9	$(5/2^-)$
247.3(1)	12.4(3.9)	5.98	$(3/2^-)^f$	1124.2(6)	2.4(0.5)	6.36	$(1/2,...,5/2)$
323.8(1)	3.2(1.9)	6.55	$(5/2^-)^f$	1166.5(7)	1.3(0.3)	6.63	$(1/2,...,5/2)$
625.6(2)	9.9(1.4)	5.94	$(3/2^-)$	2257.7(8)	11.7(1.4)	5.15	$(1/2,...,5/2)$
649.5(2)	10.8(2.1)	5.9	$(3/2^-)$	2322.3(10)	2.7(0.7)	5.74	$(1/2,3/2)$
658.2(3)	10.5(4.0)	5.91	$(7/2^+)^f$	2351.0(4)	11.0(1.3)	5.12	$(1/2,...,5/2)$
769.6(3)	8.1(0.9)	5.98	$(1/2,3/2)$	2394.5(10)	1.5(0.6)	5.98	$(1/2,...,5/2)$
834.5(1)	10.7(1.5)	5.83	$(3/2,5/2)$	2437.2(20)	2.8(0.6)	5.68	$(1/2,3/2)$

Chapter 3.10). It should be noted that these conclusions were drawn under the assumption that the ground state of ^{117}Pd has a spin and parity of $1/2^+$.

The β feedings to the excited levels in ^{117}Ag, as well as the $\log_{10} ft$ values, are shown in Table 6. Usually plenty of γ lines are of too low intensity, to be detected. Therefore our experimental values of the β feeding intensities are the upper limits, so the $\log_{10} ft$

values are the lower limits.

The Alaga rule [110] can be used to determine the relative intensities of β transitions to rotational levels. Considering this is important in the case of ^{117}Ag, as in principle the rule could apply here: the β decay of the $(1/2^+)$ state in ^{117}Pd populates the $(1/2^-)$ state in ^{117}Ag. On this basis, it was assumed that both the 28.6-keV isomeric state and the ground state might receive some additional feeding from β decay. If such feeding is neglected, the extracted $\log_{10} ft$ values appear artificially reduced. However, applying the Alaga rule in this case encounters a fundamental difficulty, since the rule is only valid when K is a good quantum number. This is true for axially symmetric deformed nuclei, but the results presented in this work indicate the coexistence of prolate and triaxial structures in ^{117}Ag. Therefore, K cannot be regarded as a good quantum number in this nucleus, and the application of the Alaga rule is not justified. Nevertheless, even under the assumption of additional feeding, the effect on the derived $\log ft$ values is modest: for 10% and 50% assumed feeding, the average increase in $\log ft$ values was only 0.7% and 5%, respectively. For this reason, the final analysis was performed under the assumption of zero additional feeding to the ground state and the 28.6-keV excited level in ^{117}Ag.

In ^{117}Ag, high-spin levels were not observed because the decaying ground-state $(1/2^+)$ in ^{117}Pd cannot populate them, and the decaying isomer with higher spin has a half-life that is too short to be measured at all.

7.8 Strength distribution in β decay

Gamow-Teller (GT) transitions represent a class of nuclear β decays in which a nucleon converts from neutron to proton or vice versa, causing the nuclear spin to change by one unit ($\Delta J = 1$) without a parity change. These transitions, which are mediated by the weak interaction and involve both spin and isospin degrees of freedom, are well documented in Section 7.2 of [58].

The strength of a GT transition is quantified by the $B(GT)$ value (Gamow-Teller transition probability). The $B(GT)$ distribution describes how this transition strength is spread over different energy levels of the daughter nucleus.

Investigation of the $B(GT)$ distribution provides important insights into the nuclear structure and the arrangement of excited states. Systematic comparison of experimental and theoretical $B(GT)$ values contributes to the improvement and validation of nuclear models [111].

The data from Table 6 were used to calculate the β feedings to the excited levels in ^{117}Ag. The I_γ intensities were corrected (enlarged) to include the internal conversion for the transitions 76.4, 147.2, 247.3, 301.7 and 323.8 keV.

The experimental Gamow-Teller transition strengths $B_i(GT)$ were determined using the comparative half-lives t_i and phase space factors f_i measured for the observed β transitions. Summing the $B_i(GT)$ over all transitions in a decay of the nucleus of interest gave the total $B(GT)$ value. The following formula was applied:

$$\Sigma B(GT) = \sum_i B_i(GT) = \sum_i \frac{3860}{f_i t_i} \tag{7.1}$$

The distributions of $B_i(GT)$ values are presented in Fig. 34 for the β decay of ^{117}Pd to ^{117}Ag.

The excited state with an energy of 2351 keV exhibits the highest β feed, with a value of 0.0301. Significantly lower β feed is observed for the low-lying excited states in the

^{117}Ag nucleus.

The structure of this nucleus exhibits a pattern of numerous low-lying states with small $B(GT)$ values, a gap of excited levels between 1200 and 2200 keV, and several high-energy states with large $B(GT)$ strengths.

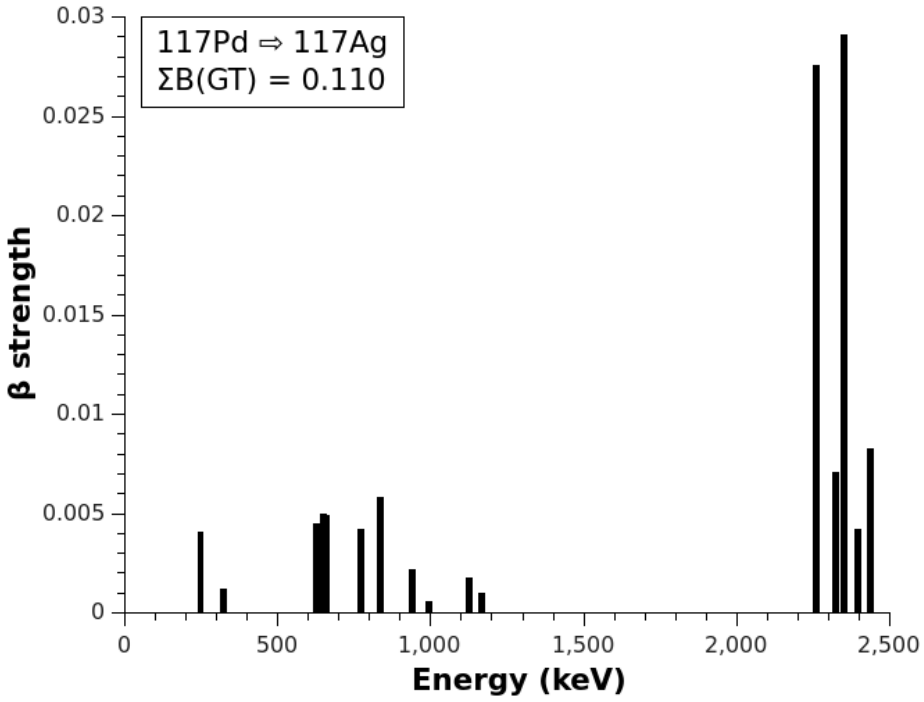

Figure 34: The distributions of *B(GT)* decay strength in the β decay of ^{117}Pd (g.s.) to ^{117}Ag. Total *B(GT)* strength is presented also.

Fig. 34 could be compared to Figure 9 in [112], which shows the same type of graph, but for a lighter silver isotope, ^{115}Ag. There, the β-strength distribution is presented separately for the decays of the ground state and the isomeric state, which is not the case in this nucleus.

For the above β-strength distributions, the following similarities can be observed. In both cases, low-energy peaks ($<$ 1000 keV) are visible, as well as a clear maximum at higher energies (2000–2500 keV). For both ^{115}Ag and ^{117}Ag, the β-strength distribution is not concentrated in a single peak – multiple weak transitions are present, which indicates a complex structure of the daughter nuclei. The total number of levels populated in the β-decay is identical. But the parameter B(GT) is a little larger in the case of ^{117}Ag.

The main differences in the β-strength distributions are as follows. In ^{115}Ag, the peak at around 2100 keV is clearly dominant and significantly stronger than the others. In ^{117}Ag, the peaks are more spread out and grouped around 2400 keV, but the dominant peak is less pronounced than in the lighter silver isotope. The β-feeding from the isomeric state is noticeably weaker than from the ground state.

7.9 Historical overview of ^{117}Ag studies

The β^- decay of ^{117}Pd to ^{117}Ag was first indirectly observed by [113]. In this publication a half-life of $5.0^{+0.5}_{-0.7}$ s was calculated and, no γ rays were detected. In [114], a decay

with a half-life of 5.0(4) s was reported for a 247.1-keV γ transition. It was attributed to the β^- decay of either ^{117}Pd or ^{118}Pd. No direct observation of the decay of ^{117}Pd had been reported before these studies. Moreover, in [97], the 247.5-keV, 323.9-keV, and 402.5-keV γ transitions were assigned to the decay of ^{117}Pd, and a half-life of 4.4(2) s was determined based on these γ transitions.

Based on the data available in the [1] database and relying solely on the production mechanism of ^{117}Ag through the β^- decay of ^{117}Pd, two excited states have been assigned to the former nuclide. These states are characterized by energies of 247.5 keV and 323.9 keV, respectively. Additionally, 12 γ lines have been attributed to the nuclide, but only three of them are integrated into the scheme of excited states: 76.6 keV, 247.5 keV, and 323.9 keV. Each of the two excited states has been confirmed in this study. Regarding the γ lines, Table in [1] includes lines 76.6, 147.3, 247.5, 323.9, 402.5, 482.1, 522.6, 625.9, 630, 649.5, and 769.7 keV, which are being consistent with those in this work. Only the 349 keV line was not confirmed in this study.

Whereas the evaluated data, name as Adopted Levels in [1], differs from β-decay of ^{117}Pd data only with an extra level at 28.6 keV, along with a transition of the same energy, which de-excites to the ground state of ^{117}Ag. This level has been confirmed in the study and is fed by the 147.2 keV and 629.7 keV lines. However, the 28.6 keV transition was not observed. This is due to the fact that the 28.6 keV excited state predominantly de-excites via the production of conversion electrons rather than the emission of gamma quanta. As a result, germanium detectors are unable to register the particles emitted in this process.

The data presented in [1] as ^{117}Ag IT decay provide additional information solely about the 28.6 keV level. According to this evaluation, the 28.6 keV line is classified as an E3 transition with a conversion coefficient $\alpha = 1.15 \cdot 10^4(6)$. However, this study can neither confirm nor refute these findings.

The data in XUNDL, although the most up-to-date, do not introduce anything significant for these considerations.

Recently, a comprehensive overview of the excited states in odd-A silver isotopes $^{111-121}$Ag was published in [115]. The experimental data discussed therein were obtained from the spontaneous fission of ^{252}Cf and analyzed using high-fold γ-ray coincidences measured with the Gammasphere array of Compton-suppressed Ge spectrometers.

7.10 Shape predictions

Theoretical predictions have most often been carried out for palladium rather than for silver, since palladium possesses an even number of protons in its nucleus. Therefore, in this section, publications concerning theoretical calculations of the deformation parameter for Pd are cited [15, 116, 117, 118], so that conclusions may be drawn in the context of the studied nucleus ^{117}Ag.

The theoretical calculations presented in [117] covered even-even nuclei, including palladium isotopes in the range of ^{88}Pd to ^{132}Pd, thus encompassing the mass region around $A \simeq 110$. The study employed the relativistic mean-field (RMF) framework with NL3 and NL3* parameter sets, which are particularly effective for describing both ground and excited states, accounting for collective properties in spherical as well as deformed nuclei.

The calculations based on NL3 presented there suggest the quadrupole deformation parameter β_2 for ^{110}Pd is equaled to 0.240 for the ground state, which lies in a good agreement with experimental value 0.257, so strong prolate deformation is expected. The

publication did not specify whether the experimentally determined deformation parameter refers to the ground state or to an isomer, but the former was assumed, since it is experimentally easier to measure. Next, heavier nucleus ^{112}Pd the calculations predicted two minimum points in the potential, one for β_2 = -0.231 for the ground state and value for first intrinsic excited state 0.220, so two drastically different deformations, whereas the experiment predicted the prolate deformation, with 0.220 value. The same situation happens in case of next checked nucleus ^{114}Pd, within calculated values -0.231 and 0.292 for the ground state and first excited state, respectively. And experimental β_2 = 0.164, which once again suggest the lack of agreement between NL3 calculation and experimental data. Deformation in next nucleus ^{116}Pd could be described the same way with calculated values -0.221 and 0.216, and experimental value 0.207. For ^{118}Pd a switch in the calculation is noticeably, with only one minimum for -0.198 for the ground state, which shows a drastic change in case of NL3 shape predictions for ground states of pallad isotopes. The oblate deformation trend lasts till ^{120}Pd and than once again calculations suggest only prolate deformation in range of ^{122}Pd to ^{132}Pd [117].

In summary, the theoretical predictions in [117] are not consistent with the experimental data. For Pd isotopes, the ground states are predicted to exhibit prolate deformation, while the isomeric states are predicted to be oblate.

Further theoretical predictions appeared in the work [15] in the range ^{114}Pd - ^{128}Pd. For ^{114}Pd, two minima were identified: one on the oblate deformation side and the other on the prolate side. The calculated parameters indicated significant deformations of both types, with values of approximately 0.2 for the ground state and about -0.22 for the isomeric state. This publication also presented results for odd-mass nuclei. Estimates for nuclei in the range ^{115}Pd to ^{117}Pd suggest the presence of two minima. Specifically, the β_2 values are approximately 0.19 and -0.23 (^{115}Pd), 0.18 and -0.22 (^{116}Pd), and 0.15 and -0.11 (^{117}Pd), where in each case the first value corresponds to the ground state and the second to the isomer. From ^{118}Pd to ^{128}Pd, only one minimum appears, oscillating near $\beta_2 = 0$ on the prolate deformation side. The model indicates that in lighter Pd isotopes, configurations with negative quadrupole deformation (oblate) are predominant, whereas with increasing neutron number, the Pd nuclei evolve toward more spherical shapes [15]. Experimental data presented in Figure 7 of [15] indicate an assignment of $(1/2^+)$ for the ground state of ^{115}Pd and $(7/2^-)$ for the corresponding isomeric state. More relevant to the present study is the neighbouring nucleus, for which experimental values of $(3/2^+)$ and $(7/2^-)$ have been assigned, with the order of level attribution consistent with the previous isotope. The applied model, based on deformed QRPA calculations, predicts a ground-state spin of $5/2^-$ for ^{115}Pd, which does not agree with the experimental assignment, and $7/2^-$ for the isomeric state, which is also inconsistent with the aforementioned data. For ^{117}Pd, the experimental assignments are $(1/2^+)$ for the ground state and $(9/2^-)$ for the isomer, which in this case are in agreement with the model predictions. Another nucleus of interest in this work, ^{119}Pd, has been experimentally assigned a ground-state spin of $(3/2^-)$.

In the region of ^{114}Pd to ^{117}Pd, the predictions for the deformation parameter from two different sources [15, 117] indicate contrasting and opposing types of deformation. For ^{122}Pd – ^{128}Pd, the results are consistent and indicate a single minimum with a slight prolate deformation.

The publication [118] presented a wide range of analyzed isomers using the finite-range droplet macroscopic and folded-Yukawa single-particle microscopic nuclear-structure models, as well as HFB CEA PES. For the purpose of this work, only a subset of data within

the range ^{110}Pd to ^{132}Pd is cited. For the lightest nucleus in this set, a strong prolate deformation was predicted with a deformation parameter $\beta_2 = 0.24$. According to this study, the subsequent ground states in nuclei ^{110}Pd, ^{112}Pd, and ^{114}Pd to ^{119}Pd are characterized by a strong oblate deformation, with β_2 values ranging from -0.206 for ^{119}Pd to a maximum negative value of -0.258 for ^{117}Pd. Over the range ^{120}Pd to ^{123}Pd, the parameter remained negative, gradually approaching zero.

The predictions presented in [118] are consistent with those in [117], but they concern only ground states, so no comparison was made for isomeric states.

The publication [118], cited in this chapter as the only one, also referred to silver nuclei. There, the ground states of the lightest nuclei ^{110}Ag and ^{111}Ag were described as strongly prolate deformed states, while the others up to ^{120}Ag were characterized by strong oblate deformation.

The next publication on a similar topic written by Möller [116] described only even-mass nuclei and was based on calculated potential-energy surfaces for Pd. The theoretical calculation for nuclei with even mass number is definitely easier, however, it is the nuclei with odd mass number that are characterized by a richer structure.

It predicted for ^{110}Pd a spheroidal deformation parameter $\eta_2 = 0.25$ with an axial asymmetry γ of 30 degrees, where $\gamma = 0°$ corresponds to prolate and $\gamma = 60°$ to oblate shapes. For ^{112}Pd, the predictions were $\eta_2 = 0.27$ at 25° and $\eta_2 = 0.25$ at 55°. The subsequent even-mass nuclei were predicted as follows: for ^{114}Pd, $\epsilon_2 = 0.22$ at 0°, $\eta_2 = 0.25$ at 18° (axially asymmetric saddle), and $\eta_2 = 0.25$ at 60°.

For ^{116}Pd, three energy minima were predicted at $\epsilon_2 = 0.22$, corresponding to orientations at 0°, 22°, and 60°, so one minima for the oblate deformation and one for the prolate deformation.

In the case of ^{118}Pd and ^{120}Pd, only a single minimum was obtained for each, with deformation parameters $\epsilon_2 = 0.20$ and 0.22, at orientation angles of 48° and 38°, respectively. Which suggests the presence of triaxial deformation.

For the subsequent nuclei, the predicted minima are located near $\epsilon_2 \approx 0$ and orientation angle 0°. The publication includes only theoretical calculations for even-Z nuclei; therefore, analogous figures for silver isotopes are unfortunately not provided.

7.11 Comparison of ^{117}Ag with neighbouring nuclei

Two systematics for the nucleus ^{117}Ag and nearby silver isotopes have been prepared and are presented in this section.

Figure 35 shows systematics of low-energy levels for silver isotopes, and is comparable to Figure 5 in [119]. While the cited work covers a broader range of isotopes (N = 48–84), Fig. 35 focuses on a narrower subset. Nevertheless, both systematics exhibit consistent trends in several respects. In particular, the $1/2^-$ state serves as the ground state for isotopes with N = 58–70 (Figure 5) and N = 60–70 (Fig. 35). For ^{119}Ag, both systematics predict a $7/2^+$ first excited state, which is not consistent with experimental assignments. The reassignment of the ground-state spin, proposed in this work and in [70], aligns with the trend observed in lighter silver isotopes: $1/2^-$ for the ground state and $7/2^+$ for the first excited state.

The systematics are consistent for the first and second excited states in the range N = 60–70. Another common trend is observed for the $11/2^+$ level, which maintains an almost constant energy across successive isotopes. This level was therefore chosen as a reference point in Fig. 35. In ^{119}Ag, the corresponding energy is 670.6 keV, whereas in

^{117}Ag it was not experimentally identified.

Figure 35 also shows levels that do not appear in Figure 5 of [119]. One example is the $1/2^+$ level, which emerges from ^{111}Ag, but has no evidence in ^{119}Ag [1]. This level deviates from the trend of the previously described states ($1/2^-$ ground state, first $7/2^+$, second $9/2^+$). The $1/2^+$ energy exhibits a parabolic trend, similar to the $3/2^+$ and $7/2^+$ levels, while the $5/2^+$ level reaches a minimum at ^{113}Ag and shows comparable energies for ^{117}Ag and ^{119}Ag.

The systematic behavior of negative-parity states is also presented, starting from ^{111}Ag to ^{119}Ag. Most nuclei exhibit states with spins ranging from 3/2 to 9/2, which generally decrease in energy with increasing neutron number. This trend is observed for the $3/2^-[301]$, $5/2^-[301]$, $7/2^-[301]$, and $9/2^-[301]$ states, while the $5/2^-[303]$ and $3/2^-_1[301]$ levels slightly increase in energy along the isotopic chain. Certain levels are absent in specific nuclei: $9/2^-[301]$ in ^{113}Ag and ^{115}Ag, and $5/2^-[301]$ and $7/2^-[301]$ in ^{117}Ag. For example, an excited level of 834.5(1) keV in ^{117}Ag can be tentatively assigned as $5/2^-[301]$, consistent with the systematics.

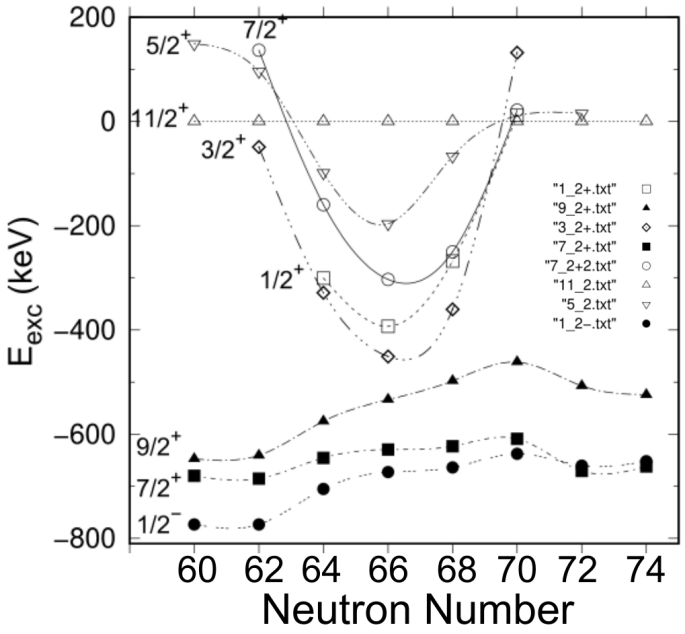

Figure 35: Systematics of positive- and negative-parity excited states in silver isotopes in the mass region $A \approx 110$.

Another systematic, based on γ transitions, spans ^{111}Ag to ^{119}Ag and reveals a consistent structure of three bands in nearly every nucleus (Fig. 36). These bands represent the occupancy of specific single-nucleon states characterized by spins $1/2^-[301]$, $3/2^-[301]$, or $5/2^-[303]$. Minor exceptions include the absence of the $3/2^-[301]$ band in ^{113}Ag and the $5/2^-[303]$ band in ^{117}Ag.

Establishing these systematics is valuable for assigning spins and parities to excited states in specific nuclei. Observing trends across isotopes allows for more confident assignments than focusing on a single nucleus alone. For instance, the 995.0 keV level in ^{117}Ag was assigned as $5/2^-$, although previously a broader range of $(1/2, \ldots, 5/2)$ had been discussed.

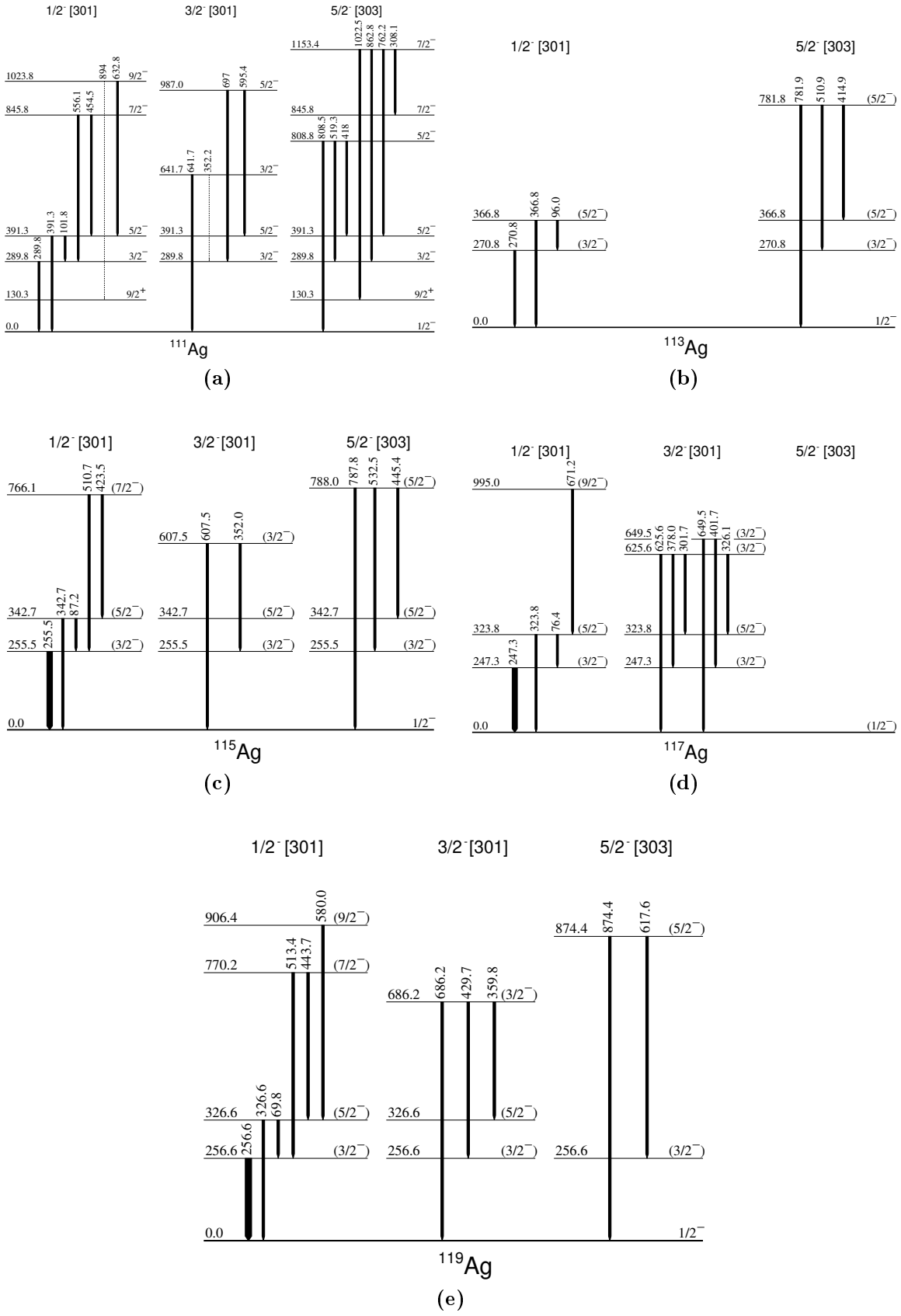

Figure 36: Systematics of low-energy levels in odd-A silver isotopes from ^{111}Ag to ^{119}Ag, showing three bands that appear either entirely or predominantly in all nuclei. Data for ^{111}Ag–^{115}Ag are from ENSDF [1], for ^{117}Ag from [71], and for ^{119}Ag from [70].

Chapter 8. β^- decay of $^{119}_{46}$Pd to $^{119}_{47}$Ag

8.1 Analysis of singles and coincidence spectra

The singles spectrum of γ rays emitted after the β^- decay of ^{119}Pd to ^{119}Ag has been already presented in Fig. 22(a). Another example is shown in Fig. 37(a). Additionally Fig. 37(b) shows the example of a β-gated spectrum.

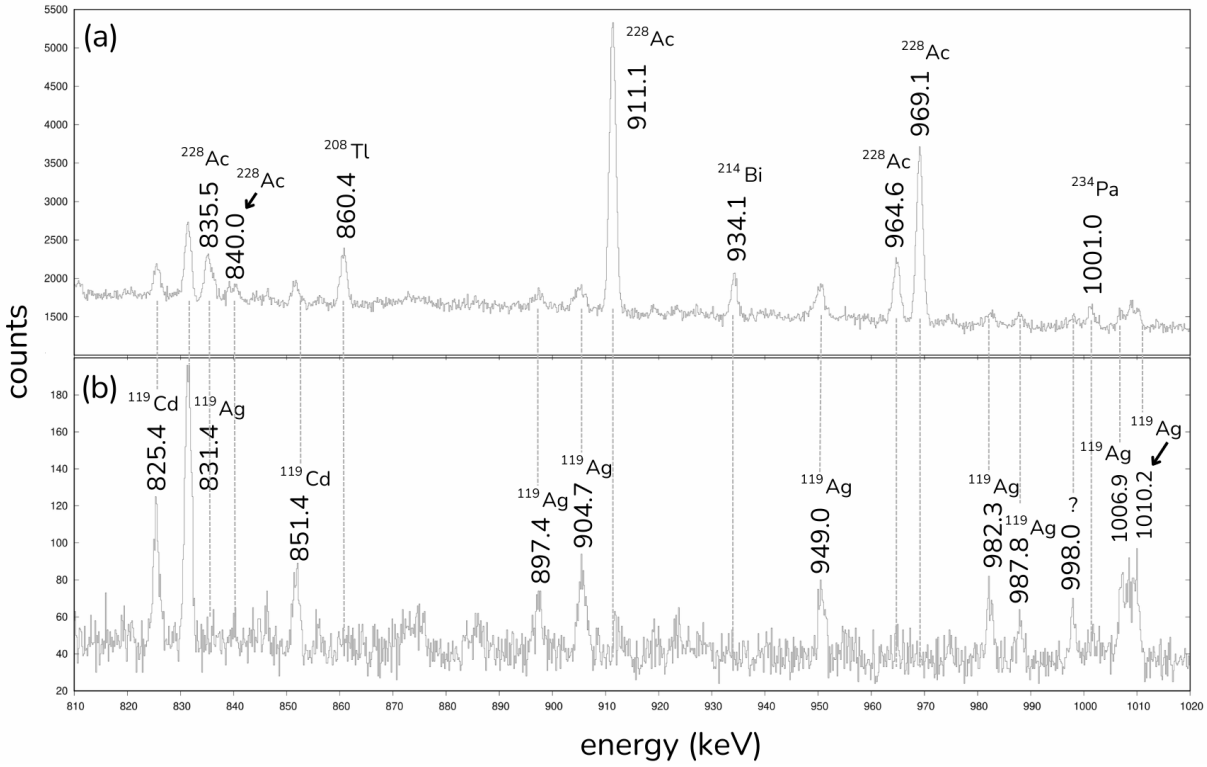

Figure 37: (a) The singles and (b) β-gated spectra recorded using LEGe detectors for the monoisotopic samples of ^{119}Pd. Each peak is annotated with its energy in keV and assigned nuclei. In panel (a) the γ lines ascribed to heavy nuclei (Tl, Bi, Ac and Pa) originate from natural γ background radiation. Panel (b) shows only the peaks corresponding to isobars with $A = 117$.

Fig. 37 shows the energy range from 810 to 1020 keV. In Fig. 37(a), peaks marked as ^{208}Tl, ^{214}Bi, ^{228}Ac, and ^{234}Pa belong to natural background γ radiation, see [78, 79]. This energy range was chosen to clearly demonstrate the strength of gating on β events.

In Fig. 37, additional lines connecting panel (a) and panel (b) are drawn to emphasize the disappearance of background-derived γ peaks, when a gating condition for β particles is applied during data analysis stage. Indeed, after applying such a condition in Fig. 37(b), the peaks originating from the natural background radiation, visible in Fig. 37(a) are no

longer visible, while other γ lines have become more pronounced. In the spectrum of Fig. 37(b), only peaks assigned to ^{119}Ag excited levels scheme are observed. All γ lines in ^{119}Ag, populated in the β^- decay of ^{119}Pd, are presented in Tables 7, 8.

In this energy range, only the line at 998.0 keV has not been attributed to this nuclide, and no other nucleus in this work, has been identified as its possible source.

In Fig. 37, only the line at 998.0 keV has not been attributed to any nuclide, which often happens for γ lines of low intensity.

Singles spectra and β-gated spectra within full energy range were analysed by use of methods described already in Chapter 5.1 - Chapter 5.4, finding the energies of the individual peaks and assigning a nuclide to them. After analysis of the singles and β gated singles spectra, the γ γ coincidences were analysed (Chapter 5.4).

An example of a γ spectrum, which was made by setting gates on two-dimensional $\gamma\gamma$ histograms, is shown in Fig. 38. In Fig. 38(a) and Fig. 38(b), the gates were set on γ lines belonging to Band B. In the nucleus ^{119}Ag, there are two structures of excited states, labeled as Band A and Band B (shown as Fig. 40). Band B will be describe in greater detail in Chapter 8.3. Applying a gate on the strongest γ line 129.8 keV, resulted in a spectrum showing that, the lines at 182.4, 507.4, 536.6, 550.7, and 607.3 keV are in coincidence with the gated line (Fig. 38(a)). The coincidence technique has already been described in chapter 5.4. In Fig. 38(b), the gate was set to the 507.4 keV line, revealing that the following lines are in coincidence with this line: 22.1, 129.8, 182.4, and 536.6 keV. Since the 507.4 keV γ line was observed in panel (a) and the 129.8 keV γ line in panel (b), these two lines are undoubtedly in coincidence and, in the excited state scheme (Fig. 40), are the part of the cascades, as well as 182.4 and 536.6 keV lines, which were already visible in the spectrum Fig. 38(a) and Fig. 38(b). The observed 22.1 keV line confirms that the 507.4 keV γ line can be attributed to the ^{119}Ag nucleus, although this line is not shown in the excited state scheme Fig. 40, because it is a characteristic X ray line of silver. This topic has already been brought up in Chapter 5.3. All coincidence γ lines for all set gates are listed in Tables 7, 8.

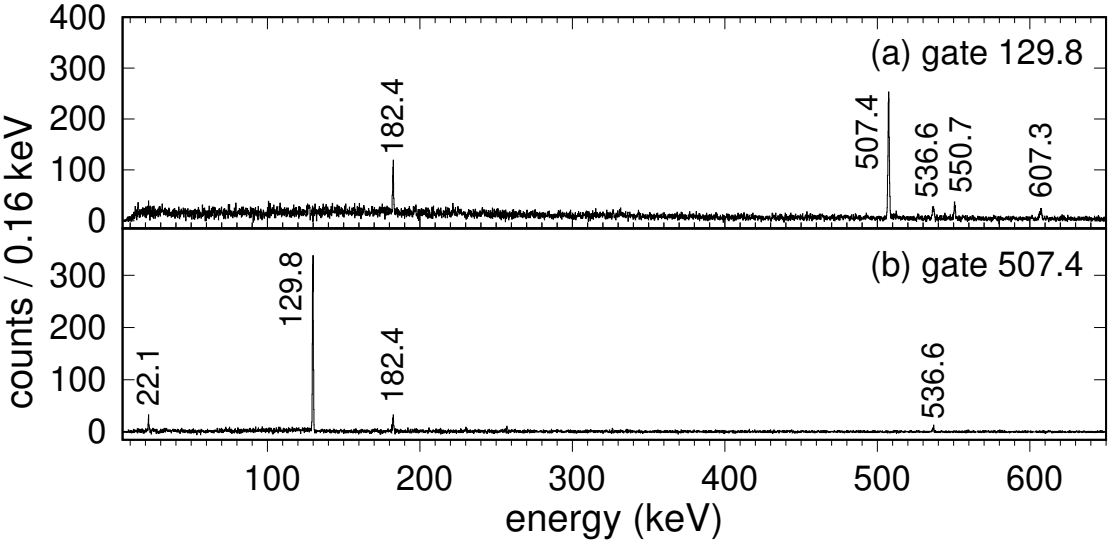

Figure 38: The coincidence γ spectra for the monoisotopic ^{119}Pd samples. Spectrum in panel (a) is gated by the 129.8-keV γ line and in panel (b) by the 507.4-keV γ line. Both lines are associated with Band B in the excited levels scheme in ^{119}Ag. The peaks are annotated with their energies in keV.

The corresponding example of the γ-gated spectra for Band A is on Fig. 39. In Fig. 39(a) the gate was set to the energy 580.0 keV and the following γ lines are in coincidence: 22.1, 69.8, 256.6, 326.5, 534.0, 547.9 and 672.6 keV. The presence of 22.1 keV X-ray line in any of the spectra in Fig. 39 is an additional confirmation that one can assign the gated γ lines to the studied nuclide. For Fig. 39(b), the gate was set to the γ energy of 256.6 keV, and the peaks that belong to the same cascade as this line, are as follows: 22.1, 69.8, 429.7, 443.7, 513.4, 547.9, 580.0, and 617.8 keV. All these γ lines occur in the Band A branch of the ^{119}Ag nucleus. Several lines that were previously visible reappear, such as: 22.1-, 69.8-, 256.6- and 547.9-keV lines, which further confirm the coincidence of these lines. All coincidence γ lines for all set gates are listed in Table 7. The presence of the 580.0 keV line in Fig. 39(b) confirms the mutual coincidence between this γ line and the 256.6 keV line.

And finally, in Fig. 39(c), the γ-gated spectrum where the coincident peaks are less pronounced, as compared to the gate at 129.7 keV (Fig. 38(a)). Here the gate was set on the 136.2-keV line and 22.1, 256.6, 326.5 and 443.7 keV showed as the γ lines in coincidence.

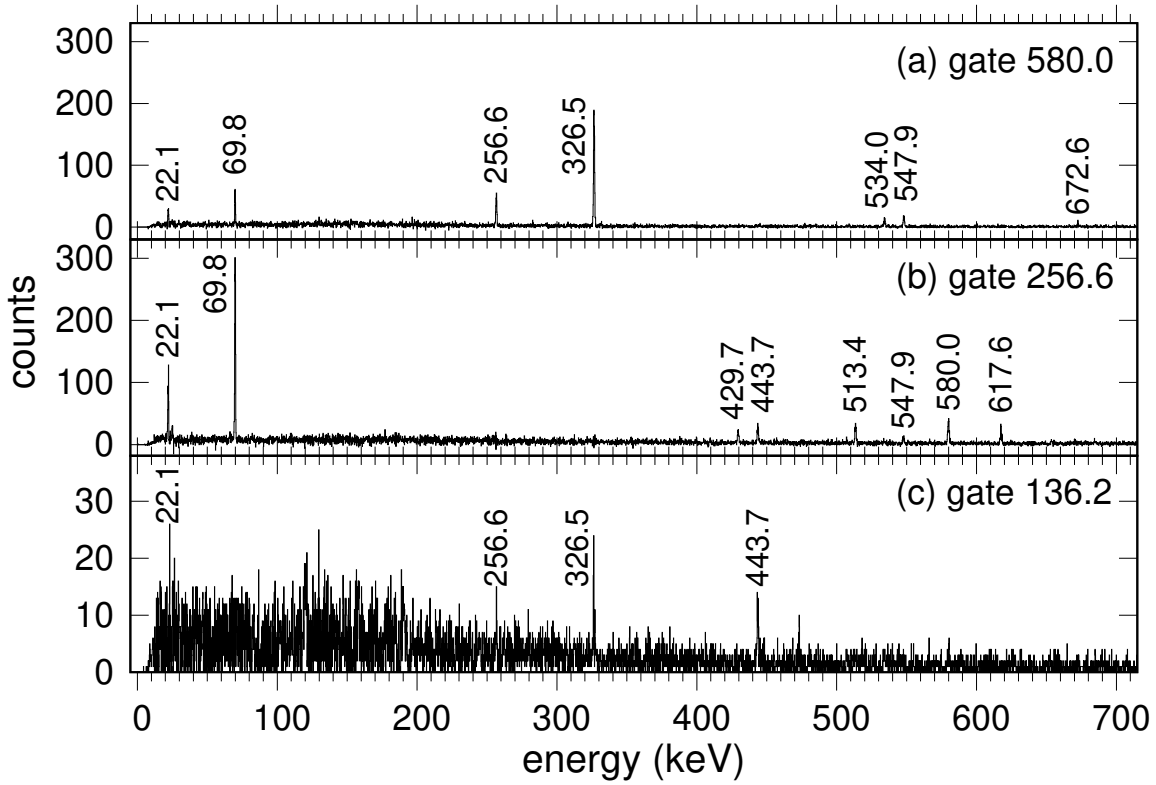

Figure 39: The coincidence γ spectra for the monoisotopic ^{119}Pd samples. Spectra in panels (a) and (b) are gated by the 580.0-keV and 256.6-keV lines, respectively, both the lines associated with Band A. Spectrum in panel (c) is gated by the 136.2-keV line. The peaks are annotated with their energies in keV.

8.2 Calculation of γ line intensity in ^{119}Ag

The intensity of a γ line is determined by estimating the area under the peak in the singles spectrum. For some weak lines, the intensities were taken from a β-gated spectrum or estimated using coincidence γ spectra. In cases where γ lines were doubly placed

or belonged to multiple isotopes, the intensities were distributed based on coincidence relations. The intensity estimation accounts for the efficiency calibration of the detectors too, and the intensity is obtained by dividing the peak area by the efficiency value. The issue of determining intensities has already been discussed earlier in Chapter 6.2 and 7.3.

8.3 Coincidence relations and construction of the excited-level scheme

In the nucleus ^{119}Ag, the analysis revealed two excited-state structures, labeled as Band A and Band B (see Fig. 40). These bands consist of nearly independent excited levels and transitions that depopulate their energy to the ground state (in the case of Band A) or to a low-energy, isomeric state at 33.4 keV (in the case of Band B). Most of the levels can be assigned to one of these structures, which are based on the $1/2^-$ and $7/2^+$ isomers, respectively. Although there are some excited levels connecting the two structures. These levels include: 770.2, 906.4, 1579.0, and 1803.7 keV, which are visible in the center of Fig. 40. The first two of these levels were assigned to Band A, since the intensities of the transitions depopulating these states support their placement in Band A.

There is only one γ line, of 136.2 keV energy, that cannot be clearly assigned to either Band A or Band B. This γ line is included in Table 7, together with the lines that have been classified as belonging to Band A.

A total of 33 new excited states and 57 new γ lines were observed in ^{119}Ag in the current β-decay measurement. Several transitions populating the ground state of ^{119}Ag, with no observed coincidence relations, were included in the scheme if their energy matched the difference between the ground state and the energy of an initial level determined from at least one coincidence relation.

Tables 7, 8 present all coincidences revealed during the analysis of the monoisotopic ^{119}Pd samples, separately for Bands A and B.

In Fig. 40, the constructed scheme of excited states in the nucleus ^{119}Ag is presented, based on the coincidences recorded in Tables 7, 8. On the right-hand side of the scheme, as part of Band B, several levels are depicted, starting from 2113.6-keV and ending at 2818.1-keV, which are disproportionately close to the lower-lying excited states. The reason for this representation is purely pragmatic to decrease the size of the figure. Additionally, in Fig. 40, five transitions in band A are depicted as very weak transitions (relative intensities below 1.5) and are therefore represented with dashed lines instead of solid ones. In contrast, Band B is characterized by only one such weak transition.

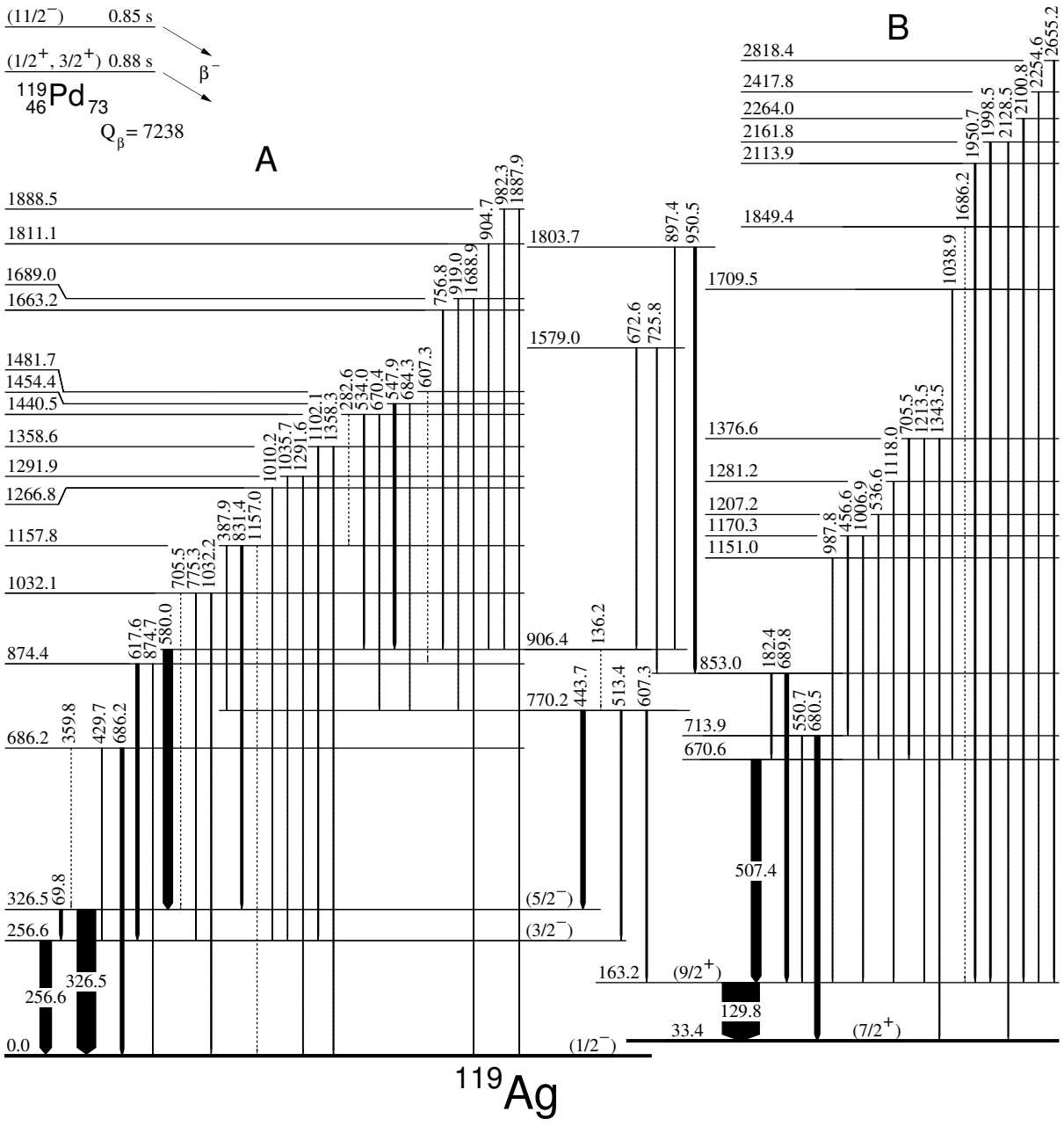

Figure 40: The level scheme of ^{119}Ag populated through the β^- decay of ^{119}Pd. The half-life values and the Q_β value (in keV) are taken from [120]. The arrow widths are approximately proportional to the γ intensities, and all energy values are given in keV. Two band structures are indicated with capital letters A and B.

Table 7: For Band A, the energies, relative intensities I_γ, their placement in the excited scheme, and coincidence relationships observed in the β^- decay of ^{119}Pd to ^{119}Ag are presented here. The energy 22.1 keV corresponds to the K_α characteristic X-rays of silver. [1] Line appears at two places, [2] intensity observed in coincidence with β particles, [3] a transition also observed in the β decay of ^{119}In. Energies of weak transitions are in parentheses.

BAND A				
E_γ(keV)	I_γ	From	To	Coincident γ lines
22.1(1)				129.8, 256.6, 326.5, 443.7, 507.4, 547.9, 580.0, 689.8, 831.4
69.8(2)	7.3(4)	326.5	256.6	22.1, 256.6, 443.7, (534.0), (547.9), 580.0, (684.3)
136.2(2)	0.9(2)	906.4	770.2	256.6, 326.5, 443.7, (580.0)
256.6(2)	62.0(3.1)	256.6	0.0	22.1, 69.8, 429.7, 443.7, 513.4, 580.0, 617.6, (684.3), (756.8), 775.3, 831.4, (897.4), 904.7, (919.0), (982.3)
282.6(2)	1.1 (0.2)	1440.5	1157.8	(69.8), (256.6), (831.4)
326.5(1)	99.1 (5.0)	326.5	0.0	(136.2), 282.6, (359.8), (387.9), 443.7, 534.0, 547.9, 580.0, 672.6, 684.3, 705.5, 756.8, 831.4, (897.4), 904.7, (919.0), (982.3)
359.8(2)	1.2 (0.2)	686.2	326.5	326.5
387.9(2)	2.3 (0.2)	1157.8	770.2	256.6, 326.5, 443.7
429.7(2)	2.4 (0.2)	686.2	256.6	256.6
443.7(1)	24.5 (1.2)	770.2	326.5	22.1, 69.8, (136.2), 256.6, 326.5, 387.9, 670.4, 684.3, (919.0)
513.4(2)	8.4 (0.7)	770.2	256.6	256.6
534.0(2)	4.5 (0.3)	1440.5	906.4	69.8, 256.6, 326.5, 580.0
547.9(1)	13.2 (0.7)	1454.4	906.4	22.1, 69.8, 256.6, 326.5, 580.0
580.0(1)	48.8 (2.5)	906.4	326.5	22.1, 69.8, 256.6, 326.5, 534.0, 547.9, 672.6, 756.8, (897.4), 904.7, (982.3)
607.3(2)[1]	1.0 (0.5)	1481.7	874.4	(256.6), (326.5), (617.6)
617.6(2)[2]	9.1 (0.6)	874.4	256.6	256.6, (607.3)
670.4(2)	3.5 (0.3)	1440.5	770.2	(69.8), 256.6, 326.5, 443.7
672.6(2)	4.0 (0.3)	1579.0	906.4	(256.6), 326.5, 580.0
684.3(2)	2.9 (0.3)	1454.4	770.2	(22.1), 69.8, 256.6, 326.5, 443.7
686.2(1)	8.9 (0.5)	686.2	0.0	
705.5(3)[1]	1.1 (0.4)	1032.1	326.5	(69.8), 256.6, 326.5
756.8(2)	5.7 (0.4)	1663.2	906.4	69.8, 256.6, 326.5, 580.0
775.3(2)	2.1 (0.3)	1032.1	256.6	256.6, 326.5
831.4(2)	13.1 (0.7)	1157.8	326.5	(22.1), 69.8, 256.6, 282.6, 326.5
874.7(3)	1.9 (0.4)	874.4	0.0	
897.4(2)	3.2 (0.3)	1803.7	906.4	256.6, 326.5, 580.0
904.7(2)	3.1 (0.5)	1811.1	906.4	326.5, (580.0)
919.0(3)	1.9 (0.3)	1689.0	770.2	(256.6), (326.5), (443.7)
982.3(2)	2.9 (0.3)	1888.5	906.4	256.6, 326.5, 580.0
1010.2(2)	3.1 (0.4)	1266.8	256.6	256.6
1032.2(2)	4.3 (0.4)	1032.1	0.0	
1035.7(3)	1.6 (0.3)	1291.9	256.6	256.6
1102.1(2)[3]	4.2 (0.5)	1358.6	256.6	256.6
1157.0(4)	1.3 (0.4)	1157.8	0.0	
1291.6(3)	2.1 (0.3)	1291.9	0.0	
1358.3(4)	1.7 (0.4)	1358.6	0.0	
1688.9(4)	1.9 (0.5)	1689.0	0.0	
1887.9(4)	1.7 (0.3)	1888.5	0.0	

Table 8: For Band B, the energies, relative intensities I_γ, their placement in the excited scheme, and coincidence relationships observed in the β^- decay of ^{119}Pd to ^{119}Ag are presented here. The energy 22.1 keV corresponds to the K_α characteristic X-rays of silver. [1] Line appears at two places, [2] intensity observed in coincidence with β particles, [3] a transition also observed in the β decay of ^{119}In. Energies of weak transitions are indicated in parentheses.

BAND B				
129.8(1)	100.0 (5.1)	163.2	33.4	182.4, 507.4, 536.6, 550.7, 607.3, 689.8, 705.5, 725.8, 950.5, 987.8, 1006.9, 1038.9, (1118.0), 1213.5, (1686.2), 1950.7, 1988.5, 2100.8, (2254.6), (2655.2)
182.4(2)	2.9 (0.2)	853.0	670.6	129.8, 507.4, 725.8, 950.5
456.6(2)	1.6 (0.2)	1170.3	713.9	680.5
507.4(1)	26.3 (1.4)	670.6	163.2	22.1, 129.8, 182.4, 536.6, (705.5), (725.8), 1038.9
536.6(2)	2.1 (0.3)	1207.2	670.6	129.8, 507.4
550.7(2)	2.4 (0.3)	713.9	163.2	129.8
607.3(2)[1]	3.5 (0.5)	770.2	163.2	129.8
680.5(1)	14.1 (0.8)	713.9	33.4	456.6
689.8(1)	9.8 (0.6)	853.0	163.2	22.1, 129.8, 725.8, 950.5
705.5(2)[1]	2.0 (0.3)	1376.6	670.6	129.8, 507.4
725.8(2)	2.4 (0.3)	1579.0	853.0	129.8, 182.4, (507.4), 689.8
950.5(2)	6.8 (0.5)	1803.7	853.0	129.8, 182.4, (507.4), 689.8
987.8(2)	2.8 (0.3)	1151.0	163.2	129.8
1006.9(2)	3.6 (0.3)	1170.3	163.2	129.8
1038.9(3)	1.5 (0.4)	1709.5	670.6	129.8, 507.4
1118.0(5)	1.9 (0.4)	1281.2	163.2	129.8
1213.5(2)	5.1 (0.6)	1376.6	163.2	129.8
1343.5(3)	2.2 (0.4)	1376.6	33.4	
1686.2(5)	1.2 (0.4)	1849.4	163.2	129.8
1950.7(4)	3.3 (0.3)	2113.9	163.2	129.8
1998.5(5)	1.9 (0.3)	2161.8	163.2	129.8
2100.8(5)	4.1 (0.4)	2264.0	163.2	129.8
2128.5(5)	1.9 (0.3)	2161.8	33.4	
2254.6(7)	3.3 (0.5)	2417.8	163.2	129.8
2655.2(1.0)	3.3 (0.3)	2818.4	163.2	129.8

8.4 Spin and parity assignments

In total 63 γ lines were assigned to ^{119}Ag nucleus, and 62 γ lines were placed into the excited scheme on Fig. 40. A line of 22.1(1) keV was the only exception, because this line was present in the $\gamma\,\gamma$ spectrum, but it is an atomic-level transition. The excited scheme in Fig. 40 shows 18 excited levels in Band A and 17 excited levels in Band B. Finally 2 excited levels, the 1579.0 and 1803.7 keV, were not unambiguously ascribed to any of the bands. In Fig. 40 they are displayed between the Bands A and B.

The excited states forming Band A, are fed in a β^- decay of the $(1/2^+)$ ground state of ^{119}Pd. In contrast, the states of Band B are populated in a β^- decay of the $(7/2)^-$ isomeric state in ^{119}Pd.

In the study [100], four excited states and five γ transitions (69.9, 129.9, 256.6, 326.1, and 507.2 keV) were identified. This work confirms the spin and parity assignments proposed in [100], where the spin-parity $3/2^-$ was assigned to the level at $257+X$ (denoted in this work as 256.6 keV). Additionally, the $5/2^-$ assignment was attributed to the level at $326+X$ (here known as 326.6 keV). The proposed $(9/2^+)$ spin-parity for the 130-keV level was further substantiated and is presented in this work as a more confident assignment, now recorded without parentheses, corresponding to a level at 162.9 keV. All the lines and levels observed in [1] have been confirmed, and the 507.2 keV transition has also been incorporated into the excited states scheme. It is now listed as the 507.4 keV transition between the 670.3 keV level with spin $11/2^+$ and the 162.9 keV level with spin $9/2^+$.

A reassignment, however, has been made for the ground state and an isomeric level. According to [100], the ground state was characterized by a spin-parity of $(7/2^+)$ for ^{119}Ag. This assignment derived from the systematics of lighter odd-mass silver nuclei, and the assignment for the ground state was extended to studied nucleus.

The whole systematic for odd-mass silver nuclei around mass $A = 100$ was presented as Figure 16 in [70]. There ^{119}Ag exhibits consistent spin-parity assignments $(1/2^-)$ as lighter silver isotopes.

The analysis conducted in this study suggests an alternative assignment: the ground state is now assigned as $1/2^-$, while the isomer is assigned as $7/2^+$, which is precisely the reverse of the assignments in [100] and the established systematics.

The change in spin assignments was inferred from the placement of four excited levels, specifically 770.2, 906.4, 1579.0, and 1803.7 keV, which are part of both bands. By fitting the energies of these levels together with the observed γ transitions and considering only the specific excited levels below, followed by the coincidence relations, a scheme of excited states was obtained, as shown in Fig. 40, where the hypothesis of the $(1/2^-)$ ground state and $(7/2^+)$ isomer spin-parities fits better.

For 256.6- and 326.5-keV levels spins $(3/2^-)$ and $(5/2^-)$, respectively, were proposed based on previously conducted systematic studies (Figure 16 in [70]). These levels are a part of the collective band based on the $1/2^-[301]$ excitation (see Fig. 36e). This structure is an example of a weakly deformed, decoupled band with the unfavored branch shifted up in energy. The same way level 163.2 keV got its assignment as $(9/2^+)$, even if it was assigned to a different band. It perfectly fits the systematic trends in odd-mass silver nuclei (Figure 16 in [70]).

Likewise, spin and parity assignments were made for the excited levels as follows: 770.2 keV was assigned as $7/2^-$, 906.4 keV was assigned as $9/2^-$. These levels are also a part of the collective band $1/2^-[301]$. In ^{117}Ag an analogous level of 995.0 keV was observed (Fig. 36e).

For the excited levels in Band A a bunch of levels was ascribed spin-parities from

β decay data. Spin-parity assignments for the 686.2-, 874.4-, 1032.1-, 1157.8-, 1266.8-, 1291.9-, 1358.6-, 1440.5-, 1454.4-, 1481.7-, 1663.2-, 1689.0-, 1811.1-, and 1888.5-keV levels were proposed based on the assumption that the most common electromagnetic transitions are $E1$, $M1$, and $E2$. All of these levels are included in Band A in Fig. 40. Tentative I^{Π} values are presented in Table 9. For the 1579.0 and 1803.7 keV levels not belonging to bands A or B, the same spin-parity assignment method was used.

The same method was used to make the assignment for levels in Band B. So, 1151.0-, 1170.3-, 1281.2-, 1376.6-, 1709.5-, 1849.4-, 2113.9-, 2161.8-, 2264.0-, 2417.8-, 2818.4-keV received the assignments, which are presented in Table 8.

Based on the data from spontaneous fission measurement described in [70] the level 853.0 keV got assignment $(13/2^+)$. This assignment agrees with the one in [121]. Spin-parity assignment for 670.6-keV level suggest spin 11/2 [70]. Finally assignment for 1207.2-keV level was done based on the systematics (Figure 17 in [70]).

All excited levels in Band A are characterized by negative parity.

8.5 Estimation of β feeding to excited levels

According to the β-decay selection rules, transitions from the $(1/2^+, 3/2^+)$ [70] ground state of ^{119}Pd to the 33.4-keV $(7/2^+)$ level are categorized as second forbidden, rendering β-feeding to the 33.4-keV level effectively negligible. Similarly, the transition from the $(11/2^-)$ isomer in ^{119}Pd to the 33.4-keV $(7/2^+)$ level is first forbidden transition, resulting in a substantial suppression compared to allowed β-transitions. Given the highly exotic nature of the ^{119}Pd decay, primarily due to its very low production in fission, the observed β-decay predominantly involves allowed transitions. Consequently, it can be approximated that the 33.4-keV level receives negligible β-feeding in the β-decay of ^{119}Pd.

According to the β-decay selection rules (see Table 1), the ground state to ground state transition is classified as first-forbidden. Therefore, the feeding of the ^{119}Ag ground state via this transition is very weak and can be neglected in the analysis of this nucleus's properties. The transition from the $(11/2^-)$ isomer in ^{119}Pd to the ground state in ^{119}Ag is classified as either fourth- or fifth-forbidden, so entirely insignificant.

In Tables 9,10 the β-feeding intensities in the decay of ^{119}Pd to the excited levels of ^{119}Ag, along with the $\log_{10} ft$ values are presented. An online *LogFT calculator* available at [92] was used to find the $\log_{10} ft$ values.

The spin assignments for the 686.2- and 874.4-keV levels are suggested based on the assumption that the most common electromagnetic transitions are $E1$, $M1$, and $E2$, as well as on the systematics of silver isotopes shown in Fig. 36e in Chapter 7.11.

For the 770.2-, 1579.0-, and 1803.7-keV levels, which do not belong unequivocally to neither Band A nor Band B, their β-feedings were estimated individually for each band. The 906.4-keV level, which is connected to the 770.2-keV level by a weak 136.2-keV transition, was considered to belong exclusively to Band A. The results corresponding to these four levels are presented in Table 9.

When determining the β feedings of levels, only the upper limit of the feeding is established, because many weak γ transitions feeding a given level from above may not be observed due to the Pandemonium effect, already described in Chapter 5.5. The impact of this phenomenon on the uncertainty of β feedings of levels is classified as a systematic error.

The I_β values calculated and presented in Tables 9 and 10 are different from the data presented in [70], but are in agreement with them within the measurement error limit (3σ

Table 9: The experimental estimates of β feedings represented as I_β, and $log_{10}ft$ values of the excited levels in Band A of ^{119}Ag populated in the β^- decay of ^{119}Pd. The energy levels are reported with uncertainties. The I_β values are upper limits and the $log_{10}ft$ values are lower limits. In the third column the calculated $log_{10}ft$ is presented. And the last column contains the proposed spin.

Band A			
$E_{lev}[keV]$	I_β	$log_{10}ft$ [92]	Tentative I^Π
256.6(2)	7.9(2.0)	5.95	$(3/2^-)$
326.5(1)	14.5(3.6)	5.67	$(5/2^-)$
686.2(1)	6.7(0.9)	5.90	$(3/2^-)$
770.2(1)	12.1(1.7)	5.62	$(7/2^-)$
874.4(3)	5.4(0.8)	5.94	$(5/2^-)$
906.4(1)	7.0(1.7)	5.81	$(9/2^-)$
1032.1(2)	4.0(0.6)	6.02	(1/2,...,7/2)
1157.8(3)	8.4(1.1)	5.66	(3/2,...,9/2)
1266.8(3)	1.7(0.3)	6.31	(1/2,...,7/2)
1291.9(3)	2.0(0.3)	6.24	(1/2,...,7/2)
1358.6(2)	3.2(0.5)	6.01	(1/2,...,7/2)
1440.5(2)	4.9(0.6)	5.80	(5/2,...,11/2)
1454.4(2)	8.7(1.2)	5.54	(5/2,...,11/2)
1481.7(3)	0.5(0.3)	6.77	(5/2,7/2)
1579.0(1)	2.2(0.3)	6.10	$(13/2^-)$
1663.2(2)	3.1(0.4)	5.92	(5/2,...,9/2)
1689.0(3)	2.0(0.4)	6.10	(3/2,...,7/2)
1803.7(2)	1.7(0.3)	6.13	$(11/2^-$,$13/2^-)$
1811.1(2)	1.7(0.3)	6.28	(5/2,...,13/2)
1888.5(4)	2.5(0.4)	5.93	(5/2,7/2)

limit).

As for the $log_{10}ft$ values, on the other hand, they differ slightly from the values given in [70], with the largest deviation of 3.4% occurring for the 770.2 - keV level (Band B) and the lowest for the 256.6-keV level of 0.54%. Calculated $log_{10}ft$ values indicate, that every transition, which depopulate the excited level in ^{119}Ag nuclide could be classified as allowed or first forbidden transition.

Twelve excited levels in Band A of ^{119}Ag, after taking into account additional factors presented earlier in analogous sections of previous chapters, received more specific assignments than those suggested in Table 9.

Analysis of the $\log_{10} ft$ values and γ-decay patterns allows the separation of excited states in ^{119}Ag into two distinct bands with different parities. Band A forms a regular negative-parity sequence from $1/2^-$ to $11/2^-$, as confirmed by low $\log_{10} ft$ values in the range 5.6–6.1, typical for allowed β-decays. For example, the levels at 326.5 keV ($5/2^-$, $\log_{10} ft = 5.67$) and 770.2 keV ($7/2^-$, $\log_{10} ft = 5.62$) are characteristic of strongly populated β-decay states. In contrast, the level at 1481.7 keV, despite being assigned $(5/2^-, 7/2^-)$, exhibits a higher $\log_{10} ft = 6.77$, suggesting a first-forbidden character and requiring further verification. Band B, in turn, is built on the 163.2 keV level ($9/2^+$), which is very strongly fed in β-decay with $\log_{10} ft = 5.33$, serving as a key reference for the positive-parity structure.

Table 10: The experimental estimates of β feedings represented as I_β, and $log_{10}ft$ values of the excited levels in Band B of ^{119}Ag populated in the β^- decay of ^{119}Pd. The energy levels are reported with uncertainties. The I_β values are upper limits and the $log_{10}ft$ values are lower limits. In the third column the calculated $log_{10}ft$ is presented. And the last column contains the proposed spin.

Band B			
$E_{lev}[keV]$	I_β	$log_{10}ft$ [92]	Tentative I^Π
33.4(1)	0.0	0.0	$(7/2^+)$
163.2(2)	42.5(6.6)	5.33	$(9/2^+)$
670.6(2)	11.2(1.8)	5.77	$(11/2^+)$
713.9(2)	9.6(1.4)	5.82	$(11/2^+)$
770.2(1)	1.5(0.5)	6.61	$(7/2^-)$
853.0(2)	2.5(0.6)	6.37	$(13/2^+)$
1151.0(3)	1.8(0.3)	6.42	(7/2,...,11/2)
1170.3(2)	3.3(0.5)	6.15	(7/2,...,11/2)
1207.2(3)	1.3(0.3)	6.54	$(13/2^+)$
1281.2(5)	1.2(0.3)	6.66	(7/2,...,11/2)
1376.6(2)	6.0(0.9)	5.83	(7/2,...,11/2)
1579.0(1)	1.5(0.3)	6.37	$(13/2^-)$
1709.5(4)	1.0(0.3)	6.50	(11/2,13/2)
1803.7(2)	4.4(0.7)	5.82	$(11/2^-,13/2^-)$
1849.4(5)	0.8(0.3)	6.55	(5/2,...,13/2)
2113.9(5)	2.1(0.3)	6.04	(5/2,...,13/2)
2161.8(4)	2.4(0.4)	5.96	(5/2,...,13/2)
2264.0(5)	2.6(0.4)	5.89	(5/2,...,13/2)
2417.8(7)	2.1(0.4)	5.93	(5/2,...,13/2)
2818.4(10)	2.1(0.3)	5.77	(5/2,...,13/2)

Overall, Band A and Band B are internally consistent, with the key assignments strongly supported by the measured $\log_{10} ft$ values. Several levels with higher or borderline $\log_{10} ft$ values (1481.7, 1281.2, 1207.2, 1849.4) require additional experimental investigation to firmly establish their spin and parity. To resolve ambiguities for levels such as 1481.7 keV, angular distribution and polarization measurements of the emitted γ-rays can be used to determine the multipolarity and parity change. Furthermore, lifetime measurements and internal conversion coefficient studies can provide insight into the transition character ($M1/E2$), allowing a precise spin and parity assignment. These combined methods will enable a definitive mapping of the nuclear level structure in both negative- and positive-parity bands of ^{119}Ag.

The scheme of excited states obtained from splitting data and from β^- decay data can be consistent, but only for low-energy excited states.

Decay from a low-spin state means that the nucleus does not populate higher rotational states with higher spins, which are observed in neighbouring nuclei, e.g., in ^{119}Ag (Figure 17 in [70]). These states are also visible in the splitting data.

8.6 Strength distribution in β decay

The concept of strength distribution was described in greater detail in Chapter 7.8.

In this chapter the final results for ^{119}Ag will be presented. In Fig. 41(a), data for the energy levels 770.2, 906.4, 1579.0 and 1803.7 keV are shown in gray. These levels have been highlighted among the others because they do not unequivocally belong to Band A. Instead, they are assigned as levels between Band A and Band B. Based on the transitions coming off these levels, it was calculated what proportion of the intensity feeds into each band. The 770 keV level was the hardest to match, and it was assumed that I would use the same ratio of level population intensity as level depopulation. Most of the intensity feeds into Band A. The 906 keV level was entirely assigned to Band A. The 1579 keV level also mostly feeds into Band A, and 1804 keV is the only exception, where more than half of the intensity feeds into Band B. The remaining levels are marked in black. The level at 1454.4 keV exhibited the highest $B(GT)$ value, while the 1481.5 keV level had the lowest.

In Fig. 41(b), an analogous plot is presented, but for the excited levels classified as part of Band B and level 770.2, 1579.0 and 1803.7 keV. The level at 163.2 keV showed the highest $B(GT)$ value, indicating a high probability of a Gamow-Teller transition between this level and the ground state. This supports the proposed spin assignments for these levels, as the same parity is maintained, and a spin change occurs. Conversely, the isomeric level at 33.4 keV exhibited the lowest $B(GT)$ value.

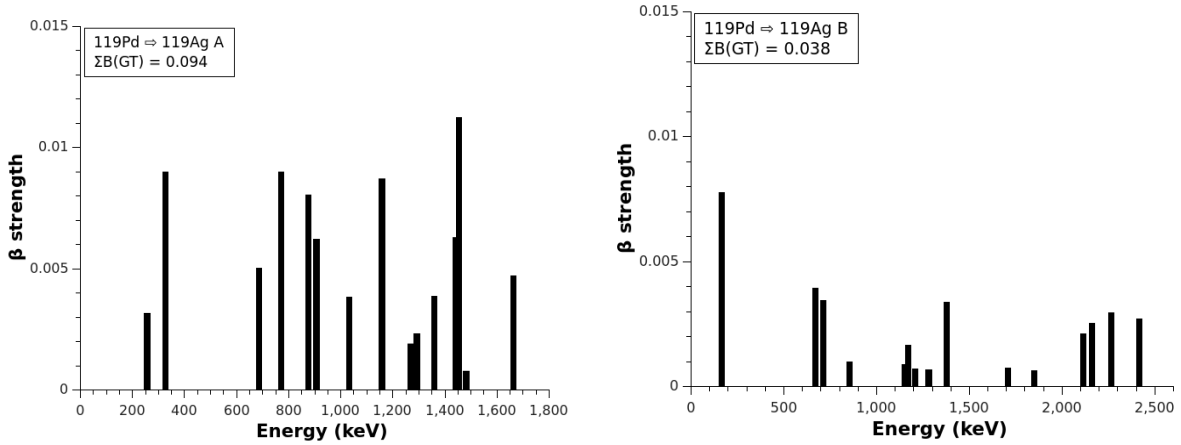

(a) (b)

Figure 41: The distributions of B(GT) decay strength in the β decay of ^{119}Pd (g.s.) to ^{119}Ag. Panel (a) presents distribution towards levels of Band A and panel (b) towards levels of Band B. The half-life [123], the β-decay energy in keV [124] and the total B(GT) strengths are presented as well.

Only the transitions that can be unambiguously assigned to Band A and Band B are presented. Thus, in Fig. 41a the level at 770.2 and 906.4 keV are included. Although in the level scheme of excited states (Fig. 40) it is located between the two bands, the presence of the intense 443.7 and 580.0 keV transitions depopulating these states justifies their assignment to Band A for the purpose of strength distribution calculations. The levels at 1579.0 and 1803.7 keV were not taken into account in these calculations, since they cannot be unambiguously assigned to any band.

Calculated sums show, that levels included in Band A are more populated through β decay, than the one in Band B. Presenting the total strength (i.e., the sum) is useful when comparing experimental data with theory, since it is not always possible to calculate the strength distribution for each individual level.

In the case of each β-strength distribution (Figure 9 in [112] and Fig. 41), one can observe many (more than 10) levels that are populated and their β-strength distribution need to be divided into more than one structure. For ^{119}Ag total strength is more than twice as large as for ^{115}Ag and ^{117}Ag.

In ^{115}Ag and ^{117}Ag (Figure 9 in [112] and Fig. 34), there was a clear division into many low-lying levels populated in the β decay at energies below 1000 keV and one or several significantly higher peaks at energies of 2000 - 2500 keV. These proportions can no longer be discerned in ^{119}Ag, both Band A and Band B (Fig. 34) are characterized by less pronounced dominant peaks. However, Band B more closely resembles, in this respect, the distributions for ^{115}Ag and ^{117}Ag.

The most uniform distribution can be attributed to Band A in ^{119}Ag among the examples described in this chapter. The peaks are distributed over a broad energy range, from approximately 300 to 2200 keV, with many comparable heights. Additionally, Band A has been characterized by the highest total B(GT) value, suggesting stronger β feeding for Band A than for Band B. In contrast, for Band B the transitions are concentrated up to 2000 keV, with no significant peaks at higher energies.

The greatest change is observed in the case of ^{119}Ag. The two lighter isotopes, ^{115}Ag and ^{117}Ag, are more consistent with each other. The total B(GT) for ^{115}Ag is about 0.105 based on Figure 9 in [112], for ^{117}Ag it is 0.110, and for ^{119}Ag the sum over both bands is 0.132. All these values are close to each other but show a slight increase, which is consistent with the Ikeda sum rule, which states that the total B(GT) for β^- and β^+ decay depends on the numbers of neutrons and protons in the nucleus, so when the number of neutrons increases, as in this case, the total B(GT) also increases [125].

8.7 Determination of the half-life for the studied nucleus

With the experimental data collected, it is possible to determine the average β decay half-life of the studied nucleus by calculating the half-lives of the strongest γ lines in the daughter nucleus or its K X-rays [39, 61]. It must be taken into account that in the scheme of excited states of exotic nuclei there may be isomeric states, which wave functions are considerably different from neighbouring nuclear levels. Consequently their half-lives usually differ as well. Therefore γ lines from isomeric levels should not be taken into account when calculating the weighted half-life average of the nucleus under study. And occasionally this type of calculation is only done using K X-ray lines, if there are no other γ lines available.

K_{α_1} and K_{α_2} x rays (of medium Z elements like silver) have so similar energies that they cannot be resolved in our germanium detectors. Obtaining an undisclosed value of the area under the peak is not entirely reliable, as there is a tail on either side of the peak. This above-mentioned phenomenon can be a source of systematic error when experimentally estimating $T_{1/2}$.

The strongest γ lines populated in β^- decay of ^{119}Pd to ^{119}Ag were examined to find their half-lives. The measurement cycle consisted of two parts: the growth period so-called *beam-on*, lasting 1887 ms, and the decay period so-called *beam-off*, lasting 1554 ms. The time cycle lengths are always integer multiples of 111 ms, which is the operation time of the JYFLTRAP Penning trap required to produce a single bunch of a monoisotopic beam.

The ratio of beam-on to beam-off time is estimated each time by checking the systematics of nuclei in the vicinity of the studied nucleus. There are no theoretical predictions

indicating what this ratio should be, so it is selected and adjusted manually each time.

During the beam-on phase, new batches of the monoisotopic samples of ^{119}Pd were implanted into the collection tape. In contrast, during the beam-off phase, the detectors registered mainly γ quanta originating from the decay chain of ^{119}Pd. And γ quanta from the background radiation [78, 79] were always present.

The plastic collection tape was moved away, each 3.4 s (one beam-on and beam-off period), to remove the long-lived decay products. And then a new cycle started again. When an ion bunch was released from the Penning trap, an additional signal was sent to the data acquisition system and recorded in the listmode data. This allowed, during the offline data analysis, to precisely identify the time a new bunch had been sent to the collection tape.

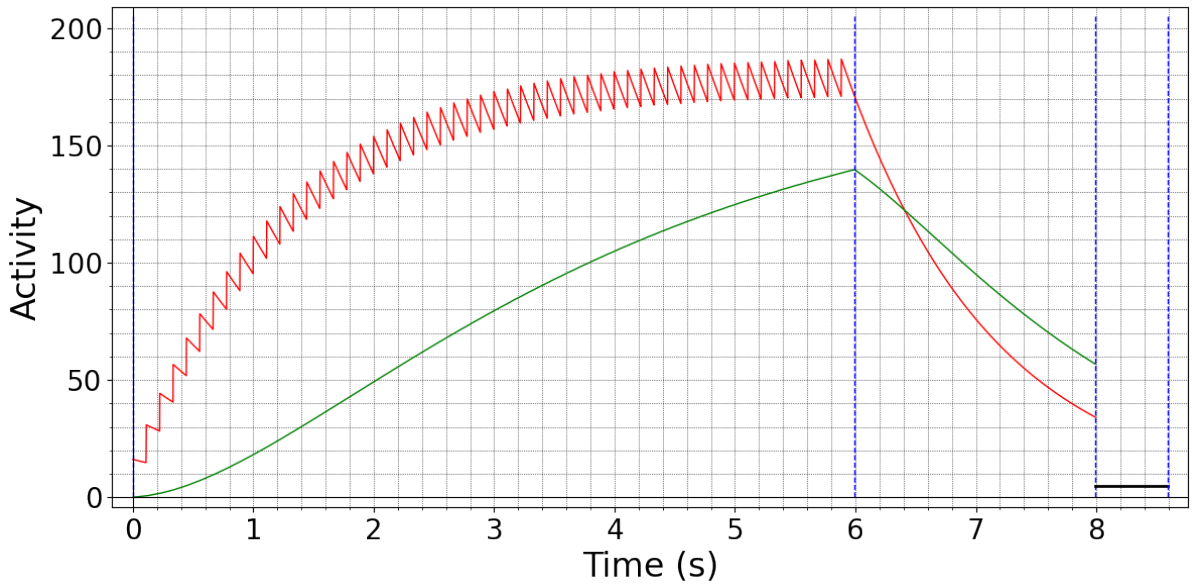

Figure 42: An example of a simulation of the beam-on and beam-off cycle for monoisotopic samples of ^{119}Pd. In the beam-on period 54 samples are delivered from the ion trap every 111 ms, next there is a decay period (beam off) of about 2 s and 0.6 s for movement of the collection tape. The time lengths of the beam-on and beam-off periods are integer multiples of the trap cycle length (here 111 ms). The red and green curves are for ^{119}Pd and ^{119}Ag, respectively.

Fig. 42 shows simulations illustrating what the beam-on and beam-off periods looked like. The red curve shows the accumulation of ^{119}Pd nuclei, where the saw tooth shape results from successive bunches of monoisotopic ions being released from the JYFLTRAP into the measurement system. In contrast, the green line shows the gradual increase in the number of ^{119}Ag nuclei resulting from the decay of the ^{119}Pd nucleus. After about 6 seconds, the growth period, here called beam-on, ends, and the process of nuclei decay begins in the beam-off period, which lasts another two seconds, until a tape shift is reached, which takes 0.6 s, and the until the collection tape movement is completed. In Fig. 42, between 6 s and 8 s, one can observe the difference in the decay half-lives of ^{119}Pd (red curve) and its daughter ^{119}Ag (green curve). Of course, radioactive nuclei are considered here, and their decay proceeds gradually, irrespective of whether it was the beam-on or beam-off period.

The limit of the fastest move and stop cycle of the collection tape is close to 1 second.

Choosing a longer beam-on and beam-off period is not a good solution in the context of this kind of research, because exotic nuclei have the shortest half-lives ($T_{1/2}$) and begin to decay during the beam-on period. Similarly, with a longer duration of beam-off period, the background radiation level in the spectrum increases, reducing the clarity of the spectrum in the context of the γ lines that are of interest. In this case, so-called a *peak-to-background* ratio will have lower value. The peak-to-background ratio refers to the quotient of the peak intensity and the background intensity within a spectrum [126].

Nonetheless, another combination of beam-on and -off periods was used, where the beam-on period was 6 s, followed by beam-off period of 2 s, and then the tape moved to remove the long-lived isotopes.

To make a calculation of the nucleus half-life, only data collected during the decay period is required. The beam-on period data was used to calculate the *growth/decay* ratio for ^{119}Ag, ^{119}Cd and background lines [78, 79] (see Fig. 45), to confirm the studied lines assignments to individual nuclei.

Typically the use of singles spectra, in determination of half-lives, is sufficient. If a γ line has a very low intensity then using a β gated γ spectrum may be the only way to find its half-life. If one wants to make a comparison between those types of spectrum, the values obtained after fitting a function to the decay curve should be very similar, no matter whether you use a first one or the latter one.

In this chapter the half-life value of ^{119}Pd has been determined, based on the singles spectra for 8 γ lines in ^{119}Ag. The collected data for decay period are presented graphically as Fig. 43 and Fig. 44), showing the dependence of transition intensity (*number of counts/net peak area*) in a function of time.

In Fig. 43, the time decay pattern is shown for five strong γ lines characteristic of the isotope ^{119}Ag. For the 129.8 keV, 256.6 keV, 326.5 keV, 507.4 keV, and 580.0 keV lines, a clear decrease in the number of counts is observed with increasing time. The 199.0 keV line, assigned to the isotope ^{119}Cd, does not exhibit any clear tendency, neither increasing nor decreasing. In contrast, the 1460.8 keV line originates from natural background radiation (^{40}K), whose half-life is $1.2 \cdot 10^9$ years [1], and therefore the number of counts remains constant within the timescale of Fig. 43.

Fig. 43 presents measured points and uncertainties in the number of counts for the peaks 129.8, 256.6, 326.5, 507.4, 580.0 keV assigned as belonging to ^{119}Ag, line 1460.8 keV from background radiation [78, 79] and 199.0 keV from ^{119}Cd. Fig. 44, on the other hand, shows the measurement points of the selected peaks together with the fitted decay curve, through which the half-lives were determined, which are presented in Table 11.

These data were fitted with an exponential function, typical for radioactive decay:

$$I(t) = I_0 e^{-\lambda t}, \tag{8}$$

where λ is the decay constant

$$\lambda = \frac{\ln(2)}{T_{1/2}} \tag{9}$$

The least square curve fit was done analytically following the handbook [127], the half-life values and its statistical uncertainties being determined from the fit parameters.

In the peak identified at 22.1 keV, in addition to the silver KX α line, part of the counts may also originate from cadmium KX α radiation. This effect is seen in data as the presence of an artificial tail on the right-hand side of the peak, which distorts the evaluated area and thus affects the calculated lifetime. This provides an explanation for

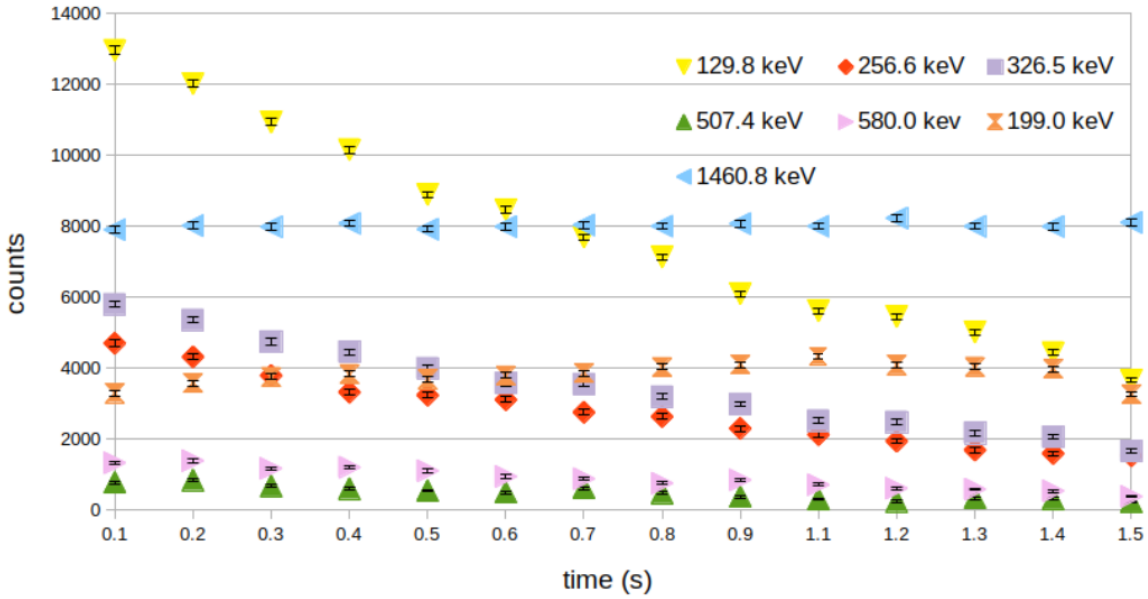

Figure 43: Time decay pattern for selected γ lines for monoisotopic samples of ^{119}Pd decaying to ^{119}Ag and background line 1460.8 keV and line 199.0 keV from ^{119}Cd. Measurement errors are indicated by black error bars.

Table 11: The half-lives of the strongest γ lines and Ag K_α X-rays (22.1 keV) populated in β^- decay of ^{119}Pd, determined in this work. The γ lines were grouped according to their assignment to Band A or Band B in the excited state scheme of the nucleus. The uncertainties are purely statistical.

Band A		Band B		Other lines	
$E_\gamma[keV]$	$T_{1/2}$ [s]	$E_\gamma[keV]$	$T_{1/2}$[s]	$E_\gamma[keV]$	$T_{1/2}$[s]
256.6	0.89(3)	129.8	0.84(2)	22.1	1.07(7)
326.5	0.87(2)	507.4	0.84(9)		
443.7	0.90(5)				
580.0	0.93(6)				

why the lifetime determined for the 22.1 keV transition is longer than for the γ lines belonging to bands A and B in ^{119}Ag in Table 11.

In the previous research [100], two half-lives were calculated based on the decrease of intensity over time of 256.6 keV and 326.1 keV lines (in this work marked as 256.6 and 326.5-keV lines). The half-lives were 0.88 $\pm$ 0.18 s and 0.95 $\pm$ 0.19 s, respectively. Both values are consistent with the half-life reported in Table 11. Also half-life based on 129.9 keV line was measured: 0.93(7) s in [100] and also this value is compliant with outcome of this work.

In this work, the weighted average half-lives were determined for two bands in ^{119}Ag. In both cases, the internal uncertainty was calculated. The following values were obtained: for band A, $\bar{T}_{1/2} = 0.88 \pm 0.02$ s, and for band B, $\bar{T}_{1/2} = 0.84 \pm 0.02$ s.

In the newer publication [70] for bands A and B, the weighted average half-lives were calculated as 0.88(2) and 0.85(1) seconds, respectively. Presented in Table 11 values are in accordance with half-life showed in [70] in most cases. A significant difference appeared for the 69.8 keV γ line, where the half-life obtained in this work is more than six times

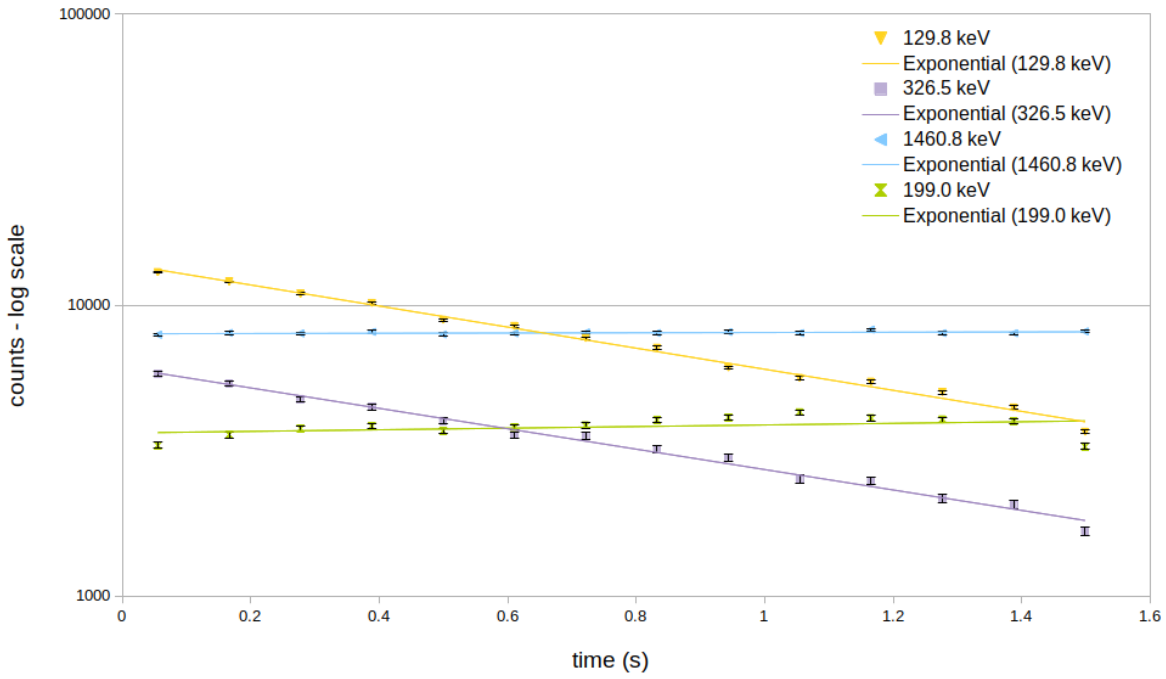

Figure 44: Measured points and time decay curves for selected γ lines for monoisotopic samples of ^{119}Ag ($T_{1/2}$ = 0.92 s [1]) and background line 1460.8 keV ($T_{1/2} = 1.248 \cdot 10^9$ y [1]) and line 199.0 keV from ^{119}Cd ($T_{1/2}$ = 2.1 s) [1]. Measurement errors are indicated by black error bars.

longer than that presented in [70]. This is probably due to the fact that this line in the studied spectrum may contain counts not only from the ^{119}Ag nucleus, but also from the nucleus of a less exotic longer-lived nucleus. The other γ lines are consistent within values from [70] in the range of the 3 σ.

Based on the data presented in Table 11, the calculated weighted, average half-life of ^{119}Ag, including measurement uncertainties, is 0.87 ± 0.02 seconds. This value represents the weighted average derived from half-lives of the individual γ lines. Since $\chi^2 \approx 2$, slightly larger than unity, the external error estimate was adopted. This value is consistent with (3 σ test) the half-life 0.92 ± 0.13 seconds presented in [100] and values presented in [70]. Band A: 0.9 ± 0.09, Band B: 0.84 ± 0.11.

Naturally it is expected that all γ lines belonging to a specific nucleus have the same $T_{1/2}$ values, with an exception of the isomeric states. The calculated half-life values (Table 11) are an additional check, whether a γ line can be classified as characteristic for some nuclide, if $T_{1/2}$ is identical.

Another method to achieve the same outcome is checking the growth/decay ratio for γ lines, so-called *Peak Area Ratio* (PAR). When examining the ratio of counts in the beam-on region to those in the beam-off region, the γ lines assigned to ^{119}Ag are expected to align along the same trend line. Figs. 43 and 44 presented the sum of the counts from three detectors.

Fig. 45 was created by dividing the counts of a given γ line during the beam-on period by the counts during the beam-off (decay) period. All data shown as Fig. 45 are singles spectrum-based, so no additional condition was set. The strongest γ lines attributed to the ^{119}Ag nucleus have been already presented as Tables 7, 8, and align along a straight line at a value of 4.55 (see Fig. 45).

The dashed lines denote in turn the values of 1.73, 2.94 and 4.55. It will be explained below how it is derived. First, the PAR values for the selected γ lines were counted. These lines were already assigned at an earlier stage of data analysis to the ^{119}Cd nucleus, to the background radiation or to the ^{119}Ag. The average PAR values for each of these groups were then estimated, and this is the origin of the above-mentioned three values.

The lines that, within their measurement uncertainties, conform to the trend line are as follows: 69.8, 256.6, 326.5, 443.7, 507.4, and 580.0 keV. The strongest γ line for this nucleus, 129.8 keV, lies a little above the trend line. The obtained value is consistent within the 3 σ test limits. However, it should be noted that this line is characterized by the smallest statistical error. A deviation from the trend line was also observed for a point representing the 617.6 keV line, which has been assigned to Band A (see Fig. 40). However, this is a less prominent γ line, and its intensity was determined from the β-gated spectrum. A comparison of the positions of the 617.6 keV points in Figs. 45 and 46 shows that the PAR points are at a different value on the vertical axis. This is precisely due to the above-mentioned fact that depending on whether one uses a singles spectrum or a β-gated spectrum one obtains a different PAR point for this γ line from the beam-on and beam-off periods. This difference was presented as Figure 7 in [70]. Where for the other γ lines seen in Figs. 45 and 46, there is no difference in the positions of the points relative to the trend line for ^{119}Ag, ^{119}Cd, and the background.

The 219.8 keV peak appeared in the analyzed spectra. However at the end of the analysis process, it was not assigned to the excitation scheme of ^{119}Ag. [70] suggests that this line could be placed as the transition, which de-excites 238.5 keV level to 18.7 keV level in ^{119}Pd the excited levels scheme.

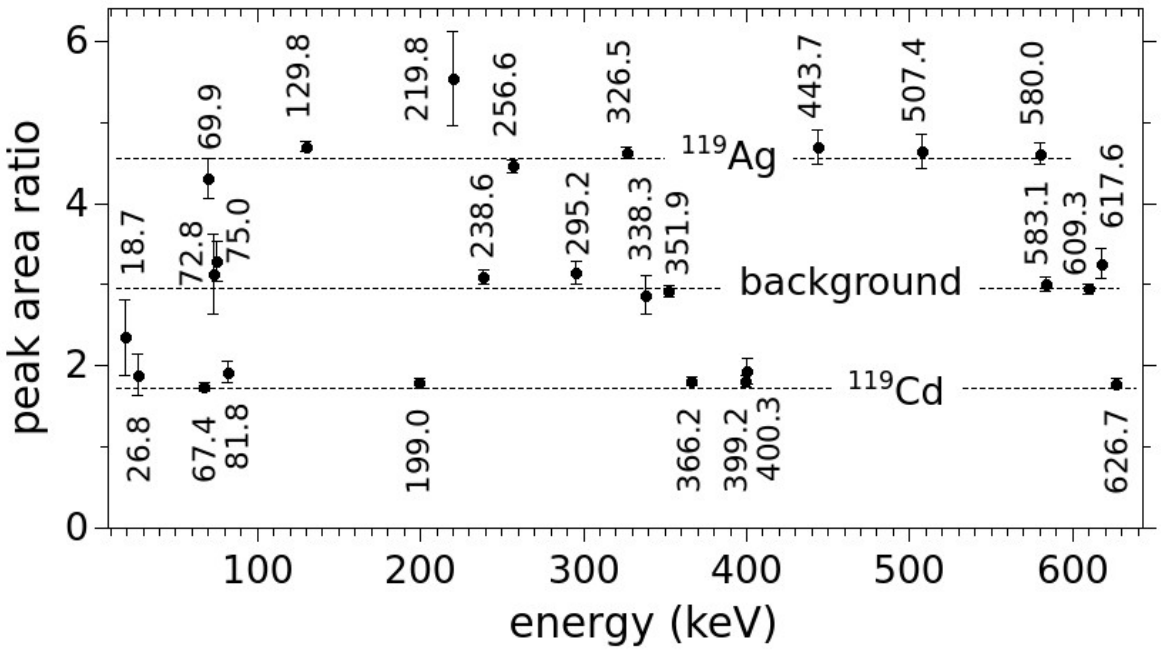

Figure 45: The values of peak area ratio (PAR) for the selected γ peaks ascribed to ^{119}Ag, ^{119}Cd and laboratory background radiation. The peak areas were taken from the singles spectra for beam-on and beam-off periods of 6 s and 2 s seconds, respectively.

This type of accumulation/decay peak area ratio graph is used to analyze peaks of very low intensity, which are barely visible in singles spectra. The PARs for the γ lines 72.8, 75.0, 238.6, 295.3, 338.3, 351.9, 583.1, and 609.3 keV consistently align around a

value of 2.94. The ratio of the duration of one period to the other is a value of 3, around which the area ratios for the background peaks were aligned. This is in line with what would be expected, since the half-lives for these lines are so long that the number of counts registered in the beam-on period is almost the same as that registered in the beam-off period. These lines were already discussed earlier in this work, in Chapter 5.2, as the strongest γ lines in the background radiation.

The third type of the PAR shown in Figs. 45 and 46 are the ones for the strongest ^{119}Cd γ lines, which arise from the β^- decay of ^{119}Ag. The PAR value of 1.73 aligns with the following lines: 67.4, 81.8, 199.0, 366.2, 399.2, 400.3, and 626.7 keV. Some of these lines were already visible in Fig. 22 in Chapter 5.2.

The reason for observed order on the vertical axis in Fig. 45 lies in the fact that ^{119}Cd is a less exotic nucleus than ^{119}Ag, which results in a longer half-life ($T_{1/2} = 2.1$ s [1]). Consequently, the smaller difference in number of counts between the beam-on and beam-off periods can be attributed to the longer $T_{1/2}$, as more nuclei remain on the tape compared to ^{119}Ag.

The positioning of the background radiation-derived lines between the γ lines assigned to ^{119}Ag and ^{119}Cd, is due to the fact that a different length of beam-on and beam-off period was used when measuring the background lines. The time used was 6 s of beam-on period and 2 s of beam-off period. These times were selected to improve statistics, and the factor of 3 in the PAR is a direct consequence of the ratio between the two time periods.

Fig. 46 presents the same type of plot as Fig. 45. The only difference lies in the application of an additional condition during the creation of this spectrum, namely the coincidence with β particles. The lines assigned to the ^{119}Ag nucleus also align along the 4.55 PAR value. Very similar results were obtained for ^{119}Ag and for the γ lines originating from ^{119}Cd.

The PARs point for 443.7 keV γ line does not align with any PAR value in this plot. However, there are also opposite tendencies. The 617.6 keV line, under the additional condition, falls within the PAR value for ^{119}Ag when its statistical uncertainty is taken into account. In contrast to the situation described above and shown in Fig. 46.

The absence of data points for the background-derived γ lines in Fig. 46 is due to the fact that these lines disappear when the coincidence condition with β particles is met. This behavior was precisely described in Chapter 5.4.

So Figs. 45, 46 confirm the assignment of γ lines such as: 69.8, 129.8, 256.6, 326.5, 443.7, 507.4, 580.0 and 617.6 to the excited structure of the ^{119}Ag nucleus, which was presented as Fig. 40.

Thanks to the use of the IGISOL+JYFLTRAP mass separation, a singles spectrum was not contaminated by γ lines originating from the oxidation of ^{103}Nb and ^{103}Mo, which were present in the system when only IGISOL was used [100].

Half-life values of exotic neutron-rich nuclei provide critical input for r-process models by determining the rate of nuclear transformations, influencing the predicted abundances of heavy elements, and enabling astrophysicists to constrain the physical conditions under which these elements are formed [128].

8.8 Historical Overview of ^{119}Ag studies

In this section, a brief review of previous experimental and theoretical studies on the properties of ^{119}Ag is presented, yet many aspects of its structure have remained unresolved until recently.

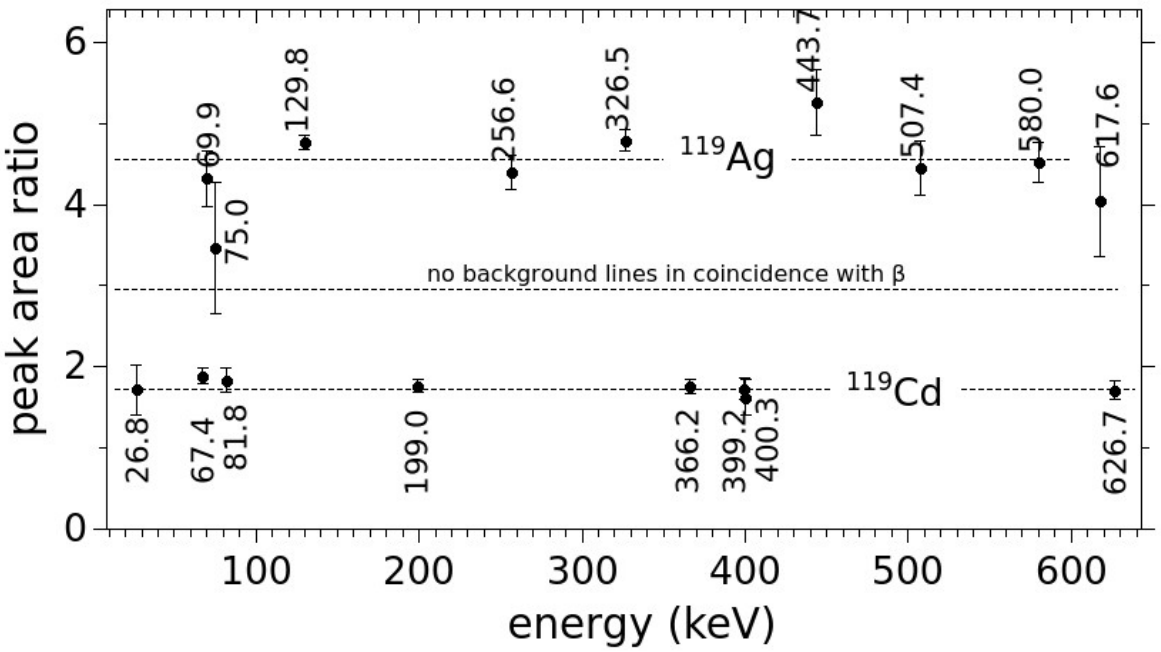

Figure 46: Accumulation/decay peak area (beam on/beam off) ratio graph for ^{119}Ag, ^{119}Cd and background from the β-gated spectra.

The ENSDF database contains only a single study on this nucleus [98]. In that work, the $A = 119$ isobars were produced at the same facility and via the same reaction as in the present thesis, ^{238}U(p, f) with a proton energy of 20 MeV, although a different target was employed.

In [98] the measured half-life for ^{119}Pd decaying to ^{119}Ag was 0.92 ± 0.13 s. This value was calculated based on the half-lives determined for the 257 keV and 326 keV transitions, for which the weighted averages of the measured values were 0.88 ± 0.18 s and 0.93 ± 0.07 s, respectively. In this work, the half-life $T_{1/2}$ for ^{119}Ag was determined to be 0.87 ± 0.02 s, which is consistent with the results reported in [98]. However, in this study, the weighted average half-life was calculated based on six strong γ transitions, including the two transitions used in [98]. The result obtained for the 256.6 keV transition, 0.89(3) s, corresponding to the 257 keV line, is consistent within 3σ. A similar situation occurs for the 326.5 keV line, which corresponds to the 326 keV γ line reported in [98]. In that work, the half-life $T_{1/2}$ was also determined for the strongest γ transition in this nucleus, 129.9 keV, and was found to be 0.93 ± 0.07 s, which is also consistent with the value obtained and presented in Table 11. A similar half-life value of 0.918 ± 0.111 s was reported in [122], where the nuclei in question were produced via fragmentation of a ^{136}Xe primary beam impinging onto a Be target.

In the work [98], the authors did not exclude the possibility of the occurrence of two β-decaying states with the same half-life but with opposite parity, which has been essentially confirmed in the present study. According to the compared half-lives presented in the paragraph above, Band A consists of excited levels characterized by negative parity or undetermined parity, while the opposite parity has been assigned to the levels belonging to Band B (see Table 10).

In [98], four excited states with energies of X, 130-X, 257, and 326 keV were reported, which correspond to the following levels in the present work: 33.4 keV, 163.2 keV, 256.6 keV, and 326.5 keV, respectively. Only a single structure was indicated in [98], in

contrast to the division into Band A and Band B proposed in this work. The spin and parity assignments for the ground state are consistent with [98], as is the assignment for the 163.2 keV level. Regarding the 257 keV and 326 keV levels, no definitive assignments were given in [98]. However, according to the systematics, for different silver isotopes, presented in Figure 5 of that work, the 257 keV state corresponds to $3/2^-$, which is also in agreement with the present study, while the 326 keV level corresponds to $5/2^-$, also consistent with our findings. Overall, [98] included only four transitions in the level scheme of ^{119}Ag, all of which were observed in the present work. Discrepancies are, however, evident in the intensities of these γ lines. The only point of agreement between the two studies is the identification of the 129.8–129.9 keV γ line as the strongest transition in the entire β-decay scheme.

When examining the Adopted Levels in [1], nothing new regarding the excited levels and γ transitions was added.

This analysis identified 37 excited states in ^{119}Ag and extended the number of observed transitions to 64, allowing for the construction of a comprehensive decay scheme for ^{119}Pd. The scheme also provides spin and parity assignments for levels in ^{119}Ag that were previously unknown.

Although previous studies reported no clear evidence for an isomeric transition in ^{119}Pd [98], the present findings allow for an alternative interpretation. The measured $\log_{10} ft$ value of 5.67 for the $(5/2^-)$ 326.5 keV and $(7/2^-)$ 770.2 keV levels in ^{119}Ag is consistent with an allowed β transition from an isomeric state in ^{119}Pd. This observation suggests the possible existence of a β-decaying isomer with spin $(5/2^-)$ or $)7/2^-)$, most likely associated with the $h_{11/2}$ neutron orbital [129].

Systematic studies of odd-mass neutron-rich Ag isotopes show that the negative-parity states $1/2^-$, $3/2^-$, and $5/2^-$, together with the positive-parity states $7/2^+$ and $9/2^+$, consistently occur at low excitation energy. The systematic behavior of these low-lying states, as outlined in [52], is interpreted as three-quasiparticle clusters coupled to collective vibrations and varies smoothly with neutron number in the mass region $A = 105-115$, in agreement with the behavior of low-lying collective levels in neutron-rich even-even Pd isotopes previously investigated at the IGISOL facility [130].

In Paar's model, nuclear states are described as three-quasiparticle configurations coupled to collective vibrations. This approach combines two fundamental mechanisms of nuclear excitation: the motion of individual quasiparticles and the collective oscillations of the nucleus.

Specifically, a *three-quasiparticle configuration coupled to collective vibrations* refers to a state in which three quasiparticles (protons or neutrons) interact with the collective vibrational modes of the nucleus, forming a complex excited state. The quasiparticles are treated as entities that can be created or annihilated in nuclear energy levels, while the coupling to collective vibrations means that these quasiparticles are not independent but interact with the nucleus's overall oscillatory motion. This framework allows the description of more complex excitations that cannot be captured by models considering only single quasiparticles or only collective vibrations.

In the present study a set of higher-lying excitations at 1579.0, 1663.2, 1803.7, 1811.1, and 1888.5 keV, which deexcite to the 906.4-keV level, has also been identified. These levels most likely carry spin $I \geq 9/2$ and may correspond to three-quasiparticle (q.p.) configurations. Similar three-q.p. excitations have been reported in other odd-A silver isotopes, and [131] proposed an oblate three-q.p. band built on top of the 1767.0-keV level. In particular, the favored decay from the 188.3-keV state to the 1579.0-keV level strongly

supports a three-q.p. character for the latter. Furthermore, the presence of several closely spaced levels in this energy region suggests that some of the 1663.2-, 1803.7-, 1811.1-, and 1888.5-keV states may also correspond to different three-q.p. excitations. Thus, while the systematic trends at low energy are confirmed, additional three-quasiparticle structures emerge at higher excitation energies.

[132] has shown that in odd-mass neutron-rich Ag isotopes, a set of deformed positive-parity levels associated with intruder configurations appears, becoming lowest in energy for ^{113}Ag, where the $1/2^+$ intruder band head is observed at 222 keV. These states were weakly populated in the β decays of ^{113}Pd and ^{115}Pd, reflecting the different structure of the initial and final states.

Although intruder $1/2^+$ [431] states are well established in odd-A Tc, Rh, and Ag isotopes, forming rotational bands in neutron-rich Ag isotopes such as ^{109,111,113,115}Ag, the present data indicate that such intruder configurations are absent in ^{117}Ag and ^{119}Ag. In these nuclei, neither β-decay studies nor spontaneous fission experiments reveal evidence for a rotational band built on the $1/2^+$ [431] state. This observation is consistent with the predicted small or negligible prolate deformation of ^{119}Ag, $\beta_2 \approx 0.1$, and the calculated oblate deformation, $\beta_2 = -0.227$, for its ground state. Therefore, based on the present findings, there is no clear evidence for the occurrence of an intruder $1/2^+$ [431] state in ^{119}Ag.

Reference [98] did not unambiguously determine the energies of the $(7/2^+)$ and $(1/2^-)$ isomers in ^{119}Ag. According to the present study, the isomer corresponds to a state with spin and parity $7/2^+$ at an excitation energy of 33.4 keV, located above the ground state with spin $1/2^+$.

The determinations presented in [1] within the dataset from β decay section differ in certain respects from those reported in [98]. In particular, the Adopted Levels evaluation is more conservative regarding the precise assignment of excitation energies for the levels, as well as the spin and parity that should be attributed to them.

Reference [100], which has been frequently cited in this work but is not included in the ENSDF or XUNDL databases, reported that the β-gated low-energy γ spectrum was dominated by the 102.6 keV peak arising from the structure of ^{103}Mo (Figure 4.8 in [100]). The isobaric contaminants ^{103}Nb and ^{103}Mo passed through the IGISOL separator as singly ionized complexes containing ^{16}O. This issue has been resolved in the present study, where the spectra are free of contaminating γ lines from the $A = 103$ isobars, thanks to the use of an ion trap.

It is also worth mentioning the findings of a study included in the XUNDL database, which is based on spontaneous fission data from ^{252}Cf, suggesting the existence of an isomeric state with an energy below 50 keV in ^{119}Ag. Additionally, it is suspected that a sudden nuclear shape transition from prolate to oblate may occur in ^{119}Ag, a phenomenon actively sought in this region of the nuclide chart. Confirming such a transition would imply a corresponding change in the ground-state spin of ^{119}Ag and potentially in subsequent silver nuclei with even neutron numbers.

Theoretical predictions for the excited states resulting from β-decay of ^{119}Pd are currently unavailable. The most recent theoretical work on neutron-rich odd palladium isotopes [133] concludes its predictions at ^{117}Pd. Furthermore, earlier calculations concerning ^{119}Pd [15] present conflicting conclusions regarding the ground-state spin compared to assignments in the ENSDF database[1].

The experimental study on excited states resulting from the β^--decay of ^{117}Pd [16], performed using the JYFLTRAP ion trap, identified a $1/2^+$ ground-state spin and a $7/2^-$

assignment for the isomeric state. This finding contradicts the hypothesis proposed by Sarriguren [15], which predicted a $9/2^-$ spin for this state. A similar spin assignment was proposed here for the next silver isotope ^{119}Ag.

Overall, the combination of historical experimental data, theoretical predictions, and the new results presented here provides a significantly more detailed and accurate picture of the structure of ^{119}Ag, highlighting the evolution of nuclear structure knowledge in neutron-rich isotopes.

8.9 Comparison of ^{119}Ag with neighbouring nuclei

In [70], Figure 16 presents the systematics of selected low-energy levels in odd-A nuclei of rhodium, silver, and indium. This is particularly relevant to studies of the ^{119}Ag nucleus, as several of the trends highlighted there are also evident in the present work. The systematics show the low-lying excited levels for silver isotopes, starting from ^{107}Ag and extending up to ^{121}Ag.

The systematic behavior of silver nuclei in this region of the nuclide chart is very consistent, as $Z = 47$ corresponds to only three proton holes relative to the closed shell at $Z = 50$, which constrains the structure and leads to regular trends in the excitation energies and spin assignments of low-lying states.

All isotopes in this series, except ^{121}Ag, have a ground state assigned with spin and parity $1/2^-$, while for ^{119}Ag this assignment remains tentative. The ground state of ^{121}Ag is assigned $7/2^+$. However, based on the findings for ^{119}Ag, a reordering of the assigned spins in ^{121}Ag cannot be ruled out, although this would require confirmation from experimental data.

The first excited level in all isotopes, except the already mentioned ^{121}Ag, is assigned spin and parity $7/2^+$. In successive isotopes, the energy of this state decreases, reaching a minimum in ^{117}Ag at 28.6 keV. The $7/2^+$ states follow a parabolic trend according to [13], meaning that their energies change approximately in a parabolic manner as a function of proton or neutron number, reaching a minimum or maximum near the mid-shell. This behavior is particularly pronounced for proton or neutron shells close to magic numbers, where the states are further stabilized due to proximity to a closed shell. Here, the mid-shell corresponds to $N = 50 + 16 = 66$, where the number of valence neutrons and holes, outside the closed shells at $N = 50$ and $N = 82$, is maximal. The $E3$ transition, which depopulates the lowest-lying excited level with spin $7/2^+$, has been observed up to ^{117}Ag, as discussed in detail in this work. This transition served as a key piece of evidence in the proposal to change the ground-state spin assignment of ^{119}Ag from $7/2^+$ to the suggested $1/2^-$ value.

The observed shift of four neutrons from the mid-shell, as seen in ^{117}Ag, arises because the parabolic minimum in excitation energy does not occur exactly at the mid-shell ($N = 66$), but slightly below it. This shift reflects the detailed shell structure and the interactions between valence neutrons and proton holes. The maximum effect of the residual interactions, which lowers the energy of the $7/2^+$ state, occurs a few neutrons away from the formal mid-shell, producing the observed displacement of the minimum by four neutrons.

Another $9/2^+$ level was observed in all silver nuclei within this range, but no clear parabolic trend was identified for these levels. Consistent trend was noted for levels with a spin of $3/2^-$, observed in every nucleus from ^{107}Ag to ^{121}Ag. In this case, the minimum occurred for ^{117}Ag at the 247.5 keV level. This behavior exhibits a parabolic trend [13],

consistent with expectations for mid-shell nuclei, as it has been already mentioned. In this case, ^{117}Ag is located four neutrons away from the mid-shell.

In each silver nucleus, an excited level with spin $5/2^-$ was observed. For ^{117}Ag, this spin was assigned to the level at 323.9 keV, which again represents a minimum in the parabolic trend among the isotopes shown in Figure 16 of [70].

Although these trends do not encompass as many isotopes, similar systematic behaviors are observed in successive isotopes of Rh and In, as also shown in Figure 16 of [70]. In the Rh isotopic chains, a systematic increase in the energy of the $1/2^-$ state is seen from ^{105}Rh to ^{113}Rh, with a similar trend for the $5/2^-$ state. The $9/2^+$ state in the chains from ^{109}Rh to ^{115}Rh exhibits nearly constant energy, while the $3/2^+$ state shows comparable energies for ^{111}Rh to ^{117}Rh. The $7/2^+$ state remains the ground state for all isotopes in the range ^{105}Rh to ^{119}Rh.

In Figure 16 [70], one can see that the $1/2^-$ states behave differently depending on the element. In the rhodium isotopes they rise quickly with energy (move upwards), while in indium they remain low. This is because they are proton states (originating from the $\pi p_{1/2}$ shell), and being close to a closed proton shell ($Z = 49$) they are further stabilized. For the In isotopic chains, the $9/2^+$ state is always the ground state. Similarly, the $3/2^-$ state follows a parabolic trend with its minimum at ^{117}In. Among analyzed three elements, the systematics of silver nuclei appear to be the richest and most consistent.

The coexistence of prolate and triaxial structures in ^{119}Ag was concluded based on the characteristics of medium-spin bands built on both the ground state and the isomer [70]. Similar phenomena should be observed in ^{117}Ag.

Analysing the data from ^{117}Ag and comparing it to ^{119}Ag, the trends in spin and parity assignments reveal a clear qualitative consistency between the two isotopes, confirming the nuclear structure features and supporting the spin and parity assignments in ^{119}Ag relative to those in the lighter ^{117}Ag.

Chapter 9. Conclusions

In the previous chapters, comprehensive results on the properties of exotic neutron-rich nuclei in the mass region $A = 110$ have been presented, and the following chapter will briefly summarize the main theses of this work. The exotic nuclei investigated in this study were produced using IGISOL coupled with the JYFLTRAP Penning trap. The ion trap requires about 100 ms to prepare a monoisotopic bunch of exotic nuclei, which sets a lower limit for the half-lives of the studied nuclei. Experimental data were processed by applying various methods such as $\beta\gamma$ coincidence spectroscopy, half-life determinations, measurements of internal conversion coefficients, and identification of isomeric transitions. Future investigations with the MR-TOF mass separator will allow access to even shorter-lived nuclei, with a high mass resolving power of $2 \cdot 10^5$ [134], thereby enabling studies of more exotic fission fragments in the $A \approx 110$ mass region.

Previous studies in this mass region employed prompt γ spectroscopy of fission fragments produced in spontaneous fission of ^{252}Cf [135] and ^{248}Cm [93], in thermal neutron-induced fission of ^{235}U [136], as well as rapid chemical separation techniques such as SISAK [97] and primary fragment separation using the LOHENGRIN mass separator [137]. However, very few experimental data originated from β-decay studies. These gaps have been addressed by the present work and by the publications on which it is based, namely [76], [70], and [71]

Complementary methods are essential in this mass region: fission studies provide insight into medium-to-high spin states, while β^- decay in low-background set-ups reveals detailed low-spin structures. Combining these approaches enables the study of long chains of neutron-rich isotopes produced in fission. In the present work, β^- decay of ^{117}Pd to ^{117}Ag and ^{119}Pd to ^{119}Ag, supported by spontaneous fission data, refined the decay schemes and confirmed excited-state structures. This allowed the resolution of previously ambiguous transitions and the identification of isomeric states.

Overall, the combination of various experimental techniques expanded nuclear level schemes, particularly in low-spin regions, and provided high-precision data for exotic, neutron-rich isotopes. The findings extend the systematic knowledge of nuclei in the $A = 110$ mass region and refine previous literature results. Furthermore, the work demonstrates the value of complementary nuclear methods for a complete understanding of nuclear structure. The thesis successfully illustrates how β decay and spontaneous fission data can be complementarily employed to study isomeric states, nuclear shapes, and decay properties, while highlighting areas for future investigation. These results provide a demanding experimental benchmark for theoretical models and contribute to the ongoing systematic description of neutron-rich nuclei.

Comparing the energy levels, spins, and parities in ^{107}Mo with the assignments in ^{117}Ag and ^{119}Ag, one can observe both resemblances and significant differences arising from the different nucleon configurations. The nucleon configuration in Mo is more complex at lower masses, so the exact energy values and spin sequences are shifted compared to Ag,

although the general band pattern remains analogous. In conclusion, Band A in ^{119}Ag roughly corresponds to negative-parity states in Mo, while Band B in ^{119}Ag is analogous to positive-parity bands in Mo, reflecting systematic behavior of nuclear structures in this region of the nuclear chart.

9.1 Conclusions for ^{107}Mo

γ transitions and excited levels in ^{107}Mo were observed in β^- decay for the first time in [76]. In total, 28 γ transitions have been assigned to the ^{107}Mo nucleus in this work. Among them, 13 transitions are newly observed, 9 are reassigned to different positions compared with the ENSDF dataset [1], and 6 are confirmed in both energy and placement relative to [1]. 15 excited levels were established, 5 of which were previously known from the literature [86, 87, 88, 89], while 10 are identified here as new. Two distinct structures decay toward a newly proposed ground state of ^{107}Mo through the 66.3- and 65.4-keV transitions, respectively. The isomeric state is assigned to the level at 65.4 keV, based on the earlier assignment reported in [88]. The spin of this level has been revised from $1/2^+$ to $5/2^+$. The experimental half-life of the ^{107}Nb nucleus is determined to be 0.27 ± 0.02 s, according to the data reported in [76]. The present results provide evidence for triaxial deformation in the ^{107}Mo nucleus. This structural feature is consistent with theoretical predictions for neutron-rich molybdenum isotopes [40] and contributes to the broader systematics of nuclear shapes relevant to the astrophysical r-process path.

9.2 Conclusions for ^{117}Ag

The present investigation of the β^- decay of ^{117}Pd to ^{117}Ag, supported by complementary spontaneous fission data [71], has enabled a refinement of the decay scheme. One of the most important levels in this nucleus is the 28.6-keV isomer, for which no direct transition to the ground state was observed in the present experiment. Nevertheless, the existence of this state was confirmed through two feeding γ transitions with energies of 147.2 and 629.7 keV. In total, 29 γ transitions were assigned to the ^{117}Ag level scheme, of which 18 were classified as new and 11 correspond to previously reported transitions. The ENSDF database [1] contains data from earlier β-decay experiments, and only two excited levels, at 247.3 and 323.8 keV, correspond directly to the levels confirmed in this work. The coincidence method proved crucial for constructing the excited-state scheme of ^{117}Ag, leading to the identification of 15 new levels and 17 new γ transitions. For the first time, a weakly deformed band built on the $1/2^-$ ground state of ^{117}Ag was observed, suggesting shape coexistence in this nucleus. This coexistence involves a prolate structure associated with the $1/2^-$ β-decaying ground state and a second structure built on the $7/2^+$ β-decaying level at 28.6 keV. A similar effect has been noted in ^{119}Ag, where the $7/2^+$ β-decaying level appears at 33.4 keV. The description of the new excited levels and transitions in this study is based primarily on β-decay data, with additional validation from prompt-γ and spontaneous fission results [71]. Altogether, the refined scheme of ^{117}Ag improves the understanding of shape coexistence phenomena and contributes significantly to the systematics of neutron-rich silver isotopes.

9.3 Conclusions for ^{119}Ag

The ENDSF database [1] contains limited information on the β^- decay of ^{119}Pd to ^{119}Ag, originating from [98]. In that work, only 5 γ transitions are listed, and all of them were confirmed in the present work with a 3σ test. 4 of these lines, with the exception of the 507.2(3)-keV line, were placed into the excited-state scheme in [98]. In [98], the corresponding levels had been given approximate assignments of 130+x, 256+y, and 326+y keV. The present analysis clarified that $y = 0$ and $x = 33.4$ keV, thereby fixing the previously ambiguous 130+x level at 163.2 keV. It was further established that the 256.6-keV and 326.5-keV levels belong to one band (Band A), whereas the 163.2-keV level and the 129.9-keV line are associated with a different structure (Band B). A total of 35 newly observed γ lines were assigned to Band A. In Band B, which contains the strongest γ transition at 129.8 keV, 23 new γ lines were identified. Altogether, the analysis confirmed five previously known γ lines and measured 58 new ones, resulting in a total of 63 transitions, the largest number reported for any nucleus in this study. With respect to excited states, 14 new levels were attributed to Band A and 15 to Band B, with an additional four new levels identified between these structures. In total, four levels previously listed in [98] were confirmed: 0.0+x, 130+x, 256+y, and 326+y keV. Alongside these, 33 new excited states were established. Two distinct structural sequences (Band A and Band B) were thus identified in ^{119}Ag (Fig. 40), following the β^- decay of the $(1/2^+)$ or $(3/2^+)$ and $(11/2^-)$ isomers of ^{119}Pd. A reassignment of spin and parity has also been proposed: the ground state, previously labeled as $7/2^+$ [1], is now reassigned to $1/2^-$, while the 33.4-keV isomer has been reclassified as $7/2^+$.

The determination of half-lives for selected γ transitions in ^{119}Ag was an essential part of this study. For weak transitions, conventional exponential fitting methods were not feasible. Therefore, numerical simulations were carried out using the open-source software SageMath. This approach relied on comparing the ratio of counts during ion implantation and subsequent decay with simulated ratios generated for a wide range of assumed half-lives. The best agreement between experimental and simulated ratios provided a reliable estimate of the half-life for each investigated transition. To overcome the excessive computation times of the built-in integration routines, a custom implementation based on Simpson's rule was developed, significantly improving efficiency without compromising accuracy. Furthermore, half-lives were measured for eight γ transitions assigned to ^{119}Ag, adding critical new information to the dataset. The calculated half-life of ^{119}Ag was 0.87 ± 0.02 s. This value is consistent (3σ test) with the half-life of 0.92 ± 0.13 s reported in [100] and with the values presented in [70]. Overall, these findings substantially refine the decay scheme of ^{119}Ag, extend the systematics of neutron-rich silver isotopes, and provide essential experimental benchmarks for theoretical models of nuclear structure in the mass region $A = 110$.

Appendix A. Novel techniques for nuclear mass and spectroscopic measurement

The final topic to be addressed in this work is the subject of some other methods that are complementary to γ-spectroscopy and are used at the University of Jyväskylä.

Till now the IGISOL technique combined with the JYFLTRAP double Penning ion trap has shown remarkable successes in studies of exotic nuclei far from stability. However, the development of optical spectroscopy is very promising for further studies, because one has to deal with nuclei that have shorter and shorter lifetimes, and as the result the post-trap γ-spectroscopy is increasingly difficult. It arises from the operating principle of the Penning trap, which functions in cycles and imposes a lower limit of about 100 ms on the measurable nucleus half-life. So the nuclides presented in this work, were at the threshold of the method's usefulness. For nucleus with half-live lower than the mentioned limit, the use of γ-spectroscopy is not recommended, because the statistics won't be sufficient.

Both γ-spectroscopy and optical spectroscopy serve as complementary tools for probing fundamental properties of nuclei and atoms. Each method provides insight into quantum levels, transition probabilities, and characteristic moments, thereby enriching our understanding of nuclear structure. Despite these commonalities, the two techniques differ significantly in their scope: γ-spectroscopy investigates high-energy nuclear transitions (up to several MeV) and yields information on nuclear energy levels, their spins, and quadrupole moments, whereas optical and laser spectroscopy focus on electronic transitions in atoms and molecules (in the eV range), enabling studies of electronic structure, magnetic moments of atoms and ions, and hyperfine effects. Used together, they provide a more complete and coherent picture of nuclear properties than either technique alone.

These methods are a Collinear Laser Spectroscopy, a Phase-Imaging Ion-Cyclotron-Resonance (PI-ICR) and last but not least a Multireflection Time-Of-Flight Mass Spectrometry (MR-TOF-MS).

In the collinear beams technique, a continuous wave laser beam is overlapped in parallel with the ion beam from the IGISOL facility. When the laser light is resonant with an atomic transition, electronic excitation takes place, with deexcitation accompanied by the emission of fluorescent photons [138]. With this method, one can obtain information on nuclear spins and deformations by measuring atomic transitions. The whole setup enables study of the isotopes of refractory elements [103], such as molybdenum. The ability to make inferences about the properties and shape of nuclei based on these independent methods is a major advantage for researchers dealing with neutron-rich nuclei in the vicinity of mass $A = 110$. Nevertheless, the fact that in one laboratory there is a γ ray spectroscopy facility and a laser spectroscopy facility is an additional powerful aspect that could lead to quicker, important publications in this area of the nuclide chart in the near

future. For instance, in this work, a result obtained in one of the recent studies [103], was used to make a spin-parity assignment of $7/2^+$ to 29.8(31) keV level and $1/2^-$ as a ground state in ^{117}Ag. This assignment was used in Chapter 7.5 in this work.

Additionally, some neutron-rich isotope such as Ag has been challenging for mass measurements since they have two or even three long-living states that are often difficult to identify and resolve from each other. To enable the study of isomeric states the PC-ICR technique could be useful. In 2024, data was acquired for less exotic silver nuclei in the mass range ^{95}Ag - ^{97}Ag [139]. In this paper high-precision mass measurements of ground-state nuclei and isomeric state of ^{96}Ag was done. PI-ICR is a high-precision technique used in Penning traps to measure the mass-to-charge ratio of ions. The method relies on recording the phase image of the ion's cyclotron motion on a detector after a defined evolution time. By analyzing the phase shift, the cyclotron frequency, and thus the ion's mass, can be determined with much higher accuracy than in conventional resonance methods.

MR-TOF-MS is another novel technique available at the IGISOL facility. It is being used to study exotic- and short-lived radioactive ion species. According to the offline tests, mass resolving powers in excess of $2 \cdot 10^5$ can be reached, enabling the purification and measurement of exotic ion species [134]. For the one of the best experiments on this setup, mass resolving power was estimated as 70 000 [140]. 10 ms is the time it takes for the MR-TOF-MS device to separate the individual ions. It is ten times shorter than the time achieved with the JYFLTRAP Penning trap. Such a short time gives a wide range of possibilities in the context of measuring exotic nuclei with even shorter half-lives.

Experimental data obtained from nuclear spectroscopy performed at the IGISOL setup are also relevant for these three methods. Since all of them share the same ion source and beam separation components, results from well-documented and repeatedly performed nuclear spectroscopy studies are essential for benchmarking experimental data acquired with other optical systems, which are continuously being developed at Jyväskylä. This approach allows for verifying whether subsequent modifications to the setup are moving in the right direction.

The combination of nuclear methods with optical techniques represents the opening of a new developmental pathway that will bring us closer to a deeper understanding of the properties of neutron-rich nuclei. Currently, this journey is only at its beginning, but with time, increasingly larger regions of the nuclide chart will be subjected to more thorough investigation.

Bibliography

[1] NNDC Brookhaven Base Evaluated Nuclear Structure Data File (ENSDF), http://www.nndc.bnl.gov/ensdf/.

[2] W. Gelletly, *Europhysics News* **31**, 9 (2000).

[3] W. Seelmann-Eggebert and G. Pfennig, *Karlsruher Nuklidkarte*, 1st ed. (Haberbeck GmbH, Germany, 1958).

[4] Z. Soti et al., *EPJ Nuclear Sci. Technol.* **10**, 7 (2024).

[5] J. Erler et al., *Nature* **486**, 509 (2012).

[6] G. Pfennig et al. (Eds.), *Karlsruher Nuklidkarte: Commemoration of the 50th Anniversary 2008* (Office for Official Publications of the European Communities, Luxembourg, 2008).

[7] K. Peräjärvi et al., *Appl. Radiat. Isotopes* **68**, 450 (2010).

[8] J. Ärje et al., *Nucl. Instr. and Meth.* **179**, 533 (1981).

[9] M. Burbidge et al., *Rev. Mod. Phys.* **29**, 547 (1957).

[10] *Report Analytical Applications of Nuclear Techniques (2004).*

[11] J. Timár et al., *J. Phys.: Conf. Ser.* **1555**, 012025 (2020).

[12] A. Bohr and B. R. Mottelson, *Nuclear Structure*, Vol. II (Benjamin, Reading, MA, 1975).

[13] R. Casten, *Nuclear Structure from a Simple Perspective* (Oxford University Press, Oxford, 1999).

[14] M. Rajput et al., *Nucl. Phys. A* **1014**, 122253 (2021).

[15] P. Sarriguren, *Phys. Rev. C* **91**, 044304 (2015).

[16] J. Kurpeta et al., *Phys. Rev. C* **98**, 024318 (2018).

[17] C.E. Rolfs, W.S. Rodney, *Cauldrons in the Cosmos: Nuclear Astrophysics*, University of Chicago Press, 1988.

[18] A.-C. Larsen, *Gamma-strength functions and level densities for nuclear structure and astrophysics*, 31st Euroschool on Exotic Beams, Jyväskylä, Finland (2024).

[19] D.N. Schramm et al., *Essays in Nuclear Astrophysics*, Cambridge University Press (1982).

[20] M. Arnould et al., Physics Reports **450**, 97 (2007).

[21] R.A. Broglia, *Surface Science* **500**, 759 (2002).

[22] M.-H Chen et al., *Mon. Not. R. Astron. Soc.* **529**, 1154 (2024).

[23] A. Aprahamian et al., *Nat. Phys.* **1**, 81 (2005).

[24] S. Curtis, *Scientific American Magazine* **328**, 30 (2023).

[25] B. Cheal et al., *Phys. Lett. B* **645**, 133 (2007).

[26] T. Togashi et al., *Phys. Rev. Lett.* **117**, 172502 (2016).

[27] R.B. Cakirli et al., *Phys. Rev. C* **78**, 041301(R) (2008).

[28] S. Lalkovski, *Bulg. J. Phys.* **44**, 498 (2017).

[29] J. Lilley, *Nuclear Physics: Principles and Applications* (John Wiley & Sons, Chichester, 2013).

[30] R. Shurtleff et al., *Am. J. Phys.* **57**, 552 (1989).

[31] A. Strzałkowski, *Wstęp do fizyki jądra atomowego* (PWN, 1978).

[32] B. Povh et al., *Particles and Nuclei: An Introduction to the Physical Concepts* (Springer, London, 2015).

[33] C.F.V. Weizsäcker, *Z. Physik* **96**, 431 (1935).

[34] O. Haxel et al., *Phys. Rev* **75**, 1766 (1949).

[35] H. Badran, PhD Thesis: *Decay spectroscopy of the very neutron-deficient lead and thallium isotopes* ^{178}Pb,^{179}Pb *and* ^{179}Tl, University of Jyväskylä (2018).

[36] J. Rainwater, *Phys. Rev.* **79**, 432 (1950).

[37] S.G. Nilsson, *Dan. Mat. Fys. Medd.* **29**, 16 (1955).

[38] B.R. Mottelson et al., *Phys. Rev.* **99**, 1615 (1955).

[39] K.S. Krane et al., *Introductory Nuclear Physics* (Wiley, New York, 1988).

[40] F.R. Xu et al., *Phys. Rev. C* **65**, 021303(R) (2002).

[41] S. Hilaire et al., *Eur. Phys. J. A* **33**, 237 (2007).

[42] K. Heyde et al., *Rev. Mod. Phys.* **83**, 1467 (2011).

[43] A. Frank et al., *Symmetries in Atomic Nuclei From Isospin to Supersymmetry*, Springer Tracts in Modern Physics, **230** (2019).

[44] A. Davydov et al., *Nucl. Phys.* **12**, 58 (1959).

[45] S. Frauendorf, *Rev. Mod. Phys.* **73**, 463 (2001).

[46] T. Mayer-Kuckuk, *Fizyka jądrowa*, PWN, Warsaw (1987).

[47] G. W. Misch et al., *Astrophys. J. Lett.* **913**, L2 (2021).

[48] O. Hahn, *Naturwissenschaften* **9**, 84 (1921).

[49] P. Walker et al., *Nuclear Physics News* **17**, 11 (2007).

[50] P. Walker et al., *Nature* **399**, 35 (1999).

[51] K. Heyde et al., *Phys. Rep.* **102**, 291 (1983).

[52] V. Paar, *Nucl. Phys. A* **211**, 29 (1973).

[53] J. J. Carroll et al., *Hyperfine Interact.* **135**, 3 (2001).

[54] B. Singh et al., *Nucl. Data Sheets* **84**, 487 (1998).

[55] N. Gove et al., *At. Data Nucl. Data Tables* **10**, 205 (1971).

[56] G. Alaga, *Phys. Rev.* **100**, 432 (1955).

[57] P. Ring, P. Schuck, *The Nuclear Many-Body Problem*, (Springer-Verlag, New York, Heidelberg, Berlin, 1980).

[58] J. Suhonen, *From Nucleons to Nucleus: Concepts of Microscopic Nuclear Theory*, (Springer-Verlag, Berlin, Heidelberg, 2007).

[59] R. B. Firestone et al., *Table of Isotopes*, 8th ed. (Springer, Budapest, 1997).

[60] T. Kibédi et al., *Nucl. Instrum. Methods Phys. Res., Sect. A* **589**, 202 (2008).

[61] J. Kantele, *Handbook of Nuclear Spectrometry* (Academic Press, London, 1995).

[62] G. Alaga et al., *Nucl. Phys. A* **97**, 600 (1967).

[63] H. Geissel et al., Chapter 2: *Exotic Nuclei and Their Separation, Electromagnetic Devices from Handbook of Nuclear Physics* (Springer, 2023).

[64] J. Kurpeta et al., *Hyperfine Interact.* **223**, 175 (2012).

[65] J. Huikari et al., *Nucl. Instrum. Methods Phys. Res. B* **222**, 632 (2004).

[66] I. D. Moore et al., *Nucl. Instrum. Methods Phys. Res. B* **317**, 208 (2013).

[67] T. Eronen et al., *Eur. Phys. J. A* **48**, 46 (2012).

[68] H. Penttilä et al., *Eur. Phys. J. A* **48**, 43 (2012).

[69] P. Karvonen et al., *Nucl. Instrum. Methods Phys. Res. B* **266**, 4794 (2008).

[70] J. Kurpeta et al., *Phys. Rev. C* **105**, 034316 (2022).

[71] A. Abramuk et al., *Phys. Rev. C* **111**, 034301 (2025).

[72] V. Kolhinen, PhD Thesis: *Penning trap for isobaric purification of radioactive ion beams at IGISOL*, University of Jyväskylä (2003).

[73] S. Naimi, PhD Thesis: *Onsets of nuclear deformation from measurements with the ISOLTRAP mass spectrometer*, Université Paris-Diderot (2010).

[74] K. Blaum et al., *Rev. Mod. Phys.* **92**, 045007 (2020).

[75] A. Rotondi et al., *AIP Conf. Proc.* **796**, 385 (2005).

[76] J. Kurpeta et al., *Phys. Rev. C* **100**, 034316 (2019).

[77] J. Kurpeta et al., *Acta Phys. Pol. B* **41**, 469 (2010).

[78] G. R. Gilmore, *Practical Gamma-Ray Spectrometry* (John Wiley & Sons, Ltd, England, 2008).

[79] K. Debertin and R. G. Helmer, *Gamma- and X-ray Spectrometry with Semiconductor Detectors* (North-Holland, 1988).

[80] Natural Background Radiation, Canadian Nuclear Safety Commission (CNSC).

[81] P. Moskal, *Foton* **117**, 4 (2012).

[82] K. Siegbahn et al., *Beta- and Gamma-ray Spectroscopy* (North-Holland Publishing Company, Amsterdam, 1955).

[83] J. Broulim, *Radiat. Detect. Technol. Methods* (2025).

[84] J. C. Hardy et al., *Phys. Lett. B* **71**, 307 (1977).

[85] A. Algora and J. L. Tain, Chapter 5: *Decay Heat and Nuclear Data*, in *Nuclear Reactors* (InTech, 2012).

[86] J. K. Hwang et al., *Phys. Rev. C* **56**, 1344 (1997).

[87] W. Urban et al., *Phys. Rev. C* **72**, 027302 (2005).

[88] J. A. Pinston et al., *Phys. Rev. C* **74**, 064304 (2006).

[89] H. Hua et al., *Phys. Rev. C* **69**, 014317 (2004).

[90] M. Wang et al., *Chin. Phys. C* **41**, 030003 (2017).

[91] BrIcc Conversion Coefficient Calculator, Australian National University.

[92] National Nuclear Data Center, $log_{10}ft$ *program*.

[93] M. A. C. Hotchkis et al., *Nucl. Phys. A* **530**, 111 (1991).

[94] K. Shizuma et al., *Z. Phys. A* **315**, 65 (1984).

[95] J. Skalski et al., *Nucl. Phys. A* **617**, 282 (1997).

[96] P. Sarriguren et al., *Phys. Rev. C* **81**, 064314 (2010).

[97] J. Rogowski et al., *Halbwertszeitbestimmung von* ^{117}*Pd*, IK Mainz Jahresbericht 1989, 14 (1990).

[98] H. Penttilä et al., *Z. Phys. A* **338**, 291 (1991).

[99] B. Fogelberg et al., *Z. Phys. A* **337**, 251 (1990).

[100] H. Penttilä, PhD Thesis: *Studies of very neutron-rich odd-mass nuclei with 109* $\leq A \leq$ *119*, University of Jyväskylä (1992).

[101] B. Fogelberg et al., *Nucl. Phys. A* **267**, 317 (1976).

[102] I. Ahmad et al., *Rep. Prog. Phys.* **58**, 1415 (1995).

[103] R.P. de Groote et al., *Phys. Lett. B* **848**, 138352 (2024).

[104] S. Eliseev et al., *Phys. Rev. Lett.* **114**, 107 (2014).

[105] J. K. Hwang et al., *Phys. Rev. C* **65**, 054314 (2002).

[106] W. Urban et al., *Eur. Phys. J. A* **22**, 157 (2004).

[107] H. Penttilä et al., *Phys. Rev. C* **44**, R935(R) (1991).

[108] V. R. Pandharipande et al., *Nucl. Phys. A* **109**, 81 (1968).

[109] J. P. Bocguet et al., *Phys. Rev.* **167**, 1117 (1968).

[110] G. Alaga et al., *Dan. Mat. Fys. Medd.*, **29**,No.9 (1955).

[111] E. Litvinova et al., *Phys. Lett. B* **730**, 307 (2014).

[112] J. Rissanen et al., *Phys. Rev. C* **86**, 034337 (2012).

[113] H. V. Weiss et al., *Phys. Rev.* **172**, 1269 (1968).

[114] W. Brüchle, PhD thesis: *Investigation of Short-lived Neutron-rich Palladium and Silver Isotopes After Rapid Chemical Separation from Fission Products*, Johannes Gutenberg University Mainz (1976).

[115] W. Urban et al., *Phys. Rev. C* **112**, 014316 (2025).

[116] P. Möller et al., *At. Data Nucl. Data Tables* **98**, 149 (2012).

[117] M. Bhuyan, *Phys. Rev. C* **92**, 034323 (2015).

[118] P. Möller et al., *At. Data Nucl. Data Tables* **109–110**, 1 (2016).

[119] S. Lalkovski et al., *Phys. Rev. C* **87**, 034308 (2013).

[120] M. Wang et al., *Chin. Phys. C* **45**, 030003 (2021).

[121] F. Wang et al., *Phys. Rev. C* **95**, 051901(R) (2017).

[122] F. Montes et al., *Phys. Rev. C* **73**, 035801 (2006).

[123] G. Audi et al., *Chin. Phys. C* **36**, 1157 (2012).

[124] M. Wang et al., *Chin. Phys. C* **36**, 1603 (2012).

[125] I. Kiyomi *Progr. Theoret. Phys.,* **31**, 434 (1964).

[126] Glossary of TEM Terms, created by JEOL Ltd.

[127] W. R. Leo, *Techniques for Nuclear and Particle Physics Experiments: A How-to Approach* (Springer-Verlag, Berlin, 1994).

[128] S. Goriely, *Eur. Phys. J. A* **59**, 16 (2023).

[129] H. Penttilä et al., *Phys. Scr.* **1990**, 38 (1990).

[130] J. Äystö et al., *Nucl. Phys. A* **480**, 104 (1988)

[131] E.H. Wang et al., *Phys. Rev. C* **95**, 064311 (2017).

[132] B. Fogelberg et al., *Proceedings of the 5th International Conference on Nuclei far from Stability*, (American Institute of Physics, New York), p. 296, (1988).

[133] M. Rajput et al., *Eur. Phys. J.* A **58**, 146 (2022).

[134] JYFL Annual Report 2022, University of Jyväskylä, Jyväskylä (2022).

[135] E. Cheifez et al., *Inst. Phys. Conf. Ser.* **51**, 193 (1980), in *Nuclear Spectroscopy of Fission Products*, ed. by T. von Egidy.

[136] L. Jacobsson et al., *Nucl. Instrum. Methods Phys. Res. B* **26**, 223 (1987).

[137] M. Graefenstedt et al., *Z. Phys. A* **334**, 239 (1989).

[138] B. Cheal et al., *Nuclear Physics News* **25**, 12 (2015).

[139] Z. Ge et al., *Phys. Rev. Lett.* **133**, 132503 (2024).

[140] JYFL Annual Report 2020, University of Jyväskylä, Jyväskylä (2020).

List of Figures

List of Tables